Design of Small Highly Maneuverable Airships

Yulin Nong

Master of Engineering

Department of Mechanical Engineering

McGill University

Montreal,Quebec

2012-06-15

A thesis submitted to McGill University in partial fulfilment of the requirements of the degree of Master of Engineering

© 2012 Yulin Nong

ABSTRACT

The aim of this thesis is to develop the theoretical framework that integrates airship size minimization, maneuverability quantification and optimal actuator placement for small highly maneuverable airship design.

The size minimization method is proposed in the first part of the thesis. The sizing flow chart is provided along with a comprehensive description and computation of four principle subsystems in airship sizing. The relationships between different subsystems are also illustrated. Novel technologies that could be applied for airship subsystems are discussed and included in the proposed sizing methods. The sizing method is validated by computing the minimum size of non-rigid airships with and without fins.

Based on the research to date conducted on ships, aircrafts and airplanes, the airship maneuverability quantification method is proposed in the second part of this thesis. The maneuver tests used to assess airship maneuverability include straight forward maneuver, turning maneuver and zig-zag maneuver. This maneuverability quantification method is first applied to the small highly maneuverable airship called ALTAV available in the Aerospace Mechatronics Lab at McGill. Based on above suggested maneuvering tests, four maneuvers are designed to test ALTAV's performance with different actuator locations: the 360° turning maneuver using PID control, the zig-zag maneuver using PID control, the straight forward maneuver using optimal control and 180° turning maneuver using optimal control.

In the third part of this thesis, aiming to understand the influence of actuator

locations and find the optimal actuator locations to provide the best maneuverability for ALTAV, the effect of actuator locations on all the elements in the dynamics model of ALTAV are analyzed, especially the effect on the entries of the inverse mass matrix are formulated through symbolic equations. Then, in order to explore the effect of actuator locations on straight forward maneuver and turning maneuver, the control forces and moments, the maximum available accelerations and angular accelerations are analyzed. The cost function used to find the optimal actuator locations is proposed based on these analysis and the optimal actuator locations fit for equal importance of longitudinal and lateral maneuvers are selected at the end of the thesis.

ABRÉGÉ

L'objectif de cette thèse est le développement d'un cadre théorethique qui intègre la minimisation de taille, la quantification de maniabilité et le placement optimal des actuateurs pour la conception de petits ballon dirigeables.

Dans la première partie de la thèse une méthode pour la minimisation de la taille est proposé. Dedans on peut trouver l'organigramme pour le dimensionnement accompagné d'une description complet de quatre sous-systèmes principaux d'un ballon dirigeable utilisé pour le dimensionnement. Les relations entre les sous-systèmes sont illustré aussi. En outre nouvel technologies applicables pour le dimensionnement de ballons dirigeables sont discutés et inclus dans la méthode proposé içi. La méthode de dimensionnement est validé en calculant la taille minimale de ballons diregeables non rigides, avec et sans ailerons.

Dans la deuxième partie de cette thèse une méthode pour la quantification de maniabilité pour avions et ballon dirigeables basée sur des recherches antérieurs est proposé. Les épreuves utilisés pour l'évaluation de maniabilité de ballon diregeables inclus des manœuvres tout droit, tournant et zigzag. Cette méthode pour quantifier la maniabilité est d'abord appliqué à un petit ballon dirigeable nommé ALTAV du Aerospace Mechatronics Lab à McGill. Basé sur les épreuves d'évaluation indiqués plus-haut, quatre manœuvres ont été conceptionnés pour évaluer la performance de l'ALTAV avec différents placements des actuateurs: un manœuvre tournant de 360° utilisant contrôle PID, un manœuvre zigzag utilisant contrôle PID, un manœuvre

tout droit utilisant contrôle optimal et un manœuvre tournant 180° utilisant contrôle optimal.

Dans la troisième et derniere partie de cette thèse l'influence du placement des actuateurs est examiné visant pour le placement optimal concernant la maniabilité de l'ALTAV. Tous les éléments affectés par le placement des actuateurs dans le modèle dynamique du ALTAV sonts analysé dans les conditions des manœuvres optimal tout droit et tournant. L'effet du vent sur l'ALTAV et l'effet du placement des actuateurs sur les éléments de la matrice inverse de la masse sonts analysé. Fondé sur cette analyse une fonction de coût est proposé pour le placement optimal des actuateurs au fin de cette thèse.

ACKNOWLEDGEMENTS

First and foremost, I want to express my deepest gratitude to my supervisors, Prof. Inna Sharf, for her indispensable guidance, invaluable advice and support throughout my graduate studies at McGill University. Prof. Sharf's broad knowledge on the various related disciplines, theoretical insights, technical depth and critical thinking have always been the source of inspiration. I want to thank Prof. Inna Sharf for her critical reading of the thesis draft and all the commends she made on my work.

My sincere thanks also go to Prof. Benoit Boulet, Prof. Jozsef Kovecses, Prof. Peter Caines, Prof. Meyer Nahon and Prof. Bruce Shepherd. The knowledge I learnt from their courses are very helpful in my thesis. I also want to thank my friend and colleague Torsten Liesk in Aerospace Lab, with whom I discussed the ALTAV dynamic model. Special thanks go to Carl for translating the abstract into French, and thanks Joyce Nault, Binder Jan and Gray Marlene for their management and help for my study at McGIll. I am also grateful to my friends who has been helping, supporting and encouraging me on my life and study at McGill, especially Ting Zou, Jing Wu, Xiaoqing Ma, Yang Zhu, Zhe Yao, Shudong Lin, Yao Tang, Tao Ding and Xuan Liu.

Last but not the least, I would like to thank my parents for their endless love and support, for everything they did for me, and for their understanding on my career development. Also, great thanks go to all my family and friends in China.

TABLE OF CONTENTS

LIST OF TABLES

LIST OF FIGURES

List of Acronyms

b	fin span, m.
C_{CD}	cross-flow drag coefficient of an infinite-length circular cylinder.
C_{DH0}	zero-angle axial drag coefficients of the hull.
C_{DF0}	zero-angle axial drag coefficients of fins.
$C_{L\alpha}$	3-D lift curve slope.
c_m	mean chord of the fin, m.
c_f	flap chord, m.
c	airfoil chord, m.
D	aerodynamic drag, N.
d	diameter of the envelope's maximum cross-section, m.
f	longitudinal membrane stress, Pa.
g	acceleration due to gravity, $9.80665 m/s^2$.
h_{cr}	airship cruise altitude, m.
I	second moment of the cross section, kgm^2.
k_{3D}	effective factor used to account for 3-D effects.
k_1, k_2, k_3	Munk inertial factor.
L_{n0}	net static lift at mean sea level, N.
$L_{n,cr}$	net static lift at cruise altitude, N.
L	aerodynamic lift, N.

l	length of the envelope, m.
M_{sta}	static bending moment, $N \cdot m$.
$M_{dyn,y}$	aerodynamic bending moment , $N \cdot m$.
$M_{adm,y}$	aerodynamic bending moment due to added-mass effect, $N \cdot m$.
$M_{vis,y}$	aerodynamic bending moment due to viscous effect, $N \cdot m$.
$M_{fh,y}$	aerodynamic bending moment due to force acting on fins, $N \cdot m$.
$M_{hf,y}$	aerodynamic bending moment due to existence of fins, $N \cdot m$.
$M_{con,y}$	aerodynamic bending moment due to control surface deflection, $N \cdot m$.
m_{H0}	envelope fabric density, kg/m^2.
m_{B0}	ballonets fabric density, kg/m^2.
$m_{eng,1}$	one engine mass, kg.
m_{hul}	hull mass, kg.
m_{bal}	ballonets mass, kg.
m_{eng}	engine mass, kg.
m_f	engine fuel mass, kg.
m_{prop}	power and propulsion system mass, kg.
m_{pay}	payload mass, kg.
m_{str}	structure mass, kg.
m_{sus}	suspension system mass, kg.
m_{anc}	ancillaries mass, kg.
m_{ij}	added mass terms.
$m_{h,ij}$	added mass terms of hull.
$m_{f,ij}$	added mass terms of fins.

$\tilde{m}_h$	helium average molecule mass, $4.0026 g/mole$.
$\tilde{m}_a$	air average molecule mass, $28.9644 g/mole$.
n_B	ballonets number.
n_{eng}	engines number.
P_{cr}	engine power used for cruise speed flight,w.
P_{max}	engine power used for maximum speed flight,w.
p_{lif}	lifting gas pressure inside the envelope at mean sea level
p_{hcr}	lifting gas pressure inside the envelope at cruise altitude
p_0	static pressure at mean sea level, $101325 Pa$.
p_{cr}	static pressure at cruise altitude, Pa.
ΔP_{min}	minimum pressure maintains rigidity, Pa.
p_{sta}	static bending pressure, Pa.
p_{dyn}	dynamic bending pressure, Pa.
p_{dif}	differential gradient pressure, Pa.
q_0	aerodynamic pressure, Pa.
q_{cr}	aerodynamic pressure at cruise speed flight, Pa.
q_{max}	aerodynamic pressure at maximum speed flight, Pa.
R	local cross section radius, m.
r_B	radius of ballonet, m.
$\mathbf{r}_G$	the position vector of center of gravity from the origin O, m.
$\mathbf{r}_V$	the position vector of center of buoyancy from the origin O, m.
r	envelope cross section radius related with fin span of b, m.
S	local cross section area, m.

S_H	envelope surface area, m^2.
S_B	ballonets surface area, m^2.
S_{HD}	drag reference area of envelope, m^2.
S_{FD}	drag reference area of fin, m^2.
S_{FS}	exposed fin area, m^2.
S_f	fin flap area, m^2.
T_{eng}	thrust,N.
T_0	absolute temperature at mean sea level,$288.15K$.
T_{cr}	temperature at cruise altitude,K.
$\dot{T}$	temperature lapse rate, $0.0065K/m$.
t_{cr}	cruise time endurance, $hour$.
t_{max}	maximum speed time endurance, $hour$.
t	envelope fabric thickness, m.
$u(c/4)$	velocity component in the x direction at the center of the 1/4-chord, m/s.
V_H	envelope volume, m^3.
V_B	ballonets volume, m^3.
$v_n(c/4)$	transverse velocity's decomposition at perpendicular direction of the fin surface, m/s.
v_{cr}	air cruise speed, m/s.
v_{max}	air maximum speed, m/s.
$\mathbf{v}$	airship velocity, m/s.
w_{dF}	local fin-induced downwash.
x_{Fs}	fin start x coordinate from nose, m.
x_{Fe}	fin end x coordinate from nose, m.

x_{cp}	center of pressure from the nose, m.
α	possible angle of attack, deg.
α_{max}	maximum survive angle of attack, deg.
α_F	geometric angle of attack, deg.
γ	angle between airship body centerline and local velocity vector at location
δ	deflection angle of the control surface, deg.
ε_m	position of the origin of body frame from the nose, m.
ε_v	position at which the flow ceases to potential, m.
η	efficient factor decided by fineness ratio.
η_d	correction factor derived from experiments.
η_T	fabric safety ratio.
η_{pr}	ratio of pressure inside envelope to outside air pressure.
η_{eng}	propulsive efficiency.
η_{BH}	ratio of ballonets volume to envelope volume.
η_{D0}	bare hull and fins drag contribution to the total drag.
η_{str}	ratio of structure mass increase to volume increase.
η_{sus}	ratio of suspension system mass increase to volume increase.
η_{anc}	ratio of ancillaries mass increase to volume increase.
η_s	ratio of fin area to airship front area
η_{wH}	weight penalty of envelope, 0.02.
η_{wB}	weight penalty of ballonets, 0.06.
η_w	weight penalty of airship system, 1.5.
η_T	fabric safety factor, 4.

ϕ, θ, ψ	airship euler angles, deg.
λ	fineness radio, l/d.
ν_{bpc}	ratio of ballonets volume used for pressure balancing.
ν_{btr}	ratio of ballonets volume used for lifting providing.
ρ	density, kg/m^3.
ρ_0	air density at mean sea level, $1.2250 kg/m^3$.
$\rho_{a,cr}$	air density at cruise altitude, kg/m^3.
σ	envelope fabric tensile strength, Nm.
σ_T	envelope fabric maximum allowable tensile strength, Nm.
τ	theoretical effectiveness factor derived from potential flow theory.
$\boldsymbol{\omega}$	airship angular velocity, deg/s.

Subscript

H	hull.
B	ballonet.
Lon	longitudinal.
Lat	lateral.
OTM	optimal turning maneuver.
$OSFM$	optimal straight forward maneuver.
TM	turning maneuver.
ZZM	zig-zag maneuver.
anc	ancillaries.
bpc	ballonet pressure control.
btr	ballonet trimming.

cr	cruise.
dif	differential.
dyn	dynamic.
end	endurance.
eng	engine.
f	fuel.
i	initial.
max	maximum.
min	minimum.
pay	payload.
sta	static.
str	structure.
sus	suspension system.
w	wind.

CHAPTER 1
Introduction

1.1 Background

The past few years have witnessed the resurgence of airship technology [14, 22, 30]. Not only a larger number of technical reports and research papers has been published than in prior years, but also new conventional and innovative airships have been designed and delivered for civil and military applications [11]. With the development of manufacturing technologies, composite materials, innovative actuators and various energy sources, airship system characteristics have been improved greatly. Compared with heavier-than-air (HTA) airplanes, lighter-than-air (LTA) and heavy lift (HL) airships consume almost no energy to stay aloft, except in the presence of winds, which gives LTA and HL airships long endurance hovering ability. The inherent safety makes airships a good choice for security applications. Besides, the airships are quieter and cheaper to operate than helicopters. A number of research groups also have investigated the potential of utilizing airships as a flight platform for long duration flight on Venus or Titan [1, 15].

Airship technologies have developed significantly from the 19th century, the design methods for small highly maneuverable airships have not caught up with the technical innovations of the last and current centuries and can not meet the needs of clients in the most operation-efficient and cost-effective way. Some of the relevant

(a) Skyship-600

(b) LZ 129 Hindenburg

Figure 1–1: Large airships in twentieth century

issues are: what is the minimum size that can suffice for a given application, what are the most suitable actuators and their optimal locations on the airship.

Although many possible applications of airships have been proposed in the last decade [29], the disadvantageous aspects of airships can not be neglected. The most obvious two disadvantages are their large surface area and the fact that they are not capable of maneuvering quickly. Before the appearance of technologies used for unmanned aerial vehicles, airships were mainly designed for cargo transportation or tourism. Hence, their sizes as exemplified by two prominent systems from the last century, the Skyship-600 (Fig. 1–1 (a)) and the LZ 129 Hindenburg (Fig. 1–1 (b)), varied from thousands of cubic meters to hundreds of thousands of cubic meters. Their large surface area made them very susceptible to wind, and they were poorly controlled in changeable weather.

1.1.1 Small Highly Maneuverable Airships

The requirements for highly maneuverable and energy efficient robots stimulated the interest in research on highly maneuverable airships, especially those with small size that can be used in indoor environment. More research focused on small highly maneuverable airship technologies, such as a hybrid flight platform constructed by

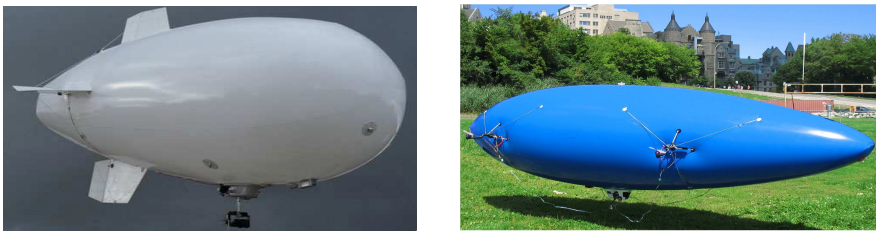

(a) E13 (b) ALTAV

Figure 1–2: Novel small airships

Western Michigan University in [38], the E13 designed by Airship Solutions Company (Fig. 1–2 (a)), and ALTAV developed by Quanser Technologies (Fig. 1–2 (b)). ALTAV is the airship at the focus of this thesis.

1.1.2 ALTAV

The motivation for developing ALTAV was to build an aerial vehicle that is energy efficient and easy to control, which is suitable for multiple indoor and outdoor usage with high maneuverability. The length of the airship is approximately 4.8 m and the maximum diameter is roughly 1.5 m. The most distinctive feature of ALTAV is its lack of aerodynamic control surfaces. Instead of large control surfaces, ALTAV has four thruster sub-assemblies mounted along the horizontal equator of the hull. Traditional airships usually have rudders, and are less maneuverable due to these large control surface area. The absence of these control surfaces makes ALTAV inherently unstable, however, the use of novel vectored thrusters gives ALTAV higher maneuverability.

1.1.3 Thesis Objectives and Motivation

The present airship design methods have not been updated sufficiently quickly and are not caught up with the technology developments. These out of date design methods are not fit for designing small highly maneuverable airships that could satisfy the requirement of new potential applications. In order to adopt novel technologies in highly maneuverable airship design, the airship sizing methods need to be revised and new design methods should be proposed. Furthermore, the minimum airship size could be estimated based on the state-of-the-art technologies.

The maneuverability of the novel highly maneuverable ALTAV airship has not been investigated systematically until now. Before delving into the study on airship maneuverability, however, the maneuverability quantification methods for airships need to be proposed first. Then, further analysis of the maneuverable characteristics of this small innovative finless airship is required, which could be used to design future small highly maneuverable airships.

1.2 Literature Review

1.2.1 Airship Sizing

The non-rigid airship sizing is a interdisciplinary research topic. The general airship system design procedure consists of three steps [29]: the Conceptual Design Procedure (CDP), the Preliminary Design Procedure (PDP) and the Detail Design Procedure(DDP). The time required for each step increases from two months for CDP to six months for PDP, and to more than twenty six months for DDP. The size of an airship is usually determined in the Conceptual Design Procedure based on the mission requirements and the system characteristics of the airship, such as the

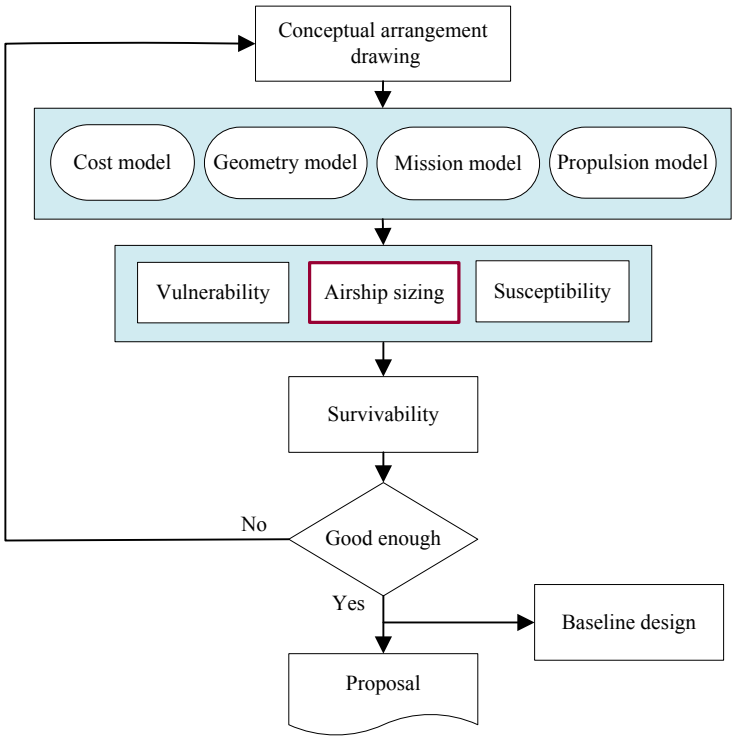

Figure 1–3: Airship conceptual design process [29](1999)

cruise altitude and the mass of each subsystem [29]. The general airship conceptual design procedure is shown in Fig. 1–3, in which the airship sizing is considered to play the central role. Airship sizing relates to the envelope geometric shape selection, the preliminary mission determination, the subsystem analysis and synthesis, the operational requirements, and the constraints with regards to fabrication and manufacture. At present, the published sizing methods are mainly based on technologies of the last century, and no clear size boundary has been determined in terms of current innovative technologies and airship application trends.

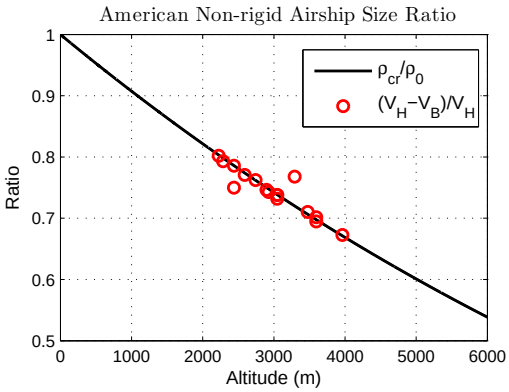

Figure 1–4: Comparison of air density ratio to envelope volume fraction

The first well known sizing work was done by Burgess [10]. In 1927, after analyzing the strength and density characteristics of a three-ply rubberized cotton cloth, Burgess estimated the maximum non-rigid airship size to be 5664 m^3(200000 ft^3). However, this size was soon exceeded by non-rigid airship series K-1 to K-135 between the years 1931 and 1945 in the U.S..

Prior to 1970, the size of non-rigid airships constructed in the U.S. was mainly defined by their required cruising altitude, which can be found by analyzing the statistical data in [31]. The data on the American non-rigid airship sizes before 1970 have been collected and plotted in Fig. 1–4, in which the x-axis is the altitude, while the y-axis shows the ratio of the air density at a cruise altitude (ρ_{cr}) to the mean sea level value (ρ_0) and the ratio of volume discrepancy between airship envelope volume (V_H) and its ballonets volume (V_B) to the envelope volume. It is obvious that the ratio $(V_H - V_B)/V_H$ is almost equal to ρ_{cr}/ρ_0 at the required cruise altitude, which means the envelope volume was equal to $\rho_0 V_B/(\rho_0 - \rho_{cr})$ at that time.

Airship sizing method provided by Goodyear Aerospace Corporation is based on the data for Akron and Macon [31]. However, this sizing method can only be applied to airships with the similar frame structure, the number of main frames and the same fineness ratio as of the Akron and Macon airships. This severely limits the applicability of this sizing method to airship design.

The maximum size of non-rigid airships under specific material and manufacturing constraints was studied by Houmard in 1986 [27]. Assuming that the goal airship has the same geometric structure as Akron airship, the maximum airship size is estimated to be 97420.8 m^3 by using envelope fabric N313A340[1] at 1068 Pa, and 173884.8 m^3 by using envelope fabric ZX458[1] at 1120 Pa.

U.S. Naval Air Development Center conducted research on the relationship between mission requirements and airship size in the last century. The size trends are discussed in [2, 32] due to variations in flight altitude, maximum speed, payload weight, cruise speed, and required endurance.

However, it is hard to use previous airship sizing methods to estimate sizes of airships with different shapes and a variety of mission profiles. In addition, none of the existing methods addressed the influence of new technologies used for airship subsystems in the airship sizing procedure.

Compared with traditional airships, new airships of this century are diverse in their size, envelope shape, available fuel sources, and they have different structures and actuators, and also higher maximum flight altitude. Since the useful lift drops

[1] Goodyear Code

quickly with the increase in altitude, airships have historically been considered as relatively low altitude vehicles. The endurance of airships varied from several hours to a week for large airships of the last century. However, experiments carried out with high-altitude [11], long endurance airships [40] have demonstrated the potential of using airships for such missions. New materials, high performance computers, new propulsion technologies, new sources of energy and more available experimental data give us the opportunity to derive novel design methods, in particular, sizing methods for small highly maneuverable airships.

1.2.2 Maneuverability: Experiments and Measures

High maneuverability is one of the important requirements for many types of vehicles, and the trade-off between maneuverability and stability is emphasized in vehicle structure design and controller design. "What constitutes a good maneuvering vehicle?", "How can one design a highly maneuverable vehicle?" and "How will actuator placement affect vehicle maneuverability?" are the central questions in theoretical research and engineering practice of vehicles.

Maneuverability Research on Ship Design and Application

Although the superior maneuverability of the English fleets led to its famous defeat of the Spanish Armada in 1588, very little research on this subject has been carried out until modern time. In 1966, Nomoto analyzed maneuver responses of ships and published his research about maneuverability and its impacts on ship design in [50], where he defined maneuvering parameters of ships for the first time. Fourteen years later (in 1980), a systematic shipboard maneuverability research was first presented by Landsburg et al. in [33], where test methods and measurements of

ship maneuverability were proposed. In [45] (in 1981), Miller et al. researched maneuvers of different water vehicles and the corresponding controllers. The test results from a turning maneuver and the effect of different number, kind and arrangement of actuators were described and compared in this paper. In 1983, Barr et al. [6] published the maneuvering performance standard for commercial vessels larger than 1000 metric tons displacement based on five years of data collection and analysis. Series of vessel maneuvering problems were analyzed, and maneuvering performance requirements and measurements were defined in that paper. In addition, maneuvering tests were described. Two years later (in 1985), Landsburg et al. [34] focused their attention on inherent maneuvering characteristics of existing vessels. In [34], an elaborate explanation of vessel maneuverability is provided. Li et al. [36], in 2005, provided the reasons why further maneuvering criteria and standards were required after emphasizing the importance of controllability and safety, and their relationship with maneuverability. Further research on ship maneuvering can be found in [60] (2005), where two maneuvering tasks are defined and an adaptive recursive design technique is developed for a parametrically uncertain nonlinear plant. However, until today, maneuverability criteria still do not meet the demand for designing highly maneuverable ships.

Maneuverability Research on Airship Design and Application

The requirements for aerial vehicles with heavy lift and good maneuverability resulted in a concept of thrust vector controlled heavy lift airships, and research into conceptual design of heavy lift maneuverable airships began in 1976 at Goodyear Corp [31]. Achieving high maneuverability of airships by employing thrust vector

control was first discussed in [53] (1979), where the possibility of improving the low speed maneuverability of airships and decreasing weight and fuel consumption by using thrust vector control was emphasized. Using a 6-DOF airship simulation model for the first time in 1984, Nagabhushan and Faiss at Goodyear Corp. proved that the low speed maneuverability of airships could be improved by using thruster vector control [47]. In their paper [47], the steady turns in a horizontal plane, and the 90 deg shifts in a prevailing 10 knot head wind were analyzed under the following three conditions: 1) the airship was controlled by rudder only; 2) the airship was controlled by rudder and bow thruster; 3) the airship was controlled by rudder and stern thruster. The simulation results in [47] showed that the maneuverability of a conventional airship could be significantly improved by using thruster vector control, and an auxiliary thruster located at the bow or the stern of the airship could significantly improve directional control of the airship, especially with the thruster at the stern. In 1985, Nagabhushan and Tomlinson conducted simulations on the take-off, landing, and ground-level maneuvers of a modern airship with twin vectorable thrusters, which were mounted on each side of the airship gondola [48]. Simulation results proved that great benefits could be obtained by incorporating a bow or a stern thruster in the airship design, including a wide range of system mass, a significant directional control power and high maneuverability at low speeds. As can be seen from the above review, up until now, only preliminary research has been done on airship maneuvering characteristics and the methods used to improve airship maneuverability. However, airship maneuverability has not been clearly defined until

now and different researchers have somewhat differing understanding of the so-called airship maneuverability.

Maneuverability Research on Aircraft Design and Application

Research on aircraft maneuverability began earlier than that on airships, and developed faster. This research covers issues such as maneuver measurements, design of highly maneuverable aircraft, optimal control realization and others. In [57] (1990), contributions to maneuverability from different parts of the X-31A aircraft were researched by Robinson and Herbst. In [8] (1993), the time-optimal reorientation maneuver for a combat aircraft was investigated by Bocvarov et al. The cost function for the minimum-time rest-to-rest reorientation maneuvers was defined, and the variational Hamiltonian of the aircraft dynamics was provided in this paper. A homotopy approach was adopted to solve this optimal problem, so that the time-optimal reorientation solutions for the simplified aircraft dynamics model could be utilized to approximate the solutions of the corresponding complex aircraft dynamics model. In [16] (1995), the time-optimal lateral maneuver of an aircraft was studied by Lutze et al. The optimal control problems of the minimum time and the minimum landing distance of an aircraft were defined. The authors provided the optimal control simulation results for maneuvers with bank-angle and sideslip-angle constraints. In [59] (2006), the flight controller of the aircraft MuPAL-α for the realization of arbitrary maneuverability was designed and the test results were provided. In order to achieve high maneuverability, Tennakoon et al.(2008) designed and simulated a control system for a unmanned aerial vehicle (UAV) in [63]. The maneuverability of the UAV was described through its tracking accuracy for different control inputs.

In order to develop design guidelines for improving the maneuverability and agility of an innovative helicopter, Olson et al. [51] assessed the impact of different design parameters on several maneuvers based on the dynamic flight simulation results of this helicopter. Eight different maneuvers for their baseline helicopter design were defined, such as hover bob-up, acceleration, deceleration, climb, turns, high-speed pull up etc, and six design variables were selected to describe the characteristics of these maneuvers, including installed power, blade loading and blade lock number. The response of the helicopter in these maneuvers was measured, and the influence of design variables on maneuverability was analyzed. Then, the design guidelines for improving helicopter maneuverability based on this analysis were provided.

1.2.3 Actuator Placement

The actuator placement problem was first suggested by Wu et al. in [66] in 1979. The motivation for this research was to study the sensor and actuator placement characteristics for large flexible space structures. The authors used a reduced order model to represent the original large-scale system. In addition, the controllability and observability of the reduced order model were considered to determine the minimum number of actuators and sensors.

In 1981, A. Arbel published his research on controllability measures and actuator placement in oscillatory systems in [5]. The modal structure of the target system is adopted in his method and the cost function for the optimal placement of the actuators is formulated based on the minimum energy problem. However, the target oscillatory systems in this research are required to be stable, which largely limits the applicability of the method.

Research on optimal actuator placement for a 90-bar truss can be referred to [39] in 1997, in which Liu et al. proposed their integrated structural topology and actuator placement design method. Simulated annealing (SA) and genetic algorithm (GA) were used to solve the topological design of discrete structures as before. The method in [39] used the ground structure approach, and both the structural size and the locations of actuators and sensors were treated as independent design variables.

Considering the faults of the eigenmode based model reduction method and the balanced realization method, Mattingly et al. proposed their extended balanced realization technique to solve optimal actuator placement issue for large scale systems in [43](1998). One requirement for this method is that the A matrix in the linearized model should be invertible, which is not satisfied by many real systems.

Stimulated by the development of smart materials, much of the literatures related to actuator placement focuses on placement of piezo-electric actuators [23, 37, 42]. Based on our review, the placement of vectorable thrusters, which are better for directional control of vessels and aerial vehicles, has not been researched heretofore.

1.3 Thesis Contribution and Organization

Chapter 2 provides a novel size minimization method of airships to be used in the Airship Conceptual Design Procedure. Based on the airship size minimization flow chart, four types of relationships in the sizing procedure are illustrated. In these models, some of the available innovative technologies for airship design are introduced and adopted in the airship size minimization procedure. The airship size synthesis is introduced after that. The sizing method validations for airships with and without fins are provided at the end of this chapter. Chapter 3 proposes three maneuver

tests and corresponding maneuverability measures based on those proposed to date for ships, airships and aircraft. The maneuverability of ALTAV is obtained based on the proposed quantification method with different actuator locations and control strategies. Chapter 4 focuses on finding optimal actuator locations for ALTAV. First, the effects on ALTAV dynamics of different actuator locations are discussed. In order to explore the effect of actuator locations on straight forward maneuver and turning maneuver, the control forces and moments, the maximum available accelerations and angular accelerations are analyzed. After that, the optimal actuator placement cost function is proposed and the optimal actuator locations for equally weighted longitudinal and lateral maneuverabilities.

Finally, in Chapter 5, conclusions are made on small highly maneuverable airship design and future potential work is discussed.

CHAPTER 2
Airship Size Minimization

This chapter focuses on airship size synthesis, aiming to obtain the minimum airship size which can satisfy operational mission requirements and is based on novel technologies in modeling, power generation and membrane material in the conceptual design procedure. For this purpose, four modules associated with airship physical system construction are presented, followed by airship size minimization function and size minimization method validation. In order to provide a clear picture of the process of the size minimization, the size minimization flow chart is provided first in Fig. 2–1, from which we can see the importance of accurate mass estimation of every subsystem and the relationships between these subsystems. The Geometric Module is introduced in Section 2.1, in which the airship envelope and ballonet shapes are given. Then, the Pressure and Fabric Module is introduced in Section 2.2. The computation of pressure over the airship envelope is provided in this section so as to guarantee that the chosen fabric for the envelope and ballonet is strong enough to maintain the rigidity of the target airship for the desired mission. In Section 2.3, the Aerostatic Module is proposed, in which the applicable static lift and required ballonets volume are derived. Next, the Power and Propulsion Module is discussed in Section 2.4, with the method used to determine the power and the mass of the propulsion system. The size minimization and airship synthesis are introduced in

Section 2.5. Finally, in Section 2.6, two airship size minimization examples are provided to validate the proposed size minimization method.

2.1 Geometric Module

The shape and the size of lighter-than-air aircraft play a very important role in flight operations, since the shape determines the aerodynamic characteristics and the size determines both the available buoyancy and the mass of the system.

2.1.1 Envelope volume and surface area

In this thesis, the geometric relationships are constrained to conventional ellipsoidal shape. There are many mathematical methods that could be used to describe the geometric relationships [12, 31, 54, 65], most of which are based on the expressions of elliptic curve of the specified envelope shape. In this thesis, the following expressions are used to represent the volume and surface area of a non-rigid airship envelope:

$$V_H = \frac{4}{3}\pi(\frac{d}{2})^2\frac{l}{2} = \frac{1}{6}\pi\lambda d^3 \ , \qquad S_H = \frac{1}{2}\pi d^2(1+\lambda^2\frac{\arccos(\frac{1}{\lambda})}{\sqrt{\lambda^2-1}}) \tag{2.1}$$

where V_H and S_H are the volume and the surface area of the airship envelope respectively, d is the diameter of the maximum cross section, λ is the fineness ratio, and l is the length of the airship. We also express the envelope surface area as a function of the volume of the airship:

$$S_H = 1.651\pi^{\frac{1}{3}}\lambda^{-\frac{2}{3}}(1+\lambda^2\frac{\arccos(\frac{1}{\lambda})}{\sqrt{\lambda^2-1}})V_H^{\frac{2}{3}} \tag{2.2}$$

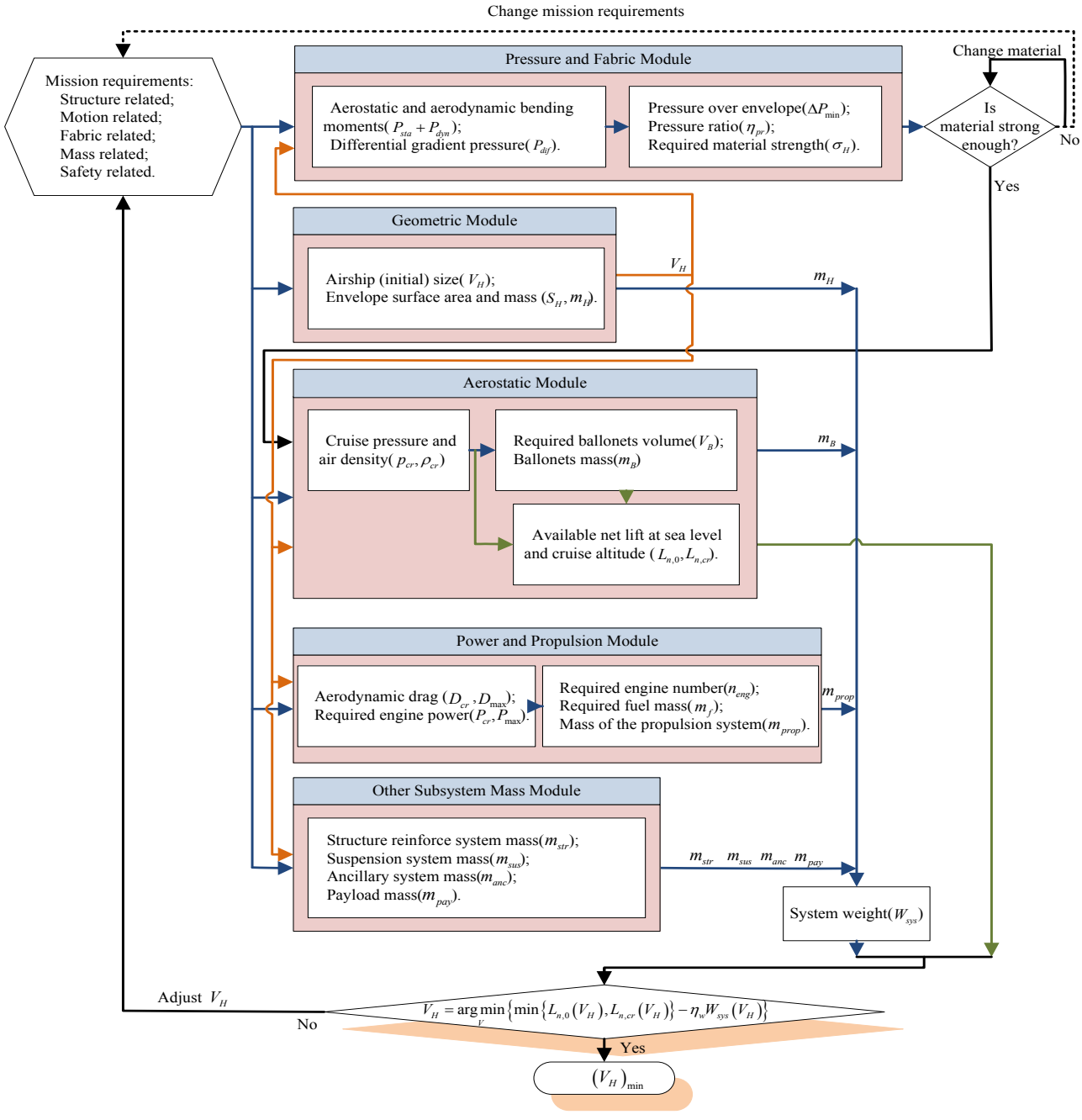

Figure 2–1: Size Minimization Flow Chart

2.1.2 Ballonet volume and surface area

One of the most important usages of ballonets is to keep the pressure balance between the inside lifting gas and the outside air if the airship is operated in an environment where air pressure and density have significant changes.

The number of ballonets typically varies from one to four, and two ballonets are used most frequently. There are no specific criteria for the shape of the ballonets, but cylinders and spheres are used widely. Since the sphere has the smallest surface area for the given volume thus minimizing the mass of the system, we use this shape as the desirable shape of ballonets in the size minimization process. Therefore, the volume V_B and surface area S_B of ballonets are calculated as:

$$V_B = n_B(\frac{4}{3}\pi r_B^3) \ , \qquad S_B = n_B(4\pi r_B^2) \tag{2.3}$$

in which r_B is the radius of a ballonet.

2.2 Pressure and Fabric Module

Because non-rigid airships lack a skeletal structure, the envelope must maintain a positive tension so as to keep its rigidity to resist the bending moments and to maintain the structural integrity. In this section, we present the envelope pressure required to maintain rigidity at the proposed flight conditions, and test whether a selected envelope fabric is strong enough to meet this pressure requirement.

2.2.1 Stress Distribution of Airship Envelope

Before presenting the details of envelope pressure calculation, it is useful to first study the stress distribution in the airship envelope. First, the envelope of an airship is assumed to be rigid under equilibrium flight conditions. For the purpose

of pressure calculation, the shape of the envelope is approximated by a cylindrical vessel in the middle and two semi-spherical vessels at each end, as shown in Fig. 2–2,

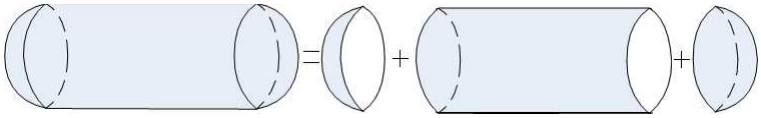

Figure 2–2: Airship Envelope Assumption

The equations used to calculate the stresses in the longitudinal and hoop directions of the cylindrical vessel and stress in the semi-spherical vessel can be found in [25], from which we find that the maximum stress occurs at the cross section with maximum radius. According to [31,41,46,64], the longitudinal and the hoop stresses at the maximum midsection of the envelope can be expressed as functions of radius r_{max}:

$$\sigma_L = \Delta p \left(\frac{r_{max}}{2}\right) , \qquad \sigma_H = \Delta p r_{max} \tag{2.4}$$

where Δp is the pressure difference between the inside and the outside of the cylindrical vessel, r_{max} is the maximum radius of the vessel, σ_L is the stress in longitudinal direction, and σ_H is the stress in the hoop direction.

From the analysis in [29], as well as from airship evolution history [3,24,61], it can be deduced that the location near the maximum diameter of the cross section has a higher potential to develop kinks, which can lead to further structual damage. Therefore, in later analysis, we will focus on the stress at the maximum diameter of the cross-section.

2.2.2 Minimum Pressure Required to Maintain Envelope Rigidity

A detailed definition of coordinates used in this thesis is provided in Chapter 3. For immediate reference, short descriptions of inertial frame and body frame are given as follows. The inertial frame ($AXYZ$) is earth-fixed, and its X axis points toward the geographic north, Y axis points toward the east and Z axis points down. The center of buoyancy (COB) is the origin of the body-fixed frame ($Oxyz$). The x axis points to the nose, the y axis points to the the right side of the airship and the z axis is downward and perpendicular to the $x-y$ plane.

The following paragraphs will focus on obtaining the minimum pressure required to maintain the envelope rigidity and on developing the relationship between bending moment and the internal and external pressure difference of the airship. First, we assume that the engineering theory of bending is valid. Then, the internal longitudinal force at the top of airship is formulated as [12, 29]:

$$\sigma_L t = \frac{f_{cross}}{2\pi r} - \sigma_{top} t = \frac{\Delta p \pi r^2}{2\pi r} - \frac{M}{I} r_{max} t = r_{max}\left(\frac{\Delta p}{2} - M\frac{t}{I}\right) \geq 0 \tag{2.5}$$

in which t is the envelope fabric thickness, σ_{top} is the tensile strength at the top of the cross section, f_{cross} is the compressive force, M is the bending moment applied at the center of buoyancy, and I is the second moment of the cross section.

Required Minimum Pressure Difference

The minimum pressure difference Δp_{min} at which the rigidity is just maintained without developing a kink could be derived from Eq. (2.5) by enforcing the equality:

$$\frac{\Delta p_{min}}{2} - M\frac{t}{I} = 0 \tag{2.6}$$

Since $I = \pi r^3 t$, we can obtain:

$$\Delta p_{min} = \frac{2Mt}{I} = \frac{2M}{\pi r^3} \tag{2.7}$$

Based on the findings in [3,24,61], the kinks are more easily developed in $x-z$ plane in body-fixed frame, and therefore, we mainly discuss the bending moment about the y-direction. For a non-rigid airship, the necessary minimum pressure difference can be decoupled into three parts:

$$\Delta p_{min} = p_{sta} + p_{dyn} + p_{dif} \tag{2.8}$$

where p_{sta} is the static bending pressure due to the static bending moment M_{sta}, p_{dyn} is the dynamic bending pressure due to the dynamic bending moment M_{dyn}, and p_{dif} is the differential pressure due to the different height of the nose and the tail of an airship.

Static Bending Pressure

In Eq. (2.8), the static bending moment M_{sta} is required to determine the static bending pressure p_{sta}. The static bending moment is generated by the discrepancy between the center of gravity and center of buoyancy locations. Using the results from Li [35], the static bending moment in y-direction is given by:

$$M_{sta,y} = mg\left(-z_G \sin\theta - x_G \cos\theta \cos\phi\right) - \rho g V_H \left(-z_V \sin\theta - x_V \cos\theta \cos\phi\right) \tag{2.9}$$

where m is the mass of the gross airship, g is the acceleration of gravity, $\mathbf{r}_G = [x_G, y_G, z_G]^T$ is the position vector from the origin O of the body-coordinate to the center of gravity, ρ is the density of the ambient air, $\mathbf{r}_V = [x_V, y_V, z_V]^T$ is the position vector from the origin O to the center of buoyancy, θ and ϕ are the pitch and the roll angles respectively. Since we define the center of buoyancy as the origin of the body-fixed frame, the static bending moment in the y-direction can be simplified to:

$$M_{sta,y} = mg\left(-z_G \sin\theta - x_G \cos\theta \cos\phi\right) \tag{2.10}$$

Dynamic Bending Pressure

In Eq. (2.8), the aerodynamic bending moment M_{dyn} is required in order to determine the aerodynamic bending pressure p_{dyn}. Understanding of aerodynamic forces and moments applied on airships took a long time to develop. In this thesis, the aerodynamic bending moment will be developed based on the airship model provided by Li in [35]. The aerodynamic bending moment on airships is composed of five parts:

$$M_{dyn,y} = M_{adm,y} + M_{vis,y} + M_{fh,y} + M_{hf,y} + M_{con,y} \tag{2.11}$$

in which $M_{adm,y}$ is the added-mass moment, $M_{vis,y}$ is the viscous moment, $M_{fh,y}$ is the moment due to the force acting on fins, $M_{hf,y}$ is the moment due to the force acting on the hull because of fins, and $M_{con,y}$ is the moment due to the control surface deflection. For airships without fins, $M_{fh,y}$, $M_{hf,y}$, and $M_{con,y}$ are zero.

1.Aerodynamic Bending Moment Due to Added-mass Moment

The calculation of added-mass forces and moments relates to complex calculation of the added-mass terms, details of which can be found in [35]. The added-mass bending moment in the y-direction is obtained as:

$$M_{adm,y} = -\left[w\left(m_{11}u\right) - u\left(m_{33}w + m_{35}q\right) + r\left(m_{44}p\right) - p\left(m_{26}v + m_{66}r\right)\right] \tag{2.12}$$

where $m_{11} = m_{h,11}$, $m_{33} = (m_{h,33} + m_{f,33})$, $m_{35} = m_{f,35}$, $m_{44} = m_{f,44}$, $m_{26} = m_{f,26}$, and $m_{66} = (m_{h,66} + m_{f,66})$ are the added-mass terms [35]. For airships without fins, $m_{f,ij} = 0$. The airship velocity in the body-fixed frame is $\mathbf{v} = [u, v, w]^T$, and angular velocity in body-fixed frame is $\boldsymbol{\omega} = [p, q, r]^T$.

2.Aerodynamic Bending Moment Due to Viscous Moment

Different methods have been used to calculate airship viscous force and moment [4,18,26,28,35,54]. In this thesis, the semi-empirical method provided in [26] and [18] is adopted to calculate the viscous moment. The viscous moment in the y-direction in the body frame is obtained by:

$$M_{vis,y} = M_{visN}\frac{w_v}{\sqrt{v_v^2 + w_v^2}} \tag{2.13}$$

in which:

$$\mathbf{v}_v = [u_v, v_v, w_v]^T = \mathbf{v} - \mathbf{v}_w \tag{2.14}$$

$$M_{visN} = -q_0 \sin 2\gamma \left(k_2 - k_1\right) \int_{\varepsilon_v}^{l} \frac{dS}{d\varepsilon}\left(\varepsilon_m - \varepsilon\right)\, d\varepsilon + q_0 \eta C_{DC} \sin^2\gamma \int_{\varepsilon_v}^{l} 2R\left(\varepsilon_m - \varepsilon\right)\, d\varepsilon \tag{2.15}$$

where $\mathbf{v}_w$ is the wind velocity vector, $\mathbf{v}_v$ is the local velocity, q_0 is the local aerodynamic pressure, k_1 and k_2 are the added-mass factors, ε is the longitudinal position from the nose, ε_m is the position of the origin of body frame from the nose, C_{CD} is

the cross-flow drag coefficient of an infinite-length circular cylinder, η is the efficiency factor decided by fineness ratio [35], R and S are the local cross-sectional radius and area, ε_v is the location at which the flow ceases to be potential, and γ is the angle between airship body centerline and local velocity vector at location ε_v.

3.Aerodynamic Bending Moment Due to Force Acting on Fins

The force acting on fins, which is normal to airship centerline, can produce pitching moment as well. The resulting moment induced by fins needs to be calculated for each fin. For one fin, the induced moment in the y-direction is calculated as [35]:

$$M_{fh,y} = M_{FN} \sin \Phi_F \tag{2.16}$$

where Φ_F is the angle from oxz body-fixed plane to fin surface plane, and

$$M_{FN} = q_0 \frac{C_{L\alpha}}{C_{l\alpha}} \alpha_F \int_{x_{Fs}}^{x_{Fe}} \int_R^b x \Delta C_{p\alpha} \left(1 + \frac{r_m a x^2}{s^2}\right) dsdx \tag{2.17}$$

in which x and s denote the longitudinal and spanwise position of a point P on the fin planform, $C_{L\alpha}/C_{l\alpha}$ is the correction factor for 3D effects [44], the factor $(1 + r^2/s^2)$ is the influence of the hull on the fins, r and b are the hull's cross-sectional radius and the fin semi span, x_{Fs} and x_{Fe} are the x coordinates of the start and end positions of the fin, $\Delta C_{P\alpha} \equiv \partial \Delta C_p / \partial \alpha$ and ΔC_p is the pressure coefficient of the airfoil, and α_F is the geometric angle of attack.

4.Aerodynamic Bending Moment Due to Force Acting on Hull Because of Fins

Because fins-induce downwash near the airship envelope, the presence of fins can lead to an additional force and moment on the airship envelope. The pitch moment

induced by one fin is calculated as:

$$M_{hf,y} = M_{HN} \sin \Phi_F \tag{2.18}$$

where,

$$M_{HN} = -q_0 \alpha_F \int_0^l \left[\pi \rho r_{max}^2 V \frac{dw_{dF}}{dx} \right] x \, dx \tag{2.19}$$

in which V is the air speed, and w_{dF} is the local fin-induced downwash. The downwash along the centerline is obtained as [35]:

$$w_{dF}(x) = V \frac{C_{L\alpha}}{C_{l\alpha}} \alpha_F \int_{x_{Fs}}^{x_{Fe}} \int_r^b \left[8\pi d_F \left(d_F - x + x_F \right) \right]^{-1} \Delta C_{p\alpha}(x_F, s) \left(1 + \frac{r^2}{s^2} \right) ds dx_F \tag{2.20}$$

where $d_F = \sqrt{(x - x_F) + s^2}$ is the distance from a point on a fin to a point on the centerline.

5.Aerodynamic Bending Moment Due to Control Surface Deflection

The pitch moment induced by elevator deflection is estimated as:

$$M_{con,y} = -\left(-L \cos \alpha - D \sin \alpha \right) \left\{ x_{cp} + c_m \left[-\frac{2 \sin \theta_f - \sin 2\theta_f}{8 \left(\pi - \theta_f + \sin \theta_f \right)} \right] \right\} \tag{2.21}$$

where L and D are the aerodynamic lift and drag generated by elevators respectively, α is the angle of attack, x_{cp} is the center of pressure, c_m is the mean chord of the fin, and $\theta_f = \cos^{-1}(2c_f/c - 1)$, in which c_f and c are the flap chord and airfoil chord respectively. The lift L and drag D are obtained as:

$$L = 2q_0 S_{FS} \left[C_{L\alpha} \tau \eta_d k_{3D} \delta \right] \ , \qquad D = 2q_0 S_{FS} \left[1.7 \left(\frac{c_f}{c} \right)^{1.38} \left(\frac{S_f}{S_{FE}} \right) \sin^2 \delta \right] \tag{2.22}$$

where S_{FS} is the exposed fin area, $C_{L\alpha}$ is the 3D lift curve slope, τ is the theoretical effectiveness factor derived from the potential flow theory [44], η_d is the correction factor based on experiments [35], k_{3D} is the efficiency factor used to account for 3D effects [18], δ is the deflection angle of the control surface, and S_f is the fin flap area.

Differential Pressure

Under some circumstances, the fore and the stern of an airship will not be at the same level, for example when at a large angle of attack or during kiting motion, where the tail rises up as the airship appears to perform a nose stand. The internal and external pressure difference will be slightly changed due to this altitude difference, and this pressure difference is calculated as:

$$p_{dif} = \rho g h = g\rho_a \left(1 - \frac{\tilde{m}_h}{\tilde{m}_a}\right) l \sin \alpha_{max} \tag{2.23}$$

where ρ_a is the density of ambient air, $\tilde{m}_h$ and $\tilde{m}_a$ are the molecular mass of the lifting gas and the ambient gas respectively, l is the length of the airship and α_{max} is the required maximum survival angle between the horizontal line and the airship body centerline.

Combining Eqs. (2.8-2.9, 2.11, 2.23), the minimum pressure difference of the airship is obtained as:

$$\Delta p_{min} = \frac{2\left(M_{sta,y} + M_{dyn,y}\right)}{\pi r^3} + p_{diff} \tag{2.24}$$

Setting the above equal to $(p_{hi} - p_a)$, in which p_{hi} and p_a are the pressure of lifting gas and the pressure of ambient air respectively, the internal and external gas

pressure ratio η_{pr} of the envelope is calculated as:

$$\eta_{pr} = \frac{p_{hi}}{p_a} = 1 + \frac{\Delta p_{min}}{p_a} \tag{2.25}$$

2.2.3 Membrane Materials

Having obtained the minimum pressure difference required to keep the target airship's rigidity, we now focus on choosing a proper membrane for the airship envelope. The desirable properties of envelope materials and ballonet materials are discussed in [29]. Since those for the envelope impose more constraints than the desirable properties for the ballonets, most materials used to make envelopes can also be used for the ballonets. The comparison of the density to tensile strength of several envelope materials is shown in Fig. 2–3 as obtained by Japan Aerospace Exploration Agency [29], and the recommended materials for airships are Vectran and Zylon. However, if decreasing the mass of the target airship is the first property in airship design, GTS could also be a good candidate for the envelope.

Based on the discussion in Section 2.2.1, in order to guarantee material strength and maintain rigidity of the airship, the tensile strength of the candidate envelope membrane should satisfy:

$$\sigma_T \geq \eta_T \sigma_H = \eta_T \Delta p_{min} r \tag{2.26}$$

where η_T is the fabric safety factor, suggested to be 1.5 according to [17].

2.3 Aerostatics Module

In contrast to HTA vehicles, LTA vehicles depend on the principle of buoyancy for their primary lift. In this section, the principle of gas expanding while an airship ascends is described at first. Then the pressure and density of ambient air are given,

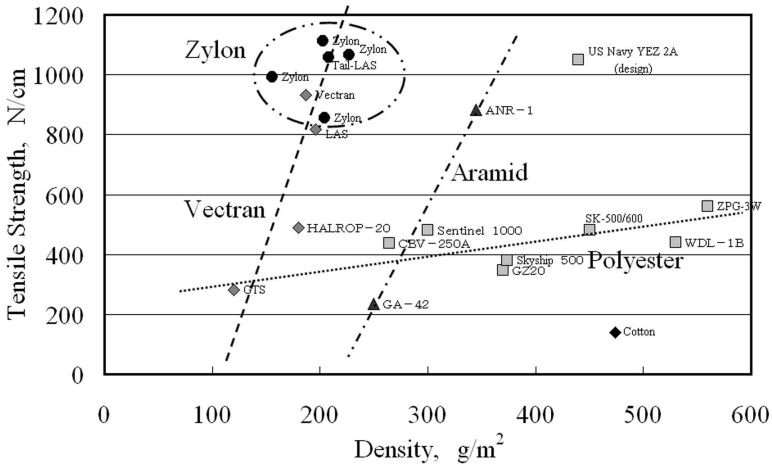

Figure 2–3: Comparison of Fabric Materials [40]

following with the lifting gas pressure and density obtained according to Ideal Gas Law. In Section 2.3.3, the required ballonets volume is obtained.

2.3.1 Principle of Gas Expanding While Airship Ascends

At mean sea level, the net lift L_{n0} is calculated as:

$$L_{n0} = (\rho_0 - \rho_{hi})\, g\, (V_H - V_B) \tag{2.27}$$

where ρ_0 is the density of ambient air, and ρ_{lif} is the density of lifting gas inside the envelope at mean sea respectively. The airship ascent is depicted in Fig. 2–4. The lifting gas volume changes from $(V_H - V_B)$ to V_H, and the ballonets volume changes from V_B to zero, while the airship ascends from mean sea level to cruise altitude. Further theoretical analysis of airship ascent can be found in [29]. Then the net

static lift $L_{n,cr}$ of the airship at cruise altitude is:

$$L_{n,cr} = (\rho_{cr} - \rho_{hcr})\, gV_H \tag{2.28}$$

in which ρ_{cr} is the density of ambient air at cruise altitude, and ρ_{hcr} is the density of lifting gas at cruise altitude.

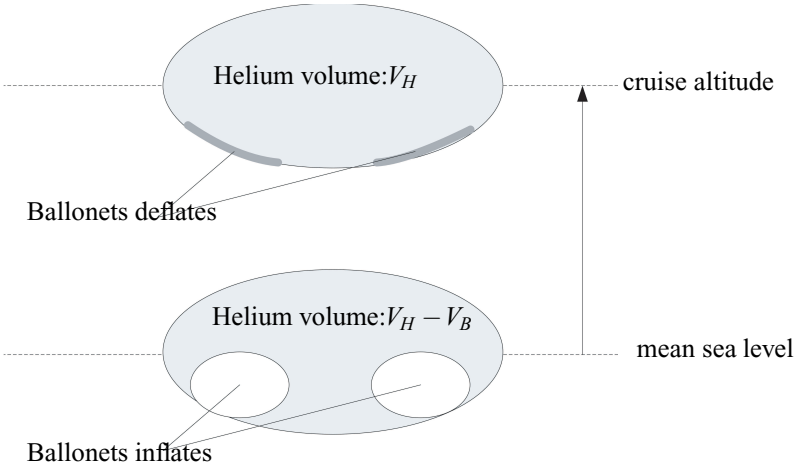

Figure 2–4: Airship Rising from Mean Sea Level to Cruise Altitude

2.3.2 Gas Pressure and Density

An airship hovers because of lift resulting from the Archimedes Principle. In this section, we present the equations to obtain the pressure and density of the lifting gas at the mean sea level and at cruise altitude, which are needed to derive the ballonets volume. Standard atmosphere model provided in [49] is adopted in this thesis.

According to Ideal Gas Law at mean sea level, if the inside lifting gas pressure is $\eta_{pr} p_0$, the density will be $\eta_{pr} \rho_0$. At cruise altitude, the volume of lifting gas increases from $(V_H - V_B)$ to V_H. Assuming that the inside lifting gas mass is constant, the

density and volume of lifting gas at mean sea level and at cruise altitude satisfy:

$$\rho_{h0}\left(V_H - V_B\right) = \rho_{hcr} V_H \tag{2.29}$$

Dividing both sides by V_H, the following equation can be obtained:

$$\rho_{hcr} = \rho_{h0}\left(1 - \frac{V_B}{V_H}\right) = \eta_{pr}\rho_0\left(1 - \frac{V_B}{V_H}\right) \tag{2.30}$$

Assuming that the temperature inside the envelope is the same as that outside the envelope, thus according to Ideal Gas Law, the following equation can be obtained:

$$\frac{p_{h0}}{\rho_{h0} T_0} = \frac{p_{hcr}}{\rho_{hcr} T_{cr}} \tag{2.31}$$

where p_{h0} and T_0 are the pressure and temperature at mean sea level respectively, p_{hcr} and T_{cr} are the pressure and temperature at the cruise altitude respectively. Multiplying both sides by ρ_{hcr} and T_{cr}, we obtain:

$$p_{hcr} = p_{h0}\frac{\rho_{hcr} T_{cr}}{\rho_{h0} T_0} = \eta_{pr} p_0\left(1 - \frac{V_B}{V_H}\right)\left(1 - \frac{\dot{T} h_{cr}}{T_0}\right) \tag{2.32}$$

where p_0 is the pressure at mean sea level, $\dot{T} = dT/dz$ is the temperature lapse constant of Standard Atmosphere, h_{cr} is the cruise altitude. Table 2–1 summarizes quick reference for the conditions of ambient air and lifting gas at mean sea level and cruise altitude.

Table 2–1: Temperature, Pressure, Density of Air and Lifting Gas at Mean Sea Level and Cruise Altitude

		Mean sea level	**Cruise altitude** ($h_{cr} \leq 11000m$)
Ambient Air [49]	temperature,K	T_0	$T_{cr} = T_0 - \dot{T} h_{cr}$
	pressure,Pa	p_0	$p_{cr} = p_0 \left(\frac{T_{cr}}{T_0}\right)^{\frac{g}{\dot{T} R_{gc}}}$
	density,kg/m^3	ρ_0	$\rho_{cr} = \rho_0 \left(\frac{T_{cr}}{T_0}\right)^{\frac{g}{\dot{T} R_{gc}}-1}$
Lifting gas	temperature,K	T_0	T_{cr}
	pressure,Pa	$p_{h0} = \eta_{pr} p_0$	$p_{hcr} = p_{h0}\left(1 - \frac{V_B}{V_H}\right)\left(1 - \frac{\dot{T} h_{cr}}{T_0}\right)$
	density,kg/m^3	$\rho_{h0} = \eta_{pr} \rho_0$	$\rho_{hcr} = \rho_{h0}\left(1 - \frac{V_B}{V_H}\right)$

2.3.3 Required Ballonets Volume

The two most common functions of the ballonets during the airship operation are balancing the internal and the external pressure, and providing enough net static lift. Therefore, based on the method proposed in [31, 52], the volume of ballonets can be derived as:

$$V_B = \left(\nu_{bpc} + \nu_{btr}\right) V_H \tag{2.33}$$

where ν_{bpc} is the factor indicating the ratio of ballonets volume used for pressure balancing, and ν_{btr} is the factor indicating the ratio of ballonets volume used for lift. The value of ν_{bpc} can be further derived as:

$$\nu_{bpc} = \frac{p_{h0} - p_{hcr}}{p_{h0}} = 1 - \frac{p_{hcr}}{p_{h0}} \tag{2.34}$$

The value of ν_{btr} used for lift is obtained as:

$$\nu_{btr} = \frac{L_{n0} - L_{n,cr}}{L_{n0}} = 1 - \frac{(\rho_{cr} - \rho_{hcr})\, gV_H}{(\rho_0 - \rho_{h0})\, g\,(V_H - V_B)} \tag{2.35}$$

Combining Eqs. (2.30), (2.33-2.35) and using $\rho_{h0} = \eta_{pr}\rho_0$, $\eta_{BH} = V_B/V_H$, we obtain a quadratic equation in η_{BH}:

$$\eta_{BH}^2 \left(\frac{\dot{T}h_{cr}}{T_0}\right) + \eta_{BH} \left(-2\frac{\dot{T}h_{cr}}{T_0} - \frac{\rho_{h0}}{\rho_0 - \rho_{h0}} - 1\right) + \left(\frac{\dot{T}h_{cr}}{T_0} - \frac{\rho_{cr}}{\rho_0 - \rho_{h0}} + \frac{\rho_{h0}}{\rho_0 - \rho_{h0}} + 1\right) = 0 \tag{2.36}$$

Solution of this equation yields the ratio η_{BH} of ballonets volume to envelope volume from which the ballonets volume is directly obtained as:

$$V_B = \eta_{BH} V_H \tag{2.37}$$

From the ballonets volume V_B, the radius r_B and the surface S_B of ballonets are obtained. Referring to Eq. (2.3), we further develop the relationship between ballonets surface area and envelope volume as:

$$S_B = (4n_B\pi)^{\frac{1}{3}} (3\eta_{BH})^{\frac{2}{3}} V_H^{\frac{2}{3}} \tag{2.38}$$

where n_B is the number of ballonets.

2.4 Power and Propulsion Module

Three components must be included in the power and propulsion system: the engine, the energy source, and the actuator used to produce forces and moments to propel the airship. In this section, the methods used to obtain the mass of both conventional and unconventional power and propulsion systems will be discussed.

2.4.1 Drag Determination according to Aerodynamics

Power is required to overcome the aerodynamic force on the airship which opposes the airship velocity. Thus, in order to accurately estimate the mass of the power and propulsion system, we first need to estimate the drag forces at cruise speed and at maximum speed. The axial drag on hull and fins of the airship at low angles of attack is obtained as in [35] at cruise and maximum speeds as:

$$\begin{aligned} D_{Hcr} &= -q_{cr} C_{DH0} S_{HD} \cos^2 \alpha \ , & D_{Fcr} &= -q_{cr} C_{DF0} S_{FD} \cos^2 \alpha_F \\ D_{Hmax} &= -q_{max} C_{DH0} S_{HD} \cos^2 \alpha \ , & D_{Fmax} &= -q_{max} C_{DF0} S_{FD} \cos^2 \alpha_F \end{aligned} \tag{2.39}$$

where D_{Hcr} and D_{Fcr} are the drag forces on the hull and the fins at cruise speed respectively, D_{Hmax} and D_{Fmax} are the drag forces on the hull and the fins at maximum speed respectively, q_{cr} and q_{max} are the aerodynamic pressure at cruise and maximum speed respectively,α is the angle of attack of the hull and is computed from the local velocity at the center of buoyancy, C_{DH0} and C_{DF0} are the zero-angle axial drag coefficients of the hull and the fins respectively, which can be found from [44], S_{HD} and S_{FD} are the corresponding reference areas, and it is assumed that $S_{FD} = \eta_s S_{HD}$, where η_s is a constant.

The total drag on the airship can be decoupled into skin friction drag, form drag, trim drag, profile drag and so on [44].The total drag on three airships has been broken down by Durand (1934) [29]. This data is plotted in Fig. 2–5, from which we can find that the bare hull contributes about 50% of the total drag, while fins and rudders contribute approximately 15%.

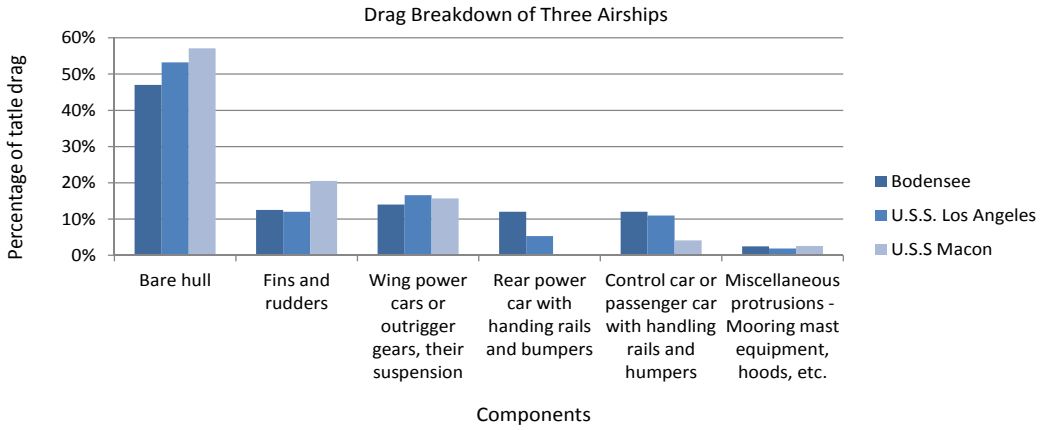

Figure 2–5: Drag Breakdown for Three Airships

More empirical data and formulas are required in order to get an accurate expression for the total drag on an airship. However, since the drag on the hull and the fins constitute the largest part of the total drag, the following equations are adopted to estimate the total drag at the conceptual design stage:

$$D_{cr} = \frac{D_{Hcr} + D_{Fcr}}{\eta_{D0}} , \qquad D_{max} = \frac{D_{Hmax} + D_{Fmax}}{\eta_{D0}} \tag{2.40}$$

where η_{D0} is the percentage of bare hull and fins drag contribution to the total drag. Based on Fig. 2–5[1] , we estimate $\eta_{D0} = 0.65$.

2.4.2 Conventional Power and Propulsion System

Many kinds of power and propulsion equipment can be used to power an aerial vehicle. The required engine power is calculated for steady state flight condition, in which thrust is equal to the drag. In steady state flight, the engine power required for cruising and maximum forward speed flights are calculated as follows [58]:

$$P_{cr} = \frac{1}{\eta_{eng}} T_{eng} v_{cr} = \frac{1}{\eta_{eng}} D_{cr} v_{cr} \tag{2.41}$$

$$P_{max} = \frac{1}{\eta_{eng}} T_{eng} v_{max} = \frac{1}{\eta_{eng}} D_{max} v_{max} \tag{2.42}$$

where T_{eng} is the thrust of the engine and η_{eng} is the propulsive efficiency. Stinton [62] plotted the variation of η_{eng} of propellers and ducted fans with airspeed in Fig. 2–6. The number of engines is determined as:

$$n_{eng} = \lceil \frac{\max\left(P_{cr}, P_{max}\right)}{P_{eng,1}} \rceil \tag{2.43}$$

where $P_{eng,1}$ is the power of the candidate engine. Therefore, the total mass of the engines is:

$$m_{eng} = n_{eng} m_{eng,1} \tag{2.44}$$

[1] For old large traditional airships, the power engines were mounted in different separate small cars, which were located at the bottom or lateral sides of these airships and very similar with gondola.

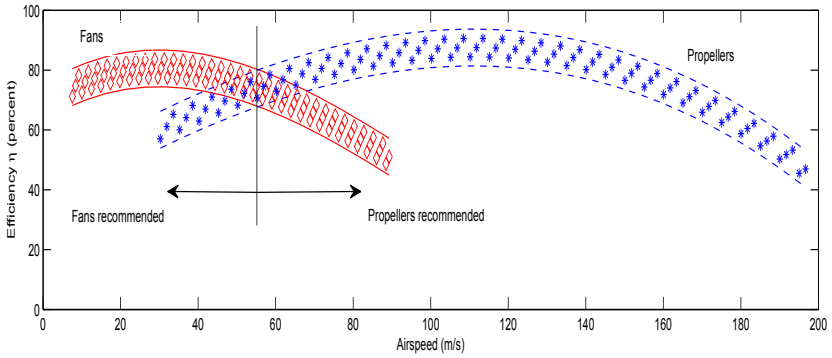

Figure 2–6: Variation of Propulsive Efficiency with Forward Speed (Based on Fig. 7-24 in [62])

where $m_{eng,1}$ is the mass of the candidate engine. Then, combining Eqs. (2.1, 2.39-2.42) together, the fuel needed for engines equals:

$$\begin{aligned} m_f =& (m_{eng,cr} P_{cr} t_{cr} + m_{eng,max} P_{max} t_{max}) \\ =& \frac{6^{\frac{2}{3}} \pi^{\frac{1}{3}} \lambda^{-\frac{2}{3}}}{8 \eta_{eng} \eta_{D0}} \left(m_{eng,cr} \rho_{cr} v_{cr}^3 t_{cr} + m_{eng,max} \rho_0 v_{max}^3 t_{max} \right) (C_{DH0} \cos^2 \alpha + \\ & C_{DF0} \eta_s \cos^2 \alpha_F) V_H^{\frac{2}{3}} \end{aligned} \tag{2.45}$$

where, $m_{eng,cr}$ is the cruise specific fuel consumption, $m_{eng,max}$ is the maximum specific fuel consumption, t_{cr} and t_{max} are the required cruise time and the maximum speed time for the airship. Then the mass of power and propulsion system is obtained as:

$$m_{prop} = m_{eng} + m_f \tag{2.46}$$

2.4.3 Unconventional Power and Propulsion System for Small Airships

There are two obvious disadvantages of conventional power and propulsion system: one is the heavy mass of conventional engines, and the other is the mass of fuel,

which increases rapidly with increase of flight duration (as in Eq. 2.45). In the case of novel small airship designs, their available lift is rather limited because of their size. Therefore, they cannot support the heavy power and propulsion systems used in conventional airships.

As an example of small unconventional airship, we consider the ALTAV airship used for research in the Aerospace Mechatronics Laboratory at McGill University. ALTAV has four power and propulsion units, mounted along the equator of the hull. The components of one unit and their masses are listed in Table 2–2.

Table 2–2: Mass Breakdown of Power and Propulsion Unit on ALTAV

Component	Type	Mass (g)
Brushless motor	PJS 3D-1000N	92
Constant pitch propeller	APC $0.305m(12")diameter \times 0.1m(3.8")$	51
Electronic speed controller	Jeti Adance 30-Plus	15
Servo motor	Hitec HS-322HD	43
Battery	12.64v, 4000mAh ThunderPower lithium polymer battery pack	338
Miscellaneous		150
Total mass		698

The existing methods to calculate the drag for these novel small airships can still be used. At present, however, there is no standard method to calculate the available thrust of a given propeller and motor system. The thruster forces in [54] and [9] are obtained experimentally. In addition to the battery that can provide enough power and time of flight for the motors, the speed controller and the servo motor is required. The mass of the unconventional power and propulsion system is obtained by adding up those of all components.

2.5 Airship Size Synthesis

Basic parameters and initial values of variables need to be provided as Preliminary Design Parameters, which will be used in the size minimization iteration. The input parameters are listed in Table 2–3[2] .

Table 2–3: Preliminary Design Parameters of a Nonrigid Airship

Input parameters	
Structure related	λ, AR, n_B, l, $\mathbf{r}_B$, l_{cv}, x_{Fs}, x_{Fe}, x_{Fms}, x_{Fme}, Φ_F
Motion related	h_{cr}, $\mathbf{v}_{cr}$, $\mathbf{v}_{max}$, t_{cr}, t_{max}, α_{max}, ω, trimmed values of $[\phi, \theta, \psi]^T$, $\mathbf{v}_w$
Fabric related	m_{H0}, m_{B0}, σ_{H0}, σ_{B0}, η_T
Mass related	$m_{eng,1}$, $m_{eng,cr}$, $m_{eng,max}$, m_{pay}, m_{str}, m_{sus}, m_{anc}
Safety related	$\eta_w = 1.5$, $\eta_{str} = 13.44‰$, $\eta_{sus} = 17.03‰$, $\eta_{anc} = 14.9‰$, $\eta_{wH} = 20‰$, $\eta_{wB} = 60‰$ $\eta_s = 176‰$
Initial variable for iteration	
Diameter of the maximum cross-section of the envelope	d

2.5.1 System Mass Estimation

In this thesis, the mass of an airship is decoupled into seven parts and is formulated as:

$$m_{total} = m_H + m_B + m_{prop} + m_{str} + m_{sus} + m_{anc} + m_{pay} \tag{2.47}$$

[2] The safety related parameters are from [17, 29], except η_s is from the geometric ratio of fin area to airship front area of Skyship-500

where m_H is the mass of envelope, m_B is the mass of ballonets, m_{str} is the mass of structural reinforcement system (including nose group), m_{sus} is the mass of suspension system (including gondola and its contents), m_{anc} is the mass of ancillary system (including components for maintenance, conduits and miscellaneous) and m_{pay} is the mass of payload.

The first assumption here is that the payload mass m_{pay} will not change with the increase or decrease of the airship envelope volume. The second assumption is that during sizing iteration, the mass of the structural reinforcement system, the suspension system and the ancillary system only change if the required diameter at the maximum cross section of the envelope is $\geq \pm 5\%$ different from the initial diameter value.

Equations for the power and propulsion system mass m_{prop} was developed in previous sections. Based on Eqs. (2.2) and (2.38), the envelope and ballonets mass are formulated as functions of the airship volume:

$$m_H = (1 + \eta_{wH})\, S_H = 1.651\,(1 + \eta_{wH})\, m_{H0} \pi^{\frac{1}{3}} \lambda^{-\frac{2}{3}} (1 + \lambda^2 \frac{\arccos(\frac{1}{\lambda})}{\sqrt{\lambda^2 - 1}}) V_H^{\frac{2}{3}} \tag{2.48}$$

and:

$$m_B = (1 + \eta_{wB})\, S_B = (1 + \eta_{wB})\, m_{B0}\, (4 n_B \pi)^{\frac{1}{3}}\, (3 \eta_{BH})^{\frac{2}{3}}\, V_H^{\frac{2}{3}} \tag{2.49}$$

where $\eta_{wH} = 2\%$ and $\eta_{wB} = 6\%$ are the recommended envelope and ballonets weight tolerances respectively [29]. The structural reinforcement system mass m_{str}, suspension system mass m_{sus} and ancillary system mass m_{anc} are highly dependent on mission requirements and designers preferences. However, the data on how they vary with envelope volume is lacking. Therefore, in this thesis, it is assumed that these

masses will increase linearly with the envelope volume expansion, and the scale factor η_{str}, η_{sus} and η_{anc} is obtained based on the mass decomposition of two different-size airships in [29]. Therefore, based on above assumptions, when the airship diameter of maximum cross-section deviates by more than 5% from its initial value, the masses m_{str}, m_{sus} and m_{anc} are calculated as:

$$m_{str} = m_{str,i}\left(1 + \eta_{str}\frac{V_H - V_{H,i}}{V_{H,i}}\right) = m_{str,i}\left(1 - \eta_{str}\right) + \frac{\eta_{str}}{V_{H,i}} m_{str,i} V_H \tag{2.50}$$

$$m_{sus} = m_{sus,i}\left(1 + \eta_{sus}\frac{V_H - V_{H,i}}{V_{H,i}}\right) = m_{sus,i}\left(1 - \eta_{sus}\right) + \frac{\eta_{sus}}{V_{H,i}} m_{sus,i} V_H \tag{2.51}$$

$$m_{anc} = m_{anc,i}\left(1 + \eta_{anc}\frac{V_H - V_{H,i}}{V_{H,i}}\right) = m_{anc,i}\left(1 - \eta_{anc}\right) + \frac{\eta_{anc}}{V_{H,i}} m_{anc,i} V_H \tag{2.52}$$

where $\eta_{str} = 13.44‰$ is the weight tolerance of the structure reinforce system mass, $\eta_{sus} = 17.03‰$ is the weight tolerance of the suspension system mass, $\eta_{anc} = 14.90‰$ is the weight tolerance of the ancillary system mass [29], the additional subscript i denotes the initial quantities in the sizing iteration.

Substituting Eqs. (2.46),(2.48-2.52) into Eq. (2.47), the gross weight of the airship system is obtained as a function of the hull volume:

$$\begin{aligned} W_{sys}\left(V_H\right) &= \left(m_{hul} + m_{bal} + m_{prop} + m_{str} + m_{sus} + m_{anc} + m_{pay}\right) g \\ &= a V_H + b V_H^{\frac{2}{3}} + c \end{aligned} \tag{2.53}$$

where a, b and c are defined as:

$$a = \left(\frac{\eta_{str}}{V_{H,i}} m_{str,i} + \frac{\eta_{sus}}{V_{H,i}} m_{sus,i} + \frac{\eta_{anc}}{V_{H,i}} m_{anc,i}\right) g$$

$$b = (1.651\,(1+\eta_{wH})\,m_{H0}\pi^{\frac{1}{3}}\lambda^{-\frac{2}{3}}\left(1+\lambda^2\frac{\arccos(\frac{1}{\lambda})}{\sqrt{\lambda^2-1}}\right)+(1+\eta_{wB})\,m_{B0}$$

$$(4n_B\pi)^{\frac{1}{3}}\,(3\eta_{BH})^{\frac{2}{3}}+0.4127\frac{\pi^{\frac{1}{3}}}{\eta_{eng}\eta_{D0}}\left(m_{eng,cr}\rho_{cr}v_{cr}^3t_{cr}+m_{eng,max}\rho_0v_{max}^3t_{max}\right)$$

$$(C_{DH0}\lambda^{-\frac{2}{3}}\cos^2\alpha+C_{DF0}\eta_s\lambda^{\frac{1}{3}}\cos^2\alpha_F))g$$

$$c = (m_{str,i}\,(1-\eta_{str})+m_{sus,i}\,(1-\eta_{sus})+m_{anc,i}\,(1-\eta_{anc})+m_{eng}+m_{pay})\,g$$

2.5.2 Sizing Constraint and Iteration

On the preliminary conceptual design stage, the airship system is required to generate enough net static lift to overcome the airship weight during flight. For conventional airships, the net static lift is always larger than or equal to the estimated system weight. For novel airships, such as the heavy-lift and almost-heavier-than-air designs, propulsion system can generate part of the lift, and the net static lift can be slightly smaller than the estimated system weight. Therefore, size minimization of the airship should lead to minimum discrepancy between the net static lift and the estimated system weight:

$$(V_H)_{min} = \arg\min_V\{\min\{L_{n0}\,(V_H)\,,L_{n,cr}\,(V_H)\}-\eta_wW_{sys}\,(V_H)\} \tag{2.54}$$

where η_w is the weight tolerance of the system. When $\eta_w \geq 1$, the design is for conventional airships, and when $0 < \eta_w < 1$, the design is for heavy-lift airships. In the absence of specific requirements, η_w is equal to 1.5 for conventional airships according to [17].

2.6 Validation of Non-rigid Airship Size Minimization

In this section, we apply the proposed sizing method to conventional airships with and without fins, and heavy-lift airships with and without fins. First, we want to validate whether the proposed method is effective in obtaining the minimum airship size in airship conceptual design procedure. Second, we want to compare the sizing results of airships with fins and without fins, so as to see which one can provide the smallest size.

To achieve these aims, we propose the same mission requirement, and use the same membrane and engines for these airships. Based on Table 2–3, we list the initial input parameters in two groups: one contains the parameters which remain constant during the sizing procedure, in Table 2–4[3] ; the other contains the initial values of parameters which change with size, in Table 2–5[4] . Based on recent existing airships, the minimum number of engines is assumed to be two for non-rigid airship with fins, and four for non-rigid airship without fins. The engine we choose at here is AR731-38BHP by UAV ENGINES LTD, which is commonly used in contemporary UAV design [11] because of its high power to weight ratio for a rotary engine.

The sizing algorithm is formulated as showen in the sizing flow chart Fig. 2–1. The initial maximum diameter is set to 5 m. The sizing results for non-rigid

[3] The units used in these tables are International System of Units (SI): Φ_F(rad), h_{cr}(m), $\mathbf{v}_{cr}$(m/s), $\mathbf{v}_{max}$(m/s), t_{cr}(h), t_{max}(h), α_{max}(deg), ω(deg/s), $[\phi, \theta, \psi]^T$(deg), $\mathbf{v}_w$(m/s), m_{H0}(kg/m^2), m_{B0}(kg/m^2), σ_{H0}(N/m), σ_{B0}(N/m)

[4] The structure related parameters are calculated based on the geometric relationship of different parts of Skyship-500.

Table 2–4: Input Parameters That Do Not Change With Airship Size

Structure related		Motion related		Fabric related		Mass related	
λ	3.623	h_{cr}	500	m_{H0}	0.15	m_{eng0}	AR731-38bhp
AR	1.5083	$\mathbf{v}_{cr}$	$[8,0,0]^T$	m_{B0}	0.15	$m_{eng,cr}$	AR731-38bhp
n_B	2	$\mathbf{v}_{max}$	$[14,0,0]^T$	σ_{H0}	10^5	$m_{eng,max}$	AR731-38bhp
Φ_F	$[0,0.5,1,1.5]\pi^T$	t_{cr}	40	σ_{B0}	10^5		
		t_{max}	5	η_T	1.5		
		α_{max}	30				
		ω	$[2.5,10,10]^T$				
		$[\phi,\theta,\psi]^T$	$[0,10,0]^T$				
		$\mathbf{v}_w$	$[1,1,1]^T$				

Table 2–5: Initial Value of Input Parameters That Change With Airship Size

Structure related (m)				Mass related (kg)	
d	5	x_{Fs}	13.11	m_{pay}	30
l	18.12	x_{Fe}	16.36	m_{str}	5
$\mathbf{r}_B$	$[0,0,0.05]^T$	x_{Fms}	14.01	m_{sus}	5
l_{cv}	8.56	x_{Fme}	16.36	m_{anc}	5

airships with fins are listed in Table 2–6, and the sizing results for non-rigid airships without fins are listed in Table 2–7, all of which have obtained from the same initial conditions.

Table 2–6: Output Results of Airship with Fins

Outputs / η_w	d (m)	V_H (m^3)	V_B (m^3)	L_{n0} (N)	$L_{n,cr}$ (N)	$\eta_w W_{sys}$ (N)
1.5 (conventional)	4.59	182.25	10.11	1710.77	1633.12	1630.81
0.98 (heavy-lift)	3.79	103.27	5.73	969.46	925.46	924.97

From Tables 2–6 and 2–7, we can see that the proposed sizing method resulted in a decrease of the initial maximum diameter from 5 m to 3.79 m for heavy-lift airship with fins, to 4.08 m for heavy-lift airship without fins, to 4.59 m for conventional

Table 2–7: Output Results of Airship without fins

Outputs / η_w	d (m)	V_H (m^3)	V_B (m^3)	L_{n0} (N)	$L_{n,cr}$ (N)	$\eta_w W_{sys}$ (N)
1.5 (conventional)	4.91	224.55	12.45	2108.00	2012.32	2004.18
0.98 (heavy-lift)	4.08	129.79	7.20	1218.46	1163.15	1156.55

airship with fins, and to 4.91 m for conventional airship without fins. In both tables, we find that the calculated minimum sizes of these airships provide just enough lift for their estimated system weights, which shows that the sizing method is effective at finding the minimum size based on the proposed mission requirements. Both sets of results show that, the size of heavy-lift airships can be smaller than that of conventional airships which generate all lift from buoyancy. Since heavy-lift airships use engines to generate part of the lift, the fuel consumption of heavy-lift airships increases more quickly with mission time than conventional airships. However, for a two day mission, heavy-lift airships require smaller size. Furthermore, without further discussing about the maneuvering advantages of non-rigid airships without fins, for both conventional and heavy-lift designs using the same membrane and engine and taking the same mass of payload, airships with fins can achieve smaller size for the same mission requirements than airships without fins. The main reason for this result is that three or four, or even more engines need to be adopted for airship control due to lack of fins, and the mass of the added engines is always larger than the original fin structures.

CHAPTER 3
ALTAV Maneuverability Metrics and Tests

As noted in Chapter 1, airship maneuverability has not been clearly defined until now. In this chapter, the maneuverability quantification method is introduced in the first two parts of this chapter based on the relevant tests and simulations conducted to date on ships, aircraft and airships. Then, the method is applied to quantify maneuverability of the small highly maneuverable airship ALTAV in the third part of this chapter. In Section 3.1, the reference coordinates and ALTAV dynamics model are provided. In order to define the airship maneuverability, the definition of heading angle is provided in Section 3.2. Then, a general airship maneuverability quantification method is introduced based on three maneuvering tests, in particular the straight forward maneuver, the turning maneuver and the zig-zag maneuver. One of the objectives of this thesis is to research the ALTAV maneuverability and how it is affected by its actuator locations. Furthermore, we wish to determine the optimal actuator location for ALTAV. Therefore, in Section 3.3, 64 different actuator locations along the equator of the hull in the $x-y$ body-fixed plane are defined, and simulations of the 3 aforementioned maneuvers based on the PID control strategy and the optimal control strategy are performed in order to reveal how ALTAV's maneuverability is affected by different actuator locations and control strategies.

3.1 Dynamic Model of Small Highly Maneuverable Airships

In this section, the dynamic model of a small highly maneuverable airship is provided. First, the airships researched in this thesis are treated as rigid bodies with six degrees of freedom (DOFs): three DOFs in translational directions (surge, sway and heave) and three DOFs in rotation (roll ϕ, pitch θ and yaw ψ). The inertial earth-fixed frame ($AXYZ$) and the local body-fixed frame ($Oxyz$) are represented respectively in Fig. 3–1.

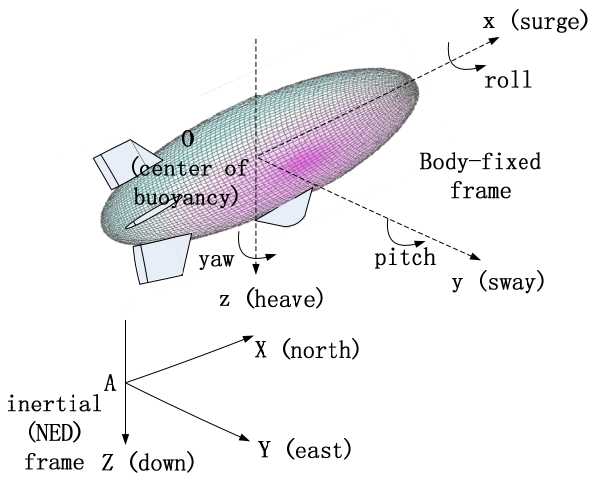

Figure 3–1: Small airship degree of freedom

The inertial earth-fixed frame is the geographic North-East-Down (NED) frame ($AXYZ$) whose X axis points toward the geographic north, Y axis points toward the east and Z axis points down. The origin of the body-fixed frame is located at the center of buoyancy (COB). The x axis points to the nose, the y axis points to the right side of the airship and the z axis is downward and perpendicular to the $x-y$ plane. Three Euler angles are used to define the direction cosine matrix (DCM)from

the geographic NED frame to the body-fixed frame is written as follows,

$$\begin{aligned}\mathbf{R}_{IB} &= \mathbf{R}_X(\phi)\mathbf{R}_Y(\theta)\mathbf{R}_Z(\psi) \\ &= \begin{bmatrix} \cos\psi\cos\theta & \sin\psi\cos\theta & -\sin\theta \\ \cos\psi\sin\theta\sin\phi - \sin\psi\cos\phi & \sin\psi\sin\theta\sin\phi + \cos\psi\cos\phi & \cos\theta\sin\phi \\ \cos\psi\sin\theta\cos\phi + \sin\psi\sin\phi & \sin\psi\sin\theta\cos\phi - \cos\psi\sin\phi & \cos\theta\cos\phi \end{bmatrix}\end{aligned} \tag{3.1}$$

The equations of motion of the small highly maneuverable airship ALTAV are expressed in body-fixed frame as [54]:

$$\begin{aligned}\bar{\mathbf{M}}_a \begin{bmatrix} \dot{\mathbf{v}} \\ \dot{\boldsymbol{\omega}} \end{bmatrix} = & \begin{bmatrix} -\boldsymbol{\omega}^\times \mathbf{M}_a \mathbf{v} + m\boldsymbol{\omega}^\times \mathbf{r}_{CG}^\times \boldsymbol{\omega} + \boldsymbol{\omega}^\times \mathbf{M}_{Da}\mathbf{v}_w - \mathbf{M}_{Da}\boldsymbol{\omega}^\times \mathbf{v}_w + \mathbf{M}_{Da}\dot{\mathbf{v}}_w \\ -m\mathbf{r}_{CG}^\times \boldsymbol{\omega}^\times \mathbf{v} - \boldsymbol{\omega}^\times \mathbf{J}_a \boldsymbol{\omega} - (\mathbf{v} - \mathbf{v}_w)^\times \mathbf{M}_{Da}(\mathbf{v} - \mathbf{v}_w) \end{bmatrix} \\ & + \begin{bmatrix} \mathbf{f}_V + \mathbf{f}_G \\ \mathbf{n}_V + \mathbf{n}_G \end{bmatrix} + \begin{bmatrix} \mathbf{f}_T \\ \mathbf{n}_T \end{bmatrix}\end{aligned} \tag{3.2}$$

where $\mathbf{v} = [u, v, w]^T$ and $\boldsymbol{\omega} = [p, q, r]^T$ denote the translational and rotational velocity vectors in body-fixed frame respectively, $\mathbf{r}_{CG}$ is the position vector from the COG to center of buoyancy (COB), $\mathbf{v}_w$ and $\dot{\mathbf{v}}_w$ are wind velocity and acceleration respectively, $\bar{\mathbf{M}}_a$ is the 6×6 mass matrix including the added mass, m is airship total mass, $\mathbf{M}_a$, $\mathbf{J}_a$ and $\mathbf{M}_{Da}$ are apparent mass, apparent inertia and apparent displaced mass matrices respectively, $\mathbf{r}_{CG}^\times$, $\boldsymbol{\omega}^\times$, and $(\mathbf{v} - \mathbf{v}_w)^\times$ are skew-symmetric matrices of corresponding vectors, $\mathbf{f}_V$ and $\mathbf{n}_V$, $\mathbf{f}_G$ and $\mathbf{n}_G$, and $\mathbf{f}_T$ and $\mathbf{n}_T$ are viscous, gravitational, actuator forces and moments respectively. In addition, the transformation of

the body components $[u, v, w, p, q, r]^T$ to $[\dot{x}, \dot{y}, \dot{z}, \dot{\phi}, \dot{\theta}, \dot{\psi}]^T$ is achieved by:

$$\begin{bmatrix} \dot{x} \\ \dot{y} \\ \dot{z} \\ \dot{\phi} \\ \dot{\theta} \\ \dot{\psi} \end{bmatrix} = \begin{bmatrix} \mathbf{R}_{IB} & 0 \\ 0 & \mathbf{S} \end{bmatrix}^{-1} \begin{bmatrix} u \\ v \\ w \\ p \\ q \\ r \end{bmatrix} \tag{3.3}$$

in which

$$\mathbf{S} = \begin{bmatrix} 1 & 0 & -\sin\theta \\ 0 & \cos\phi & \sin\phi\cos\theta \\ 0 & -\sin\phi & \cos\phi\cos\theta \end{bmatrix} \tag{3.4}$$

3.2 Airship Maneuverability Quantification

In order to optimize the maneuverability of ALTAV, we need to quantify maneuverability first. Three maneuvers are proposed in this thesis based on the previous research on ships, airships and aircraft: the straight forward maneuver, the turning maneuver and the zig-zag maneuver. These three maneuvers are frequently used to test ships, airships or aircraft maneuverability, and they can also be applied for general airships maneuverability quantification.

Heading angle ψ_H is one of the most important variables to define in the airship turning maneuvers. It is defined as the angle between the airship absolute velocity direction and the North direction. Since the North direction can be directly detected

by sensors, it is easier to use the North rather than the East as the direction reference. The heading angle for a full 360° clockwise turn is depicted in Fig. 3–2.

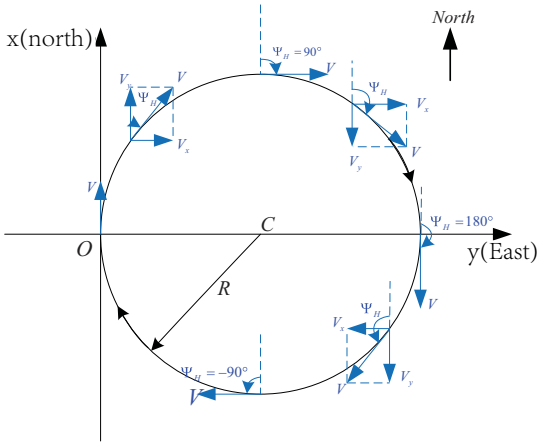

Figure 3–2: Heading angle

3.2.1 Maneuverability Quantification Based on Straight Forward Maneuver

The notion of straight forward maneuver (SFM) was first introduced in ship maneuverability quantification in [6]. It is also the most common maneuver for aerial vehicles, and is widely used when aerial vehicles fly in a trimmed condition, avoid obstacles, and leave or arrive at a hangar etc. An example of ALTAV SFM path is shown in Fig. 3–3 (a), in which the arrow shows the heading direction of the airship at the starting point O.

The parameters used to quantify SFM include: the terminal time t_f for pre-requested maneuver distance s (Fig. 3–3 (b), or the terminal distance s for pre-requested terminal time t_f), the deviation L in the lateral direction from the desired straight path (Fig. 3–4 (a)), the deviation H in vertical direction from the desired straight path (Fig. 3–4 (b)). A good SFM should have a small t_f for a specified s

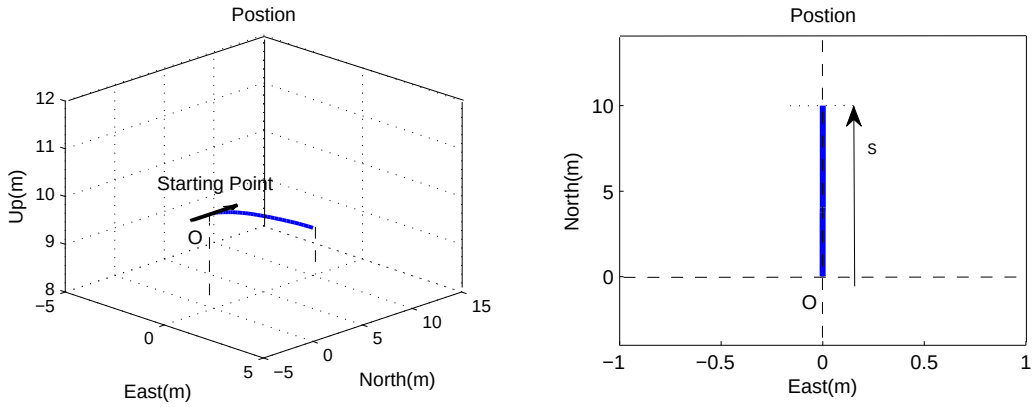

(a) In 3D Space (b) In $X-Y$ plane

Figure 3–3: ALTAV straight forward maneuver with present actuator locations

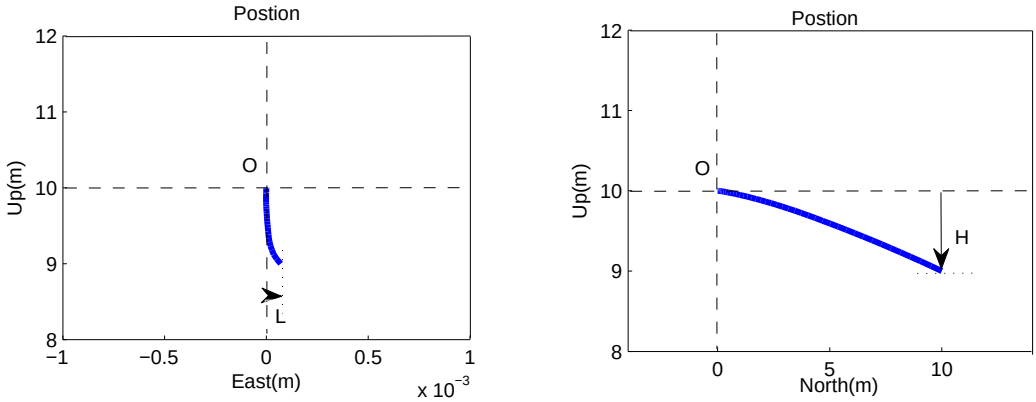

(a) In $X-Z$ plane (b) In $Y-Z$ plane

Figure 3–4: ALTAV straight forward maneuver with present actuator locations

(or a large s for a specified t_f), and small lateral and vertical deviations during the whole maneuver.

3.2.2 Maneuverability Quantification Based on Turning Maneuver

Turning maneuver (TM) is considered as one of the most important maneuvers for any vehicle. The turning maneuverability tests are widely used for ships, aircraft and airship assessment and in literature on the subject of maneuverability [6,8,47,48].

The terminal turning angle ψ_f in TM tests is usually an integer multiple of 90°. An example of ALTAV 360° clockwise TM path is shown in Fig. 3–5 (a).

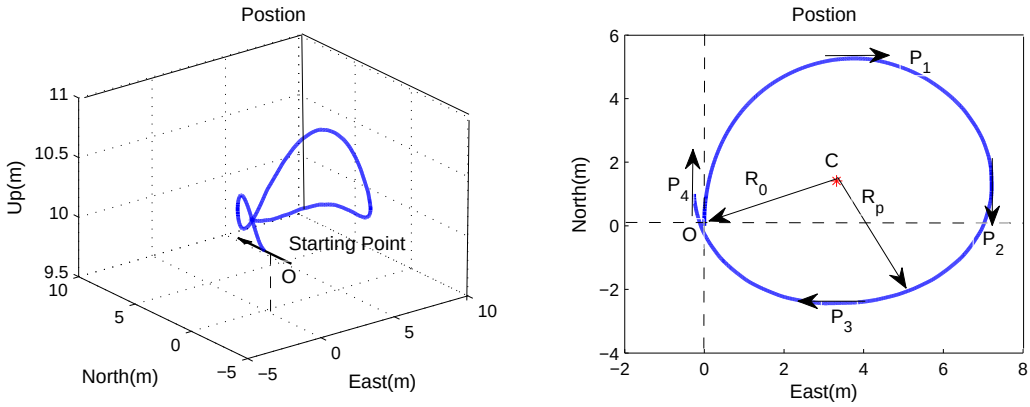

(a) In 3D Space (b) In $X-Y$ plane

Figure 3–5: ALTAV 360° turning maneuver with present actuator locations

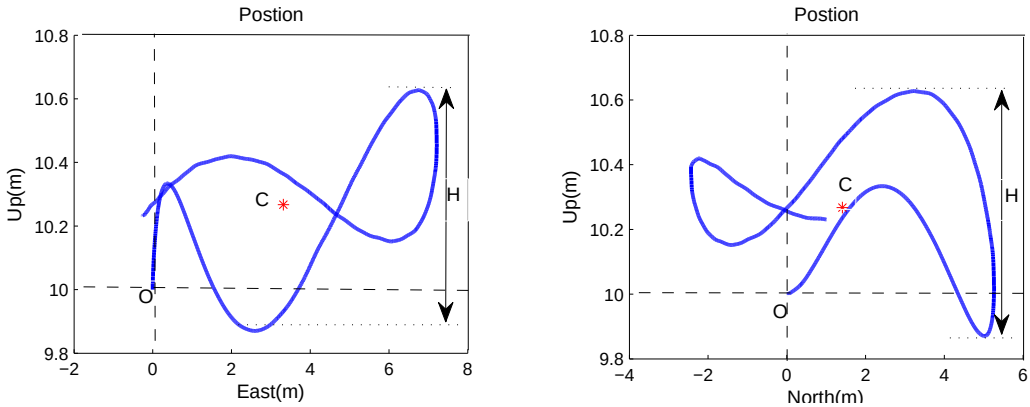

(a) In $X-Z$ plane (b) In $Y-Z$ plane

Figure 3–6: ALTAV 360° turning maneuver with present actuator locations

The parameters used to quantify TM include: the terminal time t_f for desired turning angle ψ_f ($\psi_f = 360°$ in Fig. 3–5 (a)), or the terminal turning angle ψ_f for desired terminal time t_f, the distance R_0 from the turning center C to the starting

point, the average turning radius R_p, and the vertical deviation H. For a $\psi_f = 360°$ turning maneuver, if the turning trajectory is recorded through N spatial points $(x_i, y_i, z_i)_{i=1,\cdots,N}$, the coordinate of the center point C(x_c, y_c, z_c)(Fig. 3–5 (b)) of the TM is calculated as $x_c = \sum_{i=1}^{i=N} x_i/N$, $y_c = \sum_{i=1}^{i=N} y_i/N$ and $z_c = \sum_{i=1}^{i=N} z_i/N$. The points P_1, P_2, P_3 and P_4 (see Fig. 3–5 (b)) denote locations where the heading angle first achieves 90°, 180°, 270° and 360°. Then R_0 is defined as $R_0 = \sqrt{x_c^2 + y_c^2 + z_c^2}$ (Fig. 3–5 (b)), and R_p is defined as $R_p = \sum_{i=1}^{i=N} \sqrt{(x_i - x_c)^2 + (y_i - y_c)^2 + (z_i - z_c)^2}/N$ (Fig. 3–5 (b)). The deviation H in the vertical direction is the distance between the maximum and the minimum deviations from the desired turning plane height z_d (Fig. 3–6). A good turning maneuver should have a small t_f for a specified ψ_f (or a large ψ_f for a specified t_f), small R_0, R_p and H during the entire TM.

3.2.3 Maneuverability Quantification Based on Zig-zag Maneuver

The zig-zag maneuver (ZZM) has not been used as a measure of maneuverability of airships before, but it has been suggested for ship maneuverability tests in [33, 34, 45]. An example of ALTAV ZZM path is shown in Fig. 3–7 (a). A typical ZZM can be approximated by a series of straight forward maneuvers and turning maneuvers, following one after the other. The zig-zag maneuver test provides a good mechanism to assess maneuverability of an airship, and the revealed maneuvering characteristics of an airship can better reflect its maneuverability in real flight than other maneuvers.

The parameters used to quantify ZZM include: the terminal time t_f for desired number of repeated zig-zag cycles N_f ($N_f = 5.5$ in Fig. 3–7 (b)), or N_f for desired terminal time t_f, the forward maneuver distance s (Fig. 3–7 (b)), the distance d between the maximum and the minimum deviations in the lateral direction in the

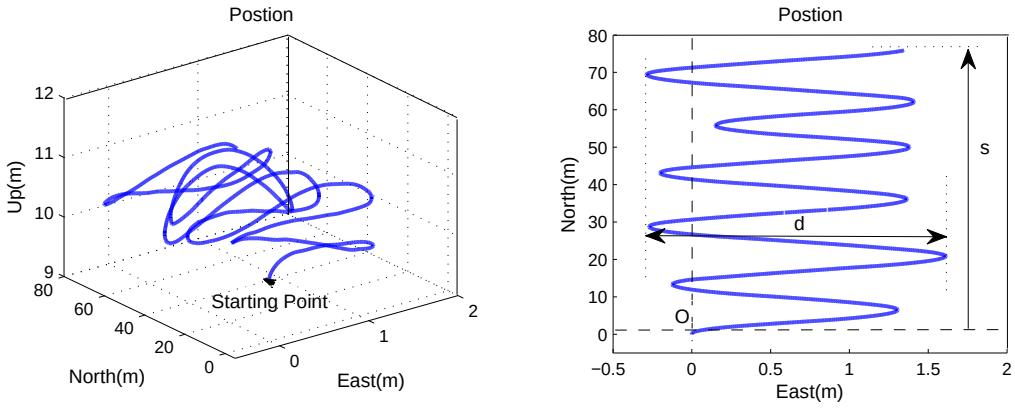

(a) In 3D space (b) In $X-Y$ plane

Figure 3–7: ALTAV zig-zag maneuver with present actuator locations

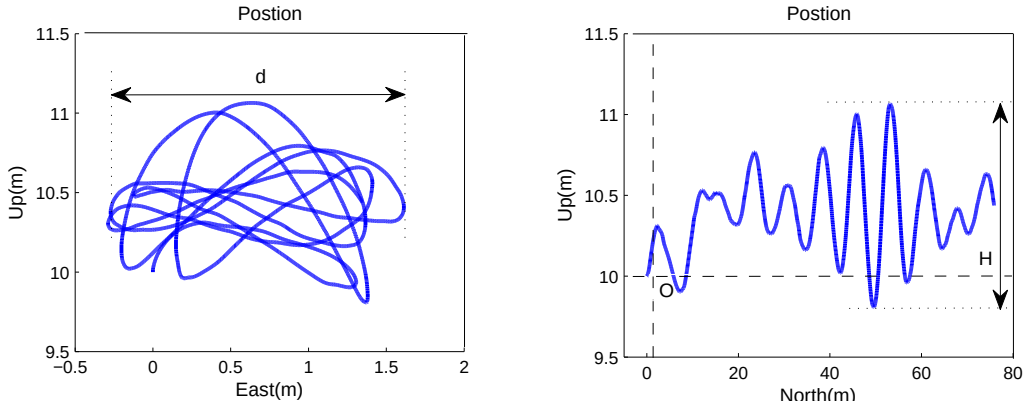

(a) In $X-Z$ plane (b) In $Y-Z$ plane

Figure 3–8: ALTAV zig-zag maneuver with present actuator locations

horizontal plane (Fig. 3–8 (a)), and the deviation H between the maximum and the minimum vertical positions (Fig. 3–8 (b)). A good zig-zag maneuver should have small t_f for a specified N_f (or a high N_f for a specified t_f), small s, d and H over the whole ZZM.

3.3 Maneuverability Differences for Changing Actuator Locations

One aim of the thesis is to find the optimal actuator placement that can provide ALTAV the best maneuverability. As mentioned before, ALTAV has four vectorable thrusters along the equator of $X-Y$ plane. Two of them are located in the forward part of ALTAV at the same x-coordinate x_{act1}; the other two are located at the rear of ALTAV at the same x-coordinate x_{act2}. The coordinates of the four actuators are denoted as (x_{act1}, y_{act1}), $(-x_{act2}, y_{act2})$, $(-x_{act2}, -y_{act2})$ and $(x_{act1}, -y_{act1})$ respectively $(x_{act1} > 0, x_{act2} > 0, y_{act1} > 0, y_{act2} > 0)$. From Eq. (3.2), it can be seen that ALTAV acceleration $\dot{\mathbf{v}}$ and angular acceleration $\dot{\boldsymbol{\omega}}$ are affected by the actuator locations. Before determining the optimal actuator locations to provide ALTAV the best maneuverability, we first choose a set of actuator locations and perform a serious of simulations, so as to get a general view of how ALTAV's maneuverability is affected by different actuator locations.

The set of feasible actuator locations is selected as in Fig. 3–9, where the feasible location has the same distance to the surface of the airship. In particular, eight locations are selected in the front of ALTAV (from A1 to A4a) and eight locations are selected at the rear of ALTAV (from A5a to A9) to give a reasonable refinement of possible actuator locations (distance between the A-stations is $\approx 0.3 - 0.4$ m). For each simulation, a pair of actuators in the front is combined with a pair of actuators in the rear of ALTAV. Therefore, there are $8 \times 8 = 64$ actuator location combinations used to perform the required maneuverability simulations, from which a basic understanding of how ALTAV's maneuverability is affected by different actuator locations and control strategies can be acquired.

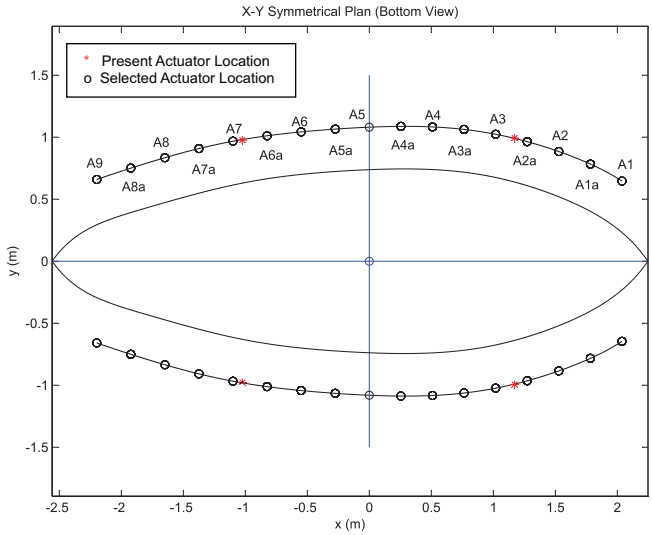

Figure 3–9: Selected actuator locations

The effect of control law on ALTAV maneuverability is also taken into account in this thesis, so as to understand whether the optimal actuator locations will vary due to different control laws. Four groups of maneuver simulations are used in this thesis to explore how ALTAV's maneuverability is affected by actuator placement and control laws:

- $\psi_f = 360°$ turning maneuver based on PID control strategy;
- Zig-zag maneuver based on PID control strategy;
- Straight forward maneuver based on optimal control strategy;
- $\psi_f = 180°$ turning maneuver based on optimal control strategy.

The original prototype of ALTAV is controlled by PID control strategy. Five separate PID controllers are used to control the forward speed u, the altitude h, and the three Euler angles ϕ, θ and ψ. The outputs of the five controllers are the angle

and magnitude control commands for the four thrusters in the $x-z$ plane of the body-fixed frame. A detailed description of ALTAV's PID controllers can be found in [54]. The PID parameters used in the turning and zig-zag maneuvers are listed in Table 3–1.

Table 3–1: PID Parameters in the $\psi_f = 360°$ Turning Maneuver and the Zig-zag Maneuver

	u	ϕ	θ	ψ	h
k_P	0.75	0.05	0.28	0.25	0.37
k_I	0	0.01	0.01	0	0
k_D	0	-0.07	-0.22	-0.1	-0.25

The initial conditions for both 360° turning and zig-zag maneuvers are the same, and the desired u_d, ϕ_d, θ_d and h_d are also the same in both maneuvers, which are listed in Table 3–2. In order to better explore ALTAV system responses to actuator control signals, we conduct all simulations with no wind conditions.

Table 3–2: Initial Conditions (IC) and Desired PID Control Values (DPCV) in the $\psi_f = 360°$ Turning Maneuver and the Zig-zag Maneuver

IC	360° TM	ZZM	DPCV	360°TM	ZZM
$\mathbf{v}$ (m/s)	$[0.5, 0, 0]^T$	$[0.5, 0, 0]^T$	u_d (m/s)	0.5	0.5
$\boldsymbol{\omega}$ (deg/s)	$[0, 0, 0]^T$	$[0, 0, 0]^T$	ϕ_d (deg)	0	0
$[x, y, z]^T$ (m)	$[0, 0, -10]^T$	$[0, 0, -10]^T$	θ_d (deg)	0	0
$[\phi, \theta, \psi]^T$ (deg)	$[0, 0, 0]^T$	$[0, 0, 0]^T$	ψ_d (deg)	Algorithm 1	Algorithm 2
$\mathbf{v}_w$ (m/s)	$[0, 0, 0]^T$	$[0, 0, 0]^T$	h_d (m)	-10	-10
$\dot{\mathbf{v}}_w$ (m/s^2)	$[0, 0, 0]^T$	$[0, 0, 0]^T$			

The optimal control problem in this thesis is solved by using GPOPS, which is a MATLAB toolbox written for solving multiple-phase optimal control problems. GPOPS uses open-loop control strategy. In ALTAV optimal maneuver problem,

GPOPS is supposed to generate the best control strategy based on provided dynamic system model, cost function, initial conditions, state constraints, and phase links. In ALTAV maneuver simulations, GPOPS is very powerful in minimizing the provided cost function. However, GPOPS consumes a lot of computing resources in searching a solution, and due to its open-loop character, it is difficult to adapt GPOPS to ALTAV actual flight control. From [55], given a set of P phases, the optimization problem is formed as follows. The cost function in GPOPS is defined as:

$$\begin{aligned} J &= \Sigma_{p=1}^{P} J^{(p)} \\ &= \Sigma_{p=1}^{P} \left[\Phi^{(p)} \left(\mathbf{x}^{(p)}(t_0^{(p)}), t_0^{(p)}, \mathbf{x}^{(p)}(t_f^{(p)}), t_f^{(p)}; \mathbf{q}^{(p)} \right) + \int_{t_0^{(p)}}^{t_f^{(p)}} \mathcal{L}^{(p)} \left(\mathbf{x}^{(p)}(t), \mathbf{u}^{(p)}(t), t; \mathbf{q}^{(p)} \right) dt \right] \end{aligned} \tag{3.5}$$

subject to the dynamic constraint:

$$\dot{\mathbf{x}}^{(p)} = \mathbf{f}^{(p)} \left(\mathbf{x}^{(p)}, \mathbf{u}^{(p)}, t; \mathbf{q}^{(p)} \right), \quad (p = 1, \cdots, P) \tag{3.6}$$

the boundary conditions:

$$\phi_{min} \leq \phi^{(p)} \left(\mathbf{x}^{(p)}(t_0^{(p)}), t_0^{(p)}, \mathbf{x}^{(p)}(t_f^{(p)}), t_f^{(p)}; \mathbf{q}^{(p)} \right) \leq \phi_{max}, \quad (p = 1, \cdots, P) \tag{3.7}$$

the inequality path constraints:

$$\mathbf{C}^{(p)} \left(\mathbf{x}^{(p)}(t), \mathbf{u}^{(p)}(t), t; \mathbf{q}^{(p)} \right) \leq 0, \quad (p = 1, \cdots, P) \tag{3.8}$$

and the phase continuity constraints:

$$\mathbf{P}^{(p)}\left(\mathbf{x}^{(p_l^s)}(t_f), t_f^{(p_l^s)}, \mathbf{q}^{(p_l^s)}; \mathbf{x}^{(p_u^s)}(t_0), t_0^{(p_u^s)}, \mathbf{q}^{(p_u^s)}\right) = \mathbf{0}, \quad (p_l, p_u \in [1, \cdots, P], s = 1, \cdots, L) \tag{3.9}$$

where $\mathbf{x}^{(p)}(t) \in \mathbb{R}^{n_p}$, $\mathbf{u}^{(p)}(t) \in \mathbb{R}^{m_p}$, $\mathbf{q}^{(p)} \in \mathbb{R}^{q_p}$ and $t \in \mathbb{R}$ are the state, control, static parameters and time in phase $p \in [1, \cdots, P]$ respectively. L is the number of phases to be linked, $p_l^s \in [1, \cdots, P], (s = 1, \cdots, L)$ are "left" phase numbers, and $p_u^s \in [1, \cdots, P], (s = 1, \cdots, L)$ are the "right" phase numbers. The details of the algorithm used to solve the multi-phase optimal control problem can be found in [7, 19–21, 56]. In ALTAV optimal control problem, $\mathbf{x}^{(p)}(t)$ is the state $[u, v, w, p, q, r, \dot{x}, \dot{y}, \dot{z}, \dot{\phi}, \dot{\theta}, \dot{\psi}]^T$, $\mathbf{u}^{(p)}(t)$ is the thruster control signals $(\mathbf{f}_T, \mathbf{n}_T)$, and $\mathbf{q}^{(p)}$ represents the actuator locations $(x_{act1}, x_{act2}, y_{act1}, y_{act2})$.

The numerical method which GPOPS uses to solve the optimal control problem falls into the category of *hp*-Adaptive Pseudospectral Methods, where h denotes the segment width and p represents the polynomial degree in each segment. In this *hp*-Adaptive Pseudospectral Methods, the number of segments, segment widths, and polynomial degrees vary throughout the time interval of interest.The iterative procedure for *hp*-Adaptive Pseudospectral Method used in GPOPS is summarized as follows [13]:

1. Initialize the specified optimal control problem and choose M collocation points, where the number M is determined by the user.
2. Solve the nonlinear programming problem (NLP) with the prescribed grid distribution.

3. Check for each segment whether the dynamic constraints, path constraints, and bounds on the state and control are satisfied to the user-defined tolerance ε in each segment at the midpoints between collocation points. For all segments not within the prescribed tolerance, continue to step (4) or step (5).
4. For all segments where the scaled midpoint residual vector β is of 'uniform-type' increase the number of collocation points in these segments by the user-specified amount L.
5. For all segments where the scaled midpoint residual vector β is of 'nonuniform-type', break the segments at all prescribed points and set M=5 in each new segment.
6. After all segments have been updated, return to step (2).
7. Terminate when the dynamic constraints, path constraints, and bounds on the state and control are satisfied to the tolerance ε in all segments.

3.3.1 PID Control Strategy: $\psi_f = 360°$ Turning Maneuver

In the $\psi_f = 360°$ PID turning maneuver simulations the initial conditions and the desired PID control values are listed in Table 3–2. In the $\psi_f = 360°$ PID turning maneuver simulation, the desired ψ_d is defined by using Algorithm 1, in which ψ_d increases from 10 deg to 360 deg in 10 deg increments. Once the yaw angle achieves 360°, the simulation stops. An example of ψ_d and ψ time histories is shown in Fig. 3–10. The simulated motion of the turning maneuver for the actuator location combination A3A7 is shown in Fig. 3–11. The length of the arrows in the figure is the same as the length of ALTAV, and the direction of the head of each arrow is the same as the direction of the head of ALTAV at the corresponding time instant. The

corresponding control signals and the states are displayed in Fig. 3–12 and Fig. 3–13 respectively.

Algorithm 1: Algorithm used to generate the current desired ψ_d for the Turning Maneuver with $\psi_f = 360°$, k starts from k=1;

Require:
Current ψ_i
Ensure:
Desired ψ_d

1: Load array $\psi_{des} = [10, 20, 30, ..., 350, 360]^T$ deg;
2: If $(\psi_i >= \psi_{des}(k))$ k=k+1;
3: $\psi_d = \psi_{des}(k)$;
4: If $(\psi_i >= \psi_{des}(36))$, exit;
5: **return** ψ_d.

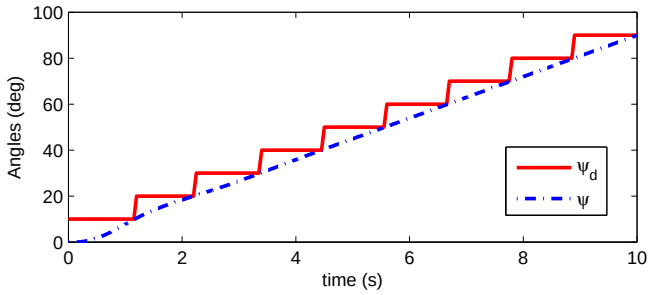

Figure 3–10: Time history of ψ_d and yaw angle ψ for $\psi_f = 360°$ turning maneuver, case A3A7

The magnitude and the angle limits on ALTAV's thrusters are $[-11, 11]$ N and $[-90, 90]$ deg respectively. From Fig. 3–12 (a), we observe that the actuators are under utilized with the current PID control strategy. Figure 3–13 shows that the yaw angle $\psi(t)$ increases to 360° as required. However, the yaw angular rate remains nearly constant at $r(t) \approx 9$ deg/s over the maneuver, and hence the yaw angle $\psi(t)$ only increases linearly based on this PID control strategy. Later in Section 3.3.4,

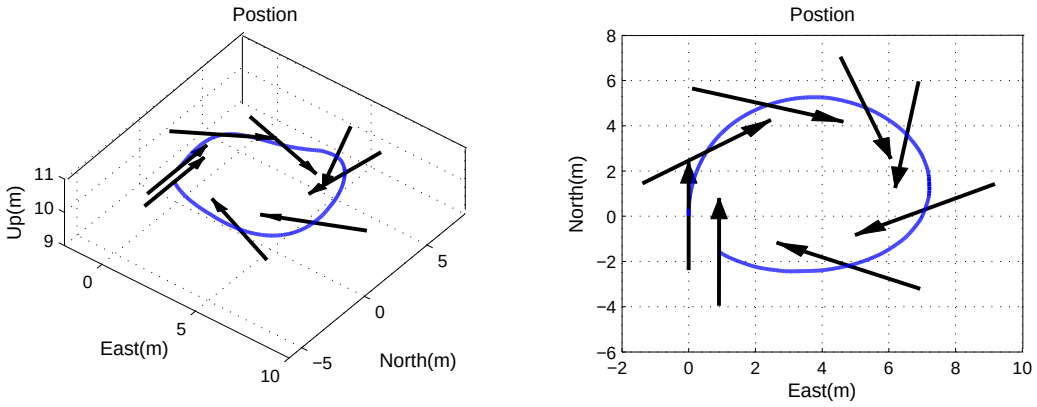

(a) In 3D Space (b) In $X-Y$ plane

Figure 3–11: The maneuver path for $\psi_f = 360°$ TM, case A3A7

with the optimal control strategy, we will observe that the yaw angle increases much faster.

Even under no wind condition, ALTAV is not able to complete the prescribed turning maneuver with all 64 actuator location combinations, as defined in the beginning of Section 3.3. With some actuator location pairs, the maneuver responses exhibit large oscillations in the vertical direction, sometimes resulting in divergence. Table 3–3 summarizes the maneuver times t_f for these maneuvers where the height deviation of the resulting trajectory is below ± 1 m for the desired z_d and R_0 and R_P are below 5 m.

Based on the results in Table 3–3, ALTAV finishes the required $\psi_f = 360°$ TM with 33 possible actuator location combinations. The shortest simulated turning time is 39.94 s, attained with actuator locations A2aA6a and A3aA6a; and the longest turning time is 40.38 s, obtained with actuator location A1A9. Since the differences in maneuver time are very small, these results show that the actuator placement

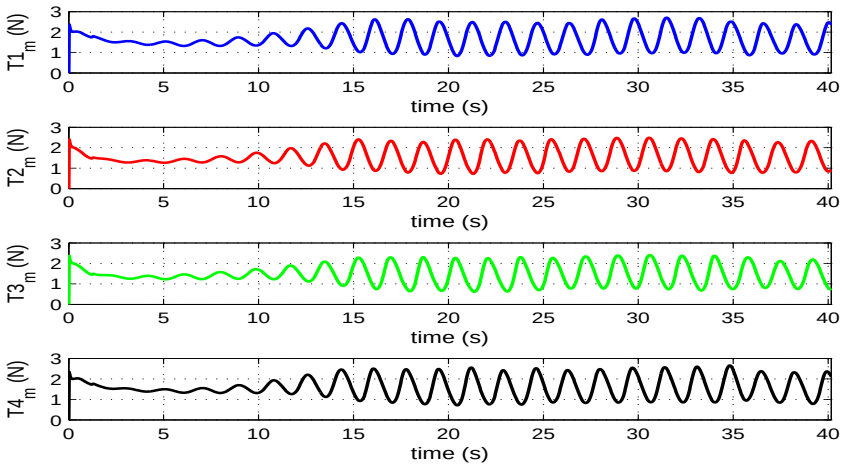

(a) Magnitude of thrust inputs

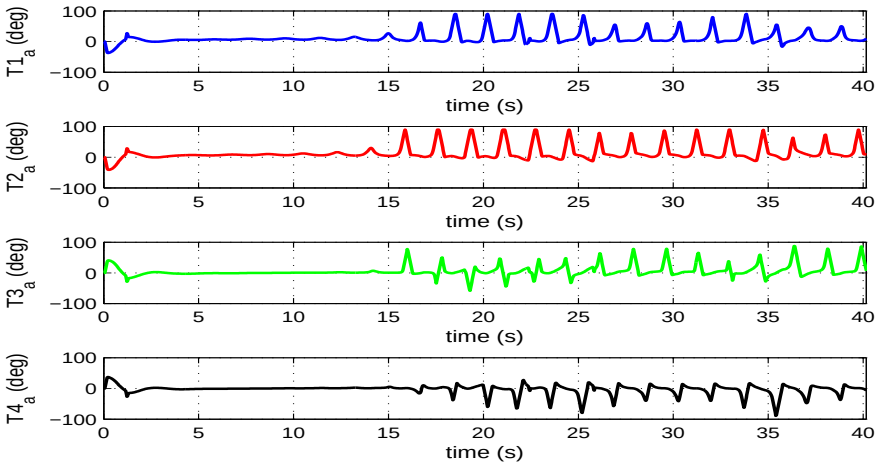

(b) Angles of thrust inputs

Figure 3–12: Time history of control signals for $\psi_f = 360°$ TM, case A3A7

does not have a significant effect on the speed of the turning maneuver, although a trend emerges showing that a large separation between front and rear actuators has an unfavorable effect on maneuverability. Actuator placement combinations of front

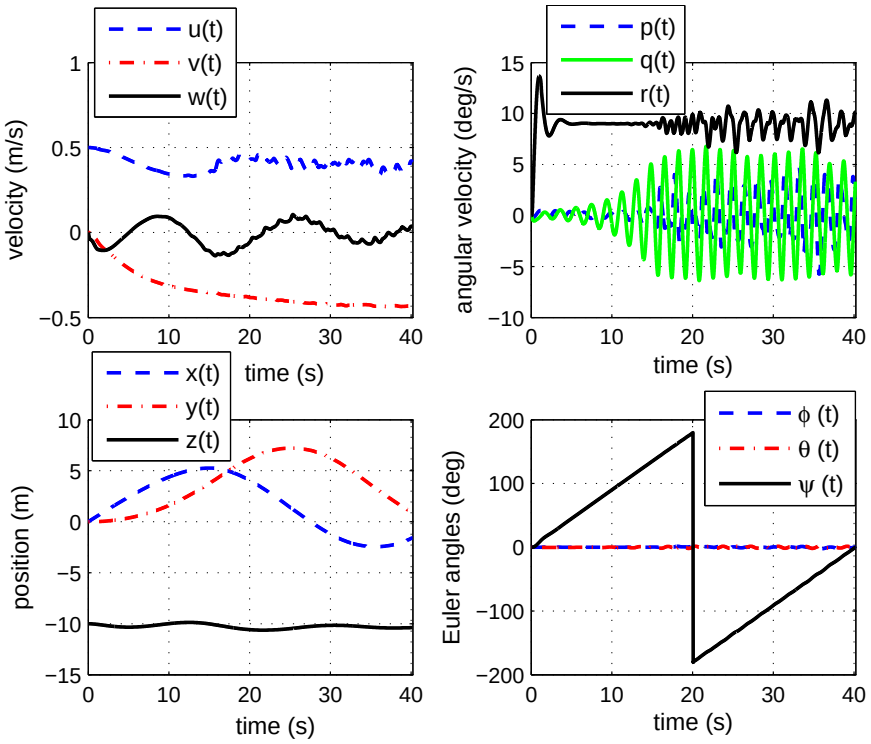

Figure 3–13: Time history of states for $\psi_f = 360°$ TM, case A3A7

Table 3–3: t_f (s) for $\psi_f = 360°$ PID Turning Maneuver ($\mathbf{v}_w = \mathbf{0}$ m/s, $\dot{\mathbf{v}}_w = \mathbf{0}$ m/s^2)

Case	A1	A1a	A2	A2a	A3	A3a	A4	A4a
A5a								39.95
A6						39.94	39.96	40.01
A6a				39.94	39.95	40.03	39.95	
A7		40.16	40.00	40.03	40.16	39.96		
A7a	40.15	40.09	40.09	40.12	40.04	39.95		
A8	40.23	40.20	40.18	40.14	40.04			
A8a	40.32	40.27	40.16	40.12	40.26			
A9	40.38	40.30	40.20	40.20				

thrusters near the nose and rear thrusters near the airship middle and the inverse of

these (front near the middle and rear near the stern) produce an unstable response of the airship which results in failure of the turning maneuver.

3.3.2 PID Control Strategy: Zig-zag Maneuver

The PID parameters, desired PID control values and initial conditions for zig-zag maneuver are listed in Tables 3–1 and 3–2. In order to perform an evident zig-zag maneuver, we require not only that the yaw angle achieves a desired value, but also the heading angle should achieve a specified value. In this zig-zag maneuver, the desired ψ_d is defined according to Algorithm 2, in which $\Psi_{H,i}$ is the current heading angle at discrete-time instant t_i and ψ_d is the desired yaw angle. One example of time histories of Ψ_H and ψ over 100 seconds for actuator placement case A3A7 is shown in Fig. 3–14. The time instant t_1 is the time instant when Ψ_H achieves 20 deg, which is an important parameter used to reflect ZZM response speed under this PID control strategy. An example of the trajectory for one circle of ZZM based on PID control is shown in Fig. 3–15. The corresponding control signals and the state responses are displayed in Fig. 3–16 and Fig. 3–17 respectively.

Algorithm 2: Algorithm used to get current desired ψ_d for zig-zag maneuver

Require:
Current heading angle $\Psi_{H,i}$ and last iteration $\Psi_{H,i-1}$;
Ensure:
Desired ψ_d
1: If ($\Psi_{H,i-1} < 20$ deg and $\Psi_{H,i} >= 20$ deg and $\psi_d = 40$ deg) $\psi_d = -40$ deg;
2: If ($\Psi_{H,i-1} > -20$ deg and $\Psi_{H,i} <= -20$ deg and $\psi_d = -40$ deg) $\psi_d = 40$ deg;
3: **return** ψ_d.

From Fig. 3–16(a), we can see that the four actuators are under utilized with current PID control strategy. Figure. 3–17 shows that the yaw angle $\psi(t)$ increases

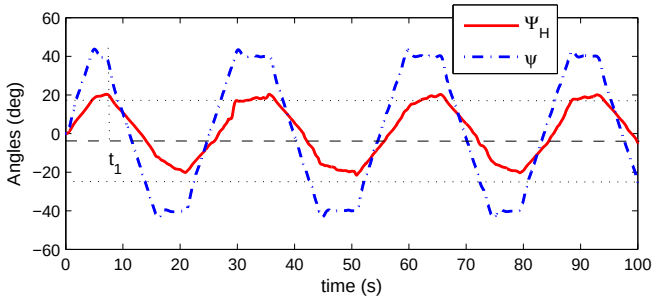

Figure 3–14: Time history of heading angle Ψ_H and yaw angle ψ of Zig-zag maneuver, case A3A7

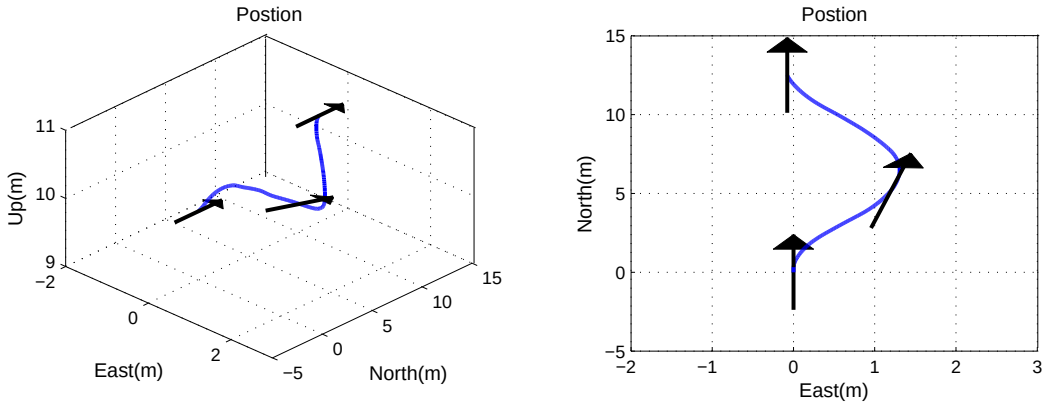

(a) In 3D Space

(b) In $X-Y$ plane

Figure 3–15: The maneuver path for one circle of ZZM, case A3A7

and decreases near linearly, and $r(t)$ oscillate around 9.37 deg/s from 3.4 s to 4.4 s and around -9.04 deg/s from 12 s to 15.6 s. At the end of 4.4 s, $\psi(t)$ changes from increase to decrease; and at the end of 15.6 s, $\psi(t)$ changes from decrease to increase. But $\psi(t)$ increases and decreases no more than linear relationship, which does not change as fast as that introduced under optimal control in Section 3.3.4.

As was the case with the turning maneuver, not all thruster combinations allow a successful completion of ZZM under PID control. The completion times of the

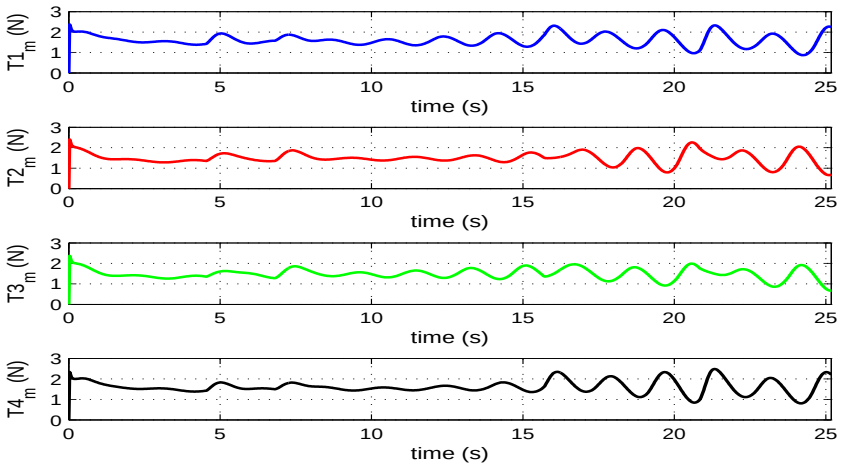

(a) Magnitude of thrust inputs

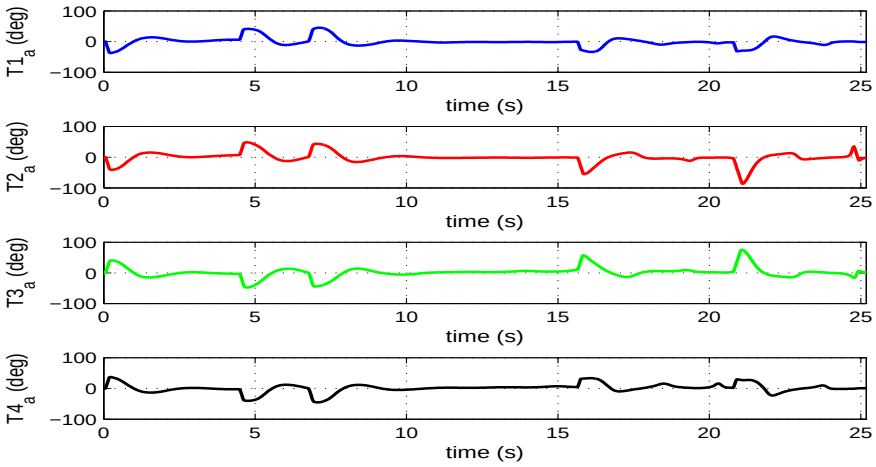

(b) Angles of thrust inputs

Figure 3–16: Time history of control signals for $N_f = 1$ ZZM, case A3A7

successful maneuvers for which the height deviations are $\leq \pm 1$ m, $s < 20$ m and $d \leq 6$ m are recorded in Table 3–4. In all, 30 actuator locations produce the required zig-zag maneuver. From Table 3–4, the shortest zig-zag maneuver time is 22.93 s,

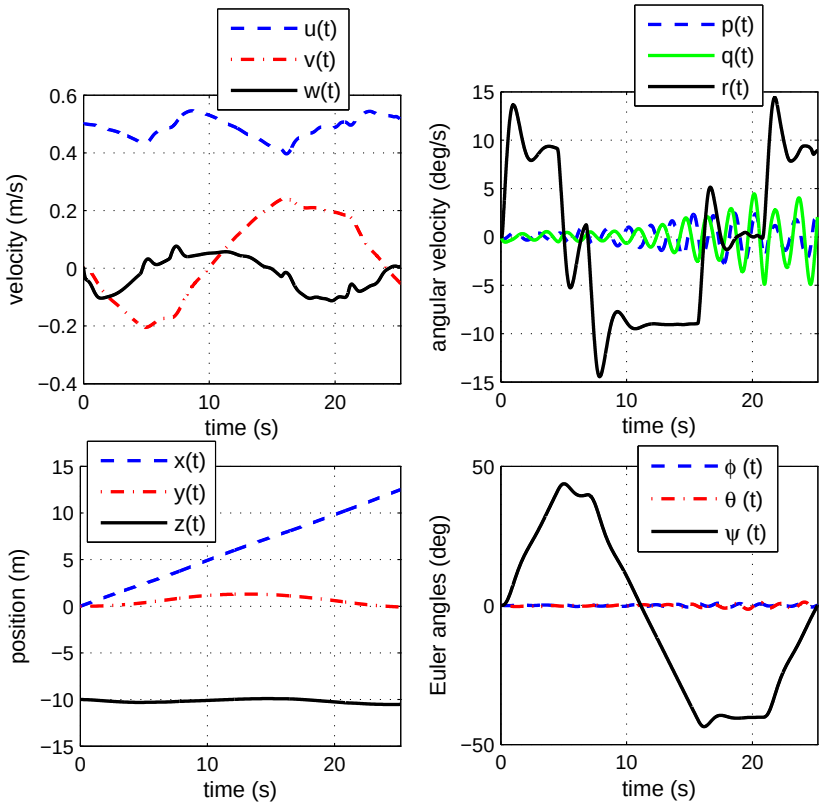

Figure 3–17: Time history of states for $N_f = 1$ ZZM, case A3A7

obtained for the actuator location case A3aA6; and the longest zig-zag maneuver time is 27.42 s for the actuator location case A4A6a. Qualitatively, the results for ZZM in Table 3–4 are very similar to those for TM in Table 3–3; in particular, the successful ZZMs are also successful TMs.

3.3.3 Optimal Control Strategy: Straight Forward Maneuver

In order to reveal if ALTAV's maneuverability is affected by the control strategy, the optimal controller is also implemented for ALTAV maneuver control. We employ

Table 3–4: t_f (s) for $N_f = 1$ Zig-zag Maneuver ($\mathbf{v}_w = \mathbf{0}$ m/s, $\dot{\mathbf{v}}_w = \mathbf{0}$ m/s^2)

Case	A1	A1a	A2	A2a	A3	A3a	A4	A4a
A5a								22.99
A6						22.93	24.79	27.07
A6a					23.17	25.21	27.42	
A7			23.18	23.75	25.18	25.72		
A7a	22.94	23.11	23.78	25.43	24.92	26.95		
A8	23.19	23.30	23.86	26.06	27.29			
A8a	23.47	23.72	26.23	26.82				
A9	23.70	26.36	26.52	26.52				

GPOPS to solve the optimal straight forward maneuver (OSFM) problem for ALTAV with the final location along the inertial set to X-direction $x_f = 10$ m. Although it would be desirable to use GPOPS to also find the optimal actuator locations, GPOPS is not efficient enough to solve such a complex optimal control problem. Besides, GPOPS failed to find a solution for multiple-phases maneuver of ALTAV, for example, the maneuver combining the straight forward flight and the turning maneuver, due to the complexity of ALTAV dynamics model. In these optimal maneuver simulations, the actuator locations are the same as before (represented by 64 combinations) as introduced in Fig. 3–9 and $\mathbf{q}$ is a constant in each case. There is only one phase in the straight forward optimal maneuver control, so that, $p = 1$ in Eq. (3.5). The cost function to be minimized is the maneuver time:

$$J = t_f \tag{3.10}$$

and the dynamic constraints are given by Eq. (3.2). A boundary of the form Eq. (3.7) cannot be too wide or too narrow. For the straight forward maneuver, we would like to ensure the lateral and vertical deviations L and H in Fig. 3–4 remain small, and

the forward speed u increases in this straight forward maneuver. After tuning the boundary conditions by trial and error, the boundary conditions used are listed in Table 3–5. An example of the trajectory for the straight forward maneuver based on the optimal control strategy is shown in Fig. 3–18. The corresponding control signals and the state responses are displayed in Fig. 3–19 and Fig. 3–20 respectively.

Table 3–5: Boundary Conditions for $x_f = 10$ m OSFM ($\mathbf{v}_w = \mathbf{0}$ m/s, $\dot{\mathbf{v}}_w = \mathbf{0}$ m/s)

	Boundary Conditions		Path Constraints on $\mathbf{x}(t)$	
	$\mathbf{x}(t_0)$	$\mathbf{x}(t_f)$	min	max
u (m/s)	0.5	free	0.3	free
v (m/s)	0	free	-0.1	0.1
w (m/s)	0	free	-0.1	0.1
p (deg/s)	0	free	-5	5
q (deg/s)	0	free	-16	16
r (deg/s)	0	free	-5	5
x (m)	0	10	0	10
y (m)	0	free	-1	1
z (m)	-10	free	-11	-9
ϕ (deg)	0	free	-10	10
θ (deg)	0	free	-30	30
ψ (deg)	0	free	-10	10

From Fig. 3–19, we observe that the four actuators achieve maximum thrust (11N) based on optimal control, which is expected for an open-loop control strategy to minimize time. The changes of the control signals under the optimal control strategy are milder than those under previous PID control strategy. Later in Chapter 4, we will show that due to ALTAV system characteristics, the less oscillatory control signals are better for ALTAV's maneuverability. From Fig. 3–20, we observe that the

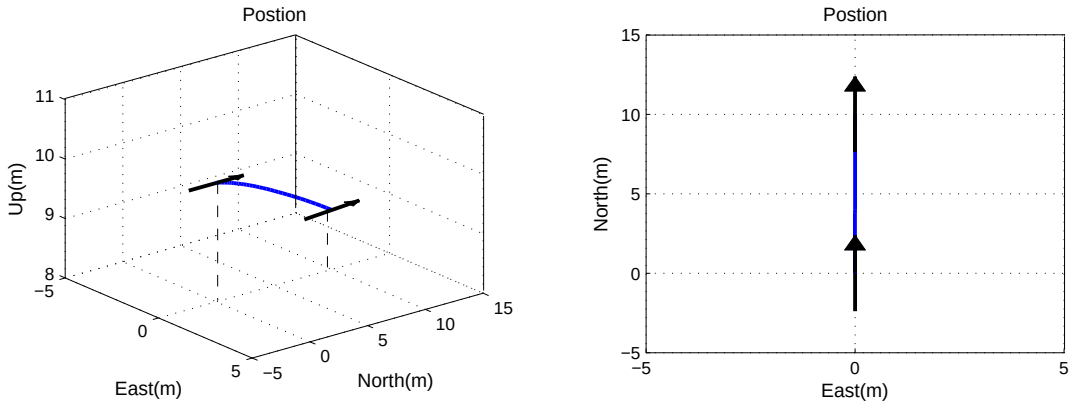

(a) In 3D Space (b) In $X-Y$ plane

Figure 3–18: The maneuver path for $x_f = 10$ m OSFM, case A3A7

forward velocity u steadily increases during the maneuver as we wish, and the other states of the airship satisfy the constraints imposed on them.

As was the case with the PID control strategy, not all of the 64 actuator combinations allow ALTAV to complete a 10 m SFM under the optimal control strategy. The results for the terminal time t_f for the successful 30 actuator locations are recorded in Table 3–6.

Table 3–6: t_f (s) for $x_f = 10$ m Optimal Straight Forward Maneuver ($\mathbf{v}_w = \mathbf{0}$ m/s, $\dot{\mathbf{v}}_w = \mathbf{0}$ m/s^2)

Case	A1	A1a	A2	A2a	A3	A3a	A4	A4a
A5a								
A6						3.03	1.98	1.72
A6a						1.75	1.72	1.73
A7			1.81	1.74	1.72	1.72	1.73	
A7a	1.76	1.74	1.73	1.72	1.72	1.72		
A8	1.73	1.72	1.72	1.72	1.72	1.73		
A8a	1.72	1.72	1.72	1.72	1.73			
A9	1.72	1.72	1.72	1.73				

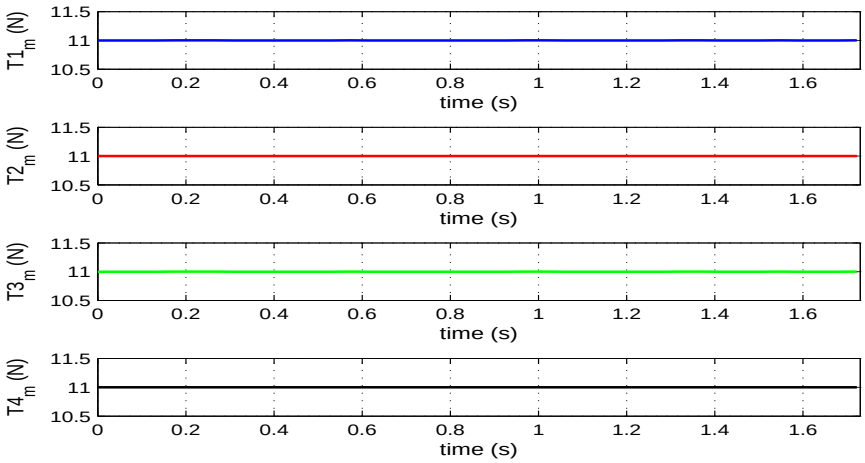

(a) Magnitude of thrust inputs

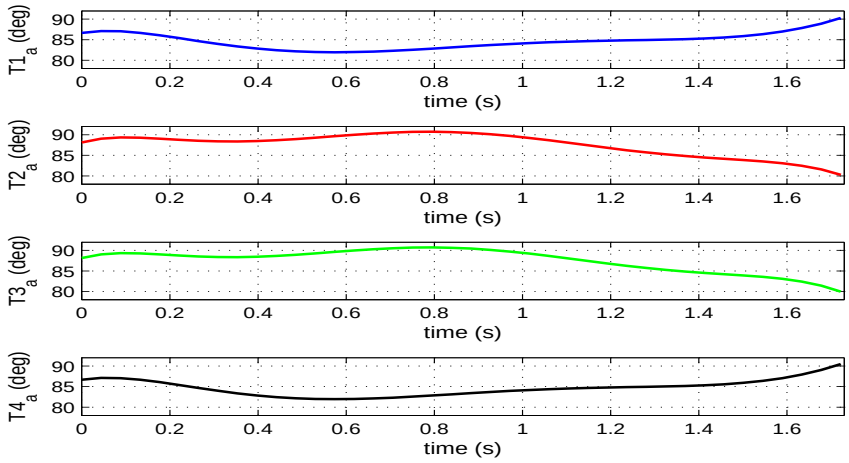

(b) Angles of thrust inputs

Figure 3–19: Time history of control signals for $x_f = 10$ m OSFM, case A3A7

From this table, the shortest optimal straight forward maneuver time is 1.72 s, attained with 18 actuator location combinations and most other combinations produce only slightly larger times. The longest and significantly different optimal straight forward maneuver time is 3.03 s for the actuator location case A3aA6. The

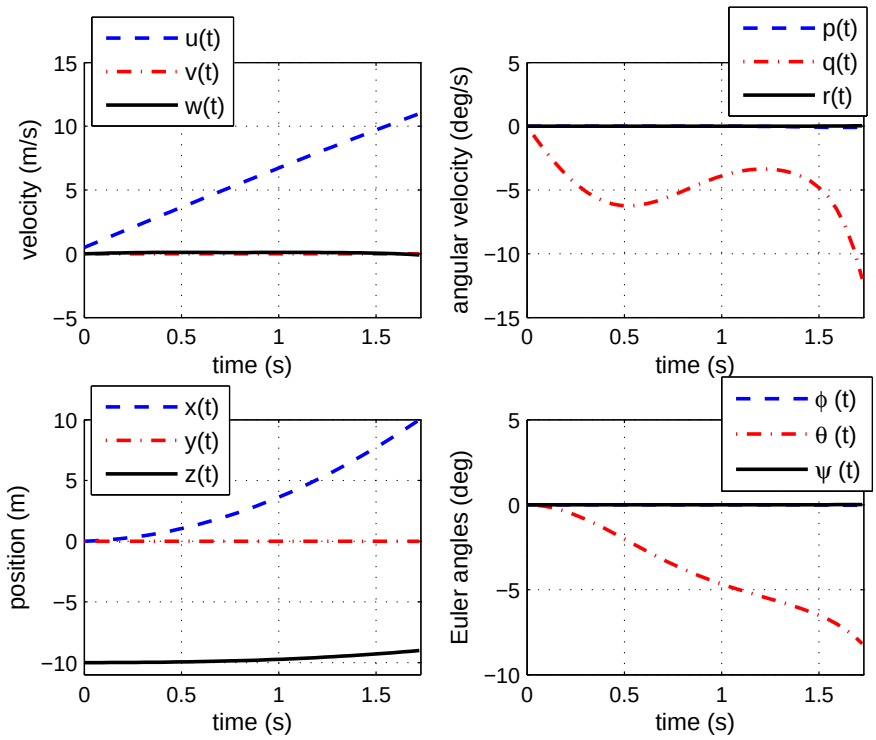

Figure 3–20: Time history of states for $x_f = 10$ m OSFM, case A3A7

straight forward maneuver does produce the desired displacement in the longitudinal direction. However, due to the coupling between longitudinal and lateral dynamics, there are non zero motions in the lateral directions in these simulations. Comparing the state responses from these simulations, it was found that the roll angular rate $p(t)$ is quite different between these simulations. The longitudinal velocity and roll angular rate for cases A3aA6, A4A6, A2A7 and A2A8 are plotted in Fig. 3–21. From this figure, we can see that the roll rate for case A2A8 never reaches its limits as

defined in Table. 3–5. However, $p(t)$ for case A3aA6 is at the ± 5 deg/s limit during most of the maneuver. In Chapter 4, further analysis on the effect of actuator locations on straight forward maneuver will be provided.

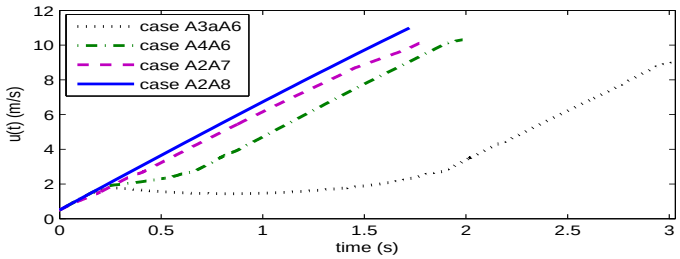

(a) Straight forward velocity $u(t)$ response

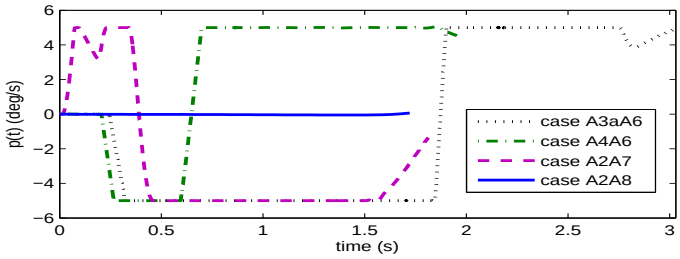

(b) Roll angular rate $p(t)$ response

Figure 3–21: Time history of states of $x_f = 10$ m OSFM

Similarly to the previous PID control simulations, the actuator placement does not have a significant effect on the speed of the open-loop SFM. There are three plausible reasons for this. First, because the available maximum forward thrust is not affected by actuator placements for ALTAV. The four actuators in the horizontal plane of the body frame can provide 44 N available maximum forward force, and the corresponding maximum forward acceleration is 6.93 m/s^2. With 0.5 m/s initial velocity, and pure rectilinear, it would take ALTAV 1.63 s to finish the SFM; but existence of lateral and vertical motions prolong ALTAV's maneuver time. From

Fig. 3–21, the absolute values of roll angular rate for cases A2A7, A4A6 and A3aA6 are larger than these for case A2A8 during most of the maneuver, and the t_f for these cases are also longer than that for case A2A8. However, the difference in lateral and vertical motions of different actuator location combinations are not significant for ALTAV. Therefore, the difference of t_f of different cases is not very significant. The second reason of the similarity of t_f in Table. 3–6 is the short 10 m maneuver distance. For a more realistic travel distance, the absolute difference in terminal maneuver time will be more significant for different actuator locations. Finally, we note that in order to clearly demonstrate the effect of actuator placement on ALTAV's maneuverability, the wind is not modeled in these simulations. If the wind velocity and acceleration are non zero, the differences in t_f for simulations with different actuator placements are expected to be more significant from the results in Table 3–6.

3.3.4 Optimal Control Strategy: $\psi_f = 180°$ Turning Maneuver

GPOPS software is also used to solve the optimal turning maneuver (OTM). Considered GPOPS computational complexity and simulation time, the final yaw angle ψ_f is set to 180° in this OTM. The cost function and the dynamics constraints are the same as those used for OSPF in Section 3.3.3. The boundary conditions for this optimal turning maneuver are listed in Table 3–7.

An example of the trajectory for the optimal turning maneuver based on the optimal control strategy is shown in Fig. 3–22. Compared to the turning trajectory for the $\psi_f = 360°$ PID turning maneuver shown in Fig. 3–11, the maneuver obtained with the optimal control strategy is "tighter", i.e. takes up less space in 3D. The corresponding control signals and the state responses are displayed in Fig. 3–23 and

Table 3–7: Boundary Conditions for t_f of $\psi_f = 180°$ Optimal Turning Maneuver ($\mathbf{v}_w = \mathbf{0}$ m/s, $\dot{\mathbf{v}}_w = \mathbf{0}$ m/s)

	Boundary Condition		Path Constraints on $\mathbf{x}(t)$	
	$\mathbf{x}(t_0)$	$\mathbf{x}(t_f)$	min	max
u (m/s)	0.5	free	0	2
v (m/s)	0	free	-2	2
w (m/s)	0	free	-0.1	0.1
p (deg/s)	0	free	-5	5
q (deg/s)	0	free	-16	16
r (deg/s)	0	free	0	free
x (m)	0	free	-0.001	3
y (m)	0	free	-0.001	3
z (m)	-10	free	-11	-9
ϕ (deg)	0	free	-10	10
θ (deg)	0	free	-30	20
ψ (deg)	0	$180°$	-1	180

Fig. 3–24 respectively. From Fig. 3–23, we can see that during the OTM, the four actuators achieve maximum thrust (11N) based on optimal control, which provides larger yaw angular rate $r(t)$ than the PID control in Section 3.3.1. However, the optimal control generated by GPOPS also has some disadvantages. We observe that there are several small cusps in Fig. 3–23, which exceed the $[-11, 11]$ N and $[-90°, 90°]$ control constraints.

In Fig. 3–24, the yaw angular rate $r(t)$ increases almost linearly and $\psi(t)$ increases parabolically during most part of the maneuver. However, in PID turning maneuver in Section 3.3.1, the $r(t)$ oscillates around 9° and $\psi(t)$ increases linearly, which shows that $r(t)$ and $\psi(t)$ increase slower under PID control and therefore PID control strategy is less efficient in the turning maneuver control. Other states remain within the limits in Table 3–7. The control signals and the state responses of this

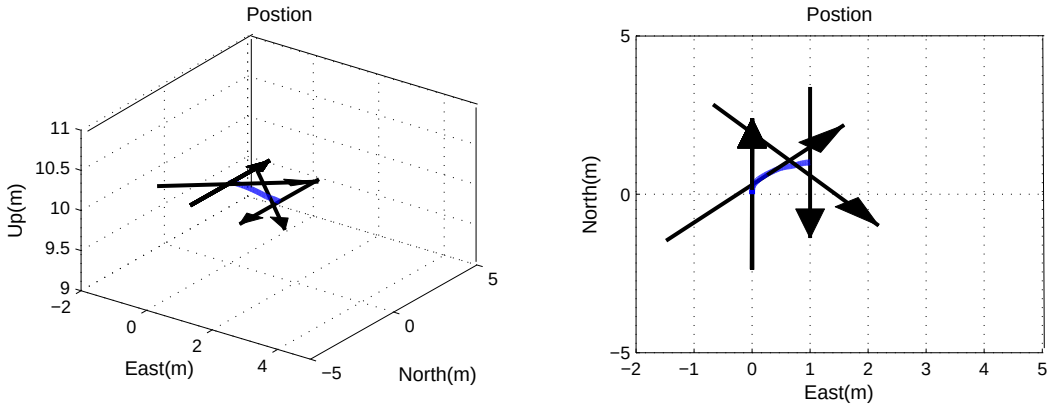

(a) In 3D Space (b) In $X-Y$ plane

Figure 3–22: The maneuver path of $\psi_f = 180°$ OTM, case A3A7

OTM are less oscillatory than those of the previous PID turning maneuver, and the maneuver time is much shorter since the yaw angular rate increases for the whole OTM procedure. In Chapter 4, we will further explain how these less oscillatory control signals are particularly better for ALTAV maneuver.

As was the case with previous control strategies, not all of the 64 actuator combinations allow ALTAV complete the 180° turning maneuver under optimal control strategy. The completion times for the successful 36 actuator locations are recorded in Table 3–8. The shortest maneuver time is 1.31 s for the actuator location case A4aA5a, and the longest maneuver time is 2.14 s, obtained for the actuator location case A1A9. The terminal turning time tends to increase with the distance between the forward and backward pairs of actuators.

The coupling effects between longitudinal and lateral motions are more significant than those in the straight forward maneuver due to lateral turning motion, resulting in more obvious time differences for the 180° turning maneuver than for

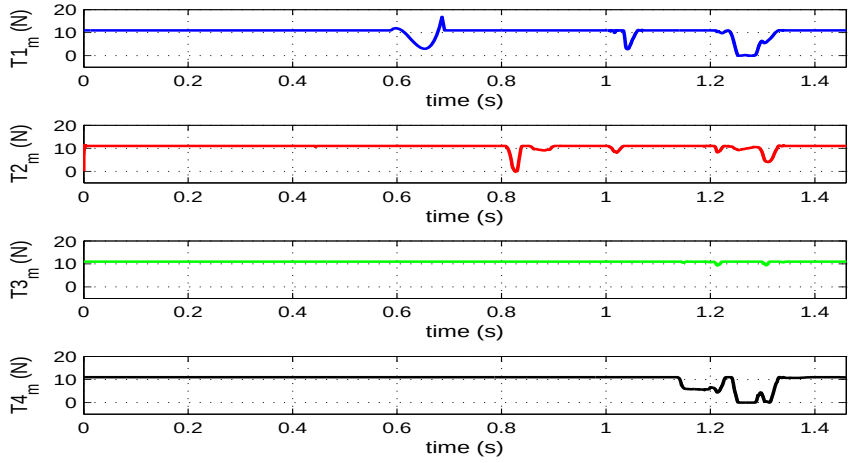

(a) Magnitude of thrust inputs

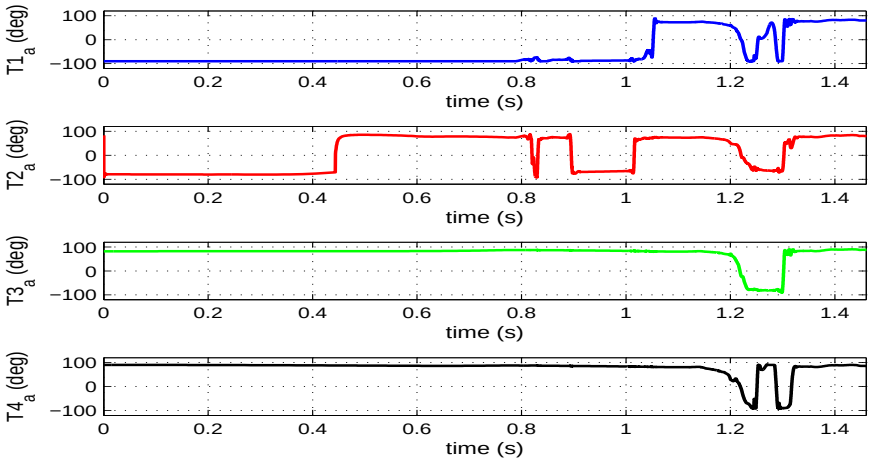

(b) Angles of thrust inputs

Figure 3–23: Time history of control signals of $\psi_f = 180°$ OTM, case A3A7

the straight forward maneuver with the same optimal control strategy. The responses of the velocity $u(t)$ and the yaw angular rate $r(t)$ for the 180° turning maneuver of cases A1A9, A1aA8, A2aA7a and A4aA5a are plotted in Figure. 3–25.

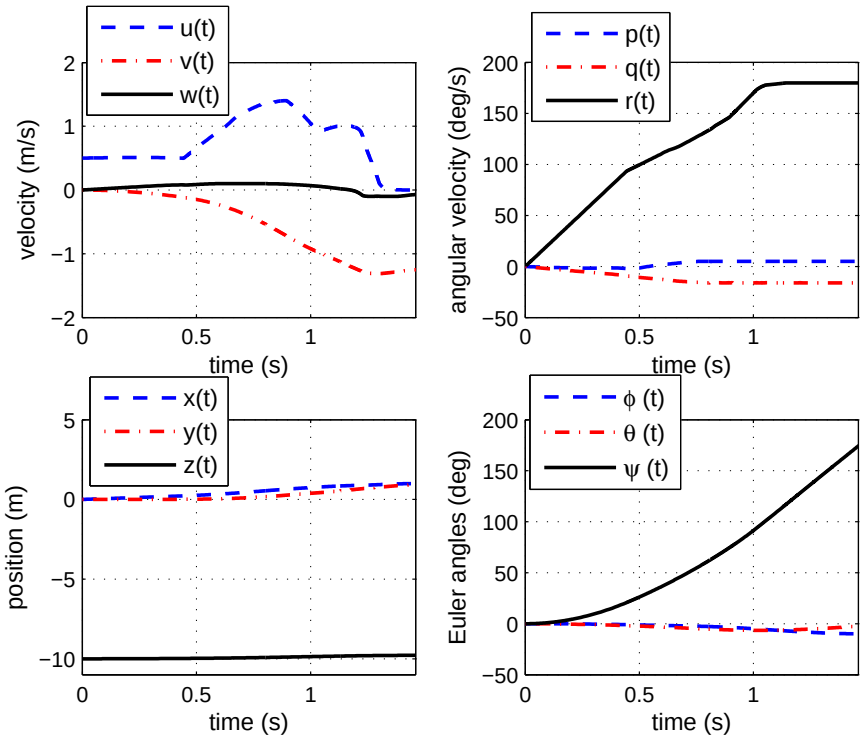

Figure 3–24: Time history of states of $\psi_f = 180°$ OTM, case A3A7

Table 3–8: t_f (s) of $\psi_f = 180°$ Optimal Turning Maneuver ($\mathbf{v}_w = \mathbf{0}$ m/s, $\dot{\mathbf{v}}_w = \mathbf{0}$ m/s)

Case	A1	A1a	A2	A2a	A3	A3a	A4	A4a
A5a							1.34	1.31
A6					1.52	1.36	1.33	1.34
A6a			1.66	1.51	1.41	1.38	1.38	
A7	1.85	1.71	1.59	1.50	1.46	1.44		
A7a	1.85	1.71	1.61	1.56	1.52	1.50		
A8	1.89	1.78	1.69	1.63	1.58			
A8a	2.01	1.88	1.78	1.72				
A9	2.14	1.99	1.89	1.81				

In these two figures, we observe that the shapes of the $u(t)$ curves are very similar for the four cases, and so is the case for $r(t)$ curves. Besides, we can see that the

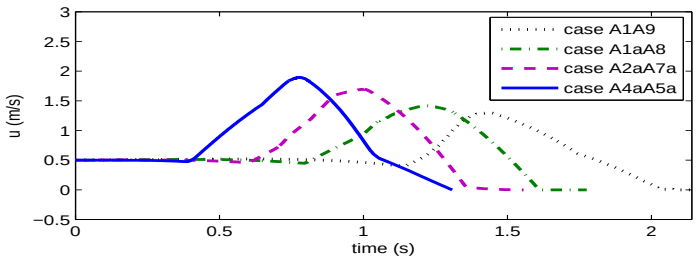

(a) Straight forward velocity $u(t)$ response

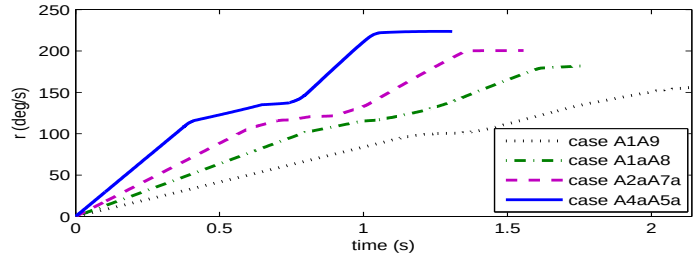

(b) Yaw angular rate $r(t)$ response

Figure 3–25: Time history of states of $\psi_f = 180°$ OTM

inflexion points of $u(t)$ curves occur at the same times as those of $r(t)$ curves. Looking at Figure. 3–25(a), we notice that all $u(t)$ responses are initially constant, then increase, decrease, and approach zero at the end of the optimal turning maneuver. Combined with Fig. 3–25(b), we observe that $u(t)$ tends to zero when $r(t)$ no longer increases. From these responses, it is obvious that the higher maneuverability can be achieved if ALTAV can increase and decrease its forward velocity efficiently.

Generally speaking, the terminal time differences are very significant between the two control strategies and actuator placements in each group of simulations. In most situations, the actuator locations that can be used to finish one type of maneuver can be also used to finish another form of maneuver. There are 28 actuator placements for which all four maneuvers can be completed. Moreover, the optimal

actuator locations based on PID control turning are quite similar to those under optimal control turning. Furthermore, in each kind of maneuver, the time differences between the best maneuverability and worst maneuverability is not very large. That said, the time differences for the zig-zag maneuver are larger than those for the other three maneuvers, which shows that that the more complex the maneuver is, the effect of actuator placement is more significant. However, the optimal actuator locations for the straight forward maneuver are slightly different from those for the turning maneuver, and those suitable for the zig-zag maneuver are located between the optimal sections for the straight forward turning maneuvers. In Chapter 4, we will theoretically analyze how to achieve better maneuverability by changing actuator locations, and try to find the optimal actuator locations suitable for both straight forward maneuver and turning maneuver.

CHAPTER 4
ALTAV Optimal Actuator Locations

Based on ALTAV maneuvering tests in Chapter 3, it is obvious that some actuator locations result in poor maneuverability of ALTAV and should be avoided. In this chapter, the influence of actuator locations on maneuverability will be explained. Then based on the understanding of effect of actuator locations on ALTAV maneuverability, a method used to find the optimal actuator locations is proposed.

In Section 4.1, the direct influence of actuator locations on ALTAV's dynamics model is obtained. Then, in Section 4.2, the influence of actuator locations on entries of ALTAV inverse mass matrix is discussed, and the method used to nullify some of off diagonal entries are proposed. In Section 4.3, the effect of actuator locations on straight forward maneuver and turning maneuver is explained through both the maximum available control forces and moments, and also through the maximum available accelerations and angular accelerations. After that, in Section 4.4, the optimal actuator location cost function is proposed, and the optimal actuator location for equal maneuverability in longitudinal direction and lateral direction is provided.

4.1 Model Analysis

The ALTAV dynamics model is further analyzed in this chapter, in particular the terms which are the actuator locations dependent on. Denoting the summations of all forces and moments on the right hand side of Eq. (3.2) as $\bar{\mathbf{f}}$ and $\bar{\mathbf{n}}$ respectively,

Eq. (3.2) is simplified to:

$$\begin{bmatrix} \dot{\boldsymbol{v}} \\ \dot{\boldsymbol{\omega}} \end{bmatrix} = \underbrace{\begin{bmatrix} \mathbf{M}_a & -m\mathbf{r}_{CG}^{\times} \\ m\mathbf{r}_{CG}^{\times} & \mathbf{J}_a \end{bmatrix}^{-1}}_{\bar{\mathbf{M}}_a^{-1}} \begin{bmatrix} \bar{\mathbf{f}} \\ \bar{\mathbf{n}} \end{bmatrix} = \underbrace{\begin{bmatrix} m\mathbf{I} + \mathbf{A}_m & -m\mathbf{r}_{CG}^{\times} \\ m\mathbf{r}_{CG}^{\times} & \mathbf{J} + \mathbf{A}_J \end{bmatrix}^{-1}}_{\bar{\mathbf{M}}_a^{-1}} \begin{bmatrix} \bar{\mathbf{f}} \\ \bar{\mathbf{n}} \end{bmatrix} \tag{4.1}$$

in which $\mathbf{r}_{CG}$ is equal to $[x_{CG}, 0, z_{CG}]^T$, $\mathbf{J}$ is the inertia tensor, and $\mathbf{A}_m$ and $\mathbf{A}_J$ are the added mass and added inertia tensors respectively. When ALTAV's actuator locations $\mathbf{q} = (x_{act1}, y_{act1}, x_{act2}, y_{act2})$ change, the $\bar{\mathbf{M}}_a^{-1}$, $\bar{\mathbf{f}}$ and $\bar{\mathbf{n}}$ will change, as does ALTAV's maneuverability. In order to better understand how changing actuator locations affect ALTAV's maneuverability, we will classify and analyze the components of $\bar{\mathbf{M}}_a$ into two groups: those that are constant and those dependent on actuator locations.

We observe that the apparent mass $\mathbf{M}_a$ only depends on the mass of the physical structure, the mass of lifting gas and the added mass. By the same token, since the added mass matrix $\mathbf{A}_J$ due to the air displaced by the airship is only a function of the mass of the displaced air and the geometry of the gas envelope, the added mass matrix $\mathbf{A}_J$ is also not affected by the actuator locations. Therefore, the following mass and inertial terms are constant in Eqs. (3.2, 4.1): $\mathbf{M}_a$, $\mathbf{M}_{Da}$ and $\mathbf{A}_J$, where $\mathbf{M}_a = m\mathbf{I} + \mathbf{A}_m$, $\mathbf{M}_{Da} = m_D\mathbf{I} + \mathbf{A}_m$ and m_D is the mass of air displaced by the airship.

When the ALTAV actuator locations $(x_{act1}, y_{act1}, x_{act2}, y_{act2})$ change, the vector $\mathbf{r}_{CG}$ of the center of gravity and the inertia tensor $\mathbf{J}_a$ change as a result: $(x_{CG}) \rightarrow \mathbf{r}_{CG}$, $(\mathbf{J}) \rightarrow \mathbf{J}_a$. The changes of these terms not only directly affect the mass matrix $\bar{\mathbf{M}}_a$,

but also the force $\bar{\mathbf{f}}$ and moment $\bar{\mathbf{n}}$ on the right hand side of Eq. (4.1), thus further affecting ALTAV's maneuverability.

4.2 Inverse Mass Matrix $\bar{\mathbf{M}}_a^{-1}$ Analysis

The inverse matrix of $\bar{\mathbf{M}}_a^{-1}$, most importantly the six diagonal entries m_{ii} of $\bar{\mathbf{M}}_a^{-1}$, can be considered to amplify $\bar{\mathbf{f}}$ and $\bar{\mathbf{n}}$ on the right hand side of Eq. (4.1). For example, for the given $\bar{\mathbf{f}}$ and $\bar{\mathbf{n}}$, if the corresponding diagonal entries in $\bar{\mathbf{M}}_a^{-1}$ increase due to changes in actuator locations, the corresponding accelerations and angular accelerations on the left hand side of Eq. (4.1) increase as a result. Then, the maneuverability in the corresponding directions increase. However, the increase in off-diagonal entries in $\bar{\mathbf{M}}_a^{-1}$ due to actuator locations can result in stronger coupling effects in ALTAV maneuvering, which decreases the maneuverability in most situations. For example, for the same $(n_z)_{\bar{\mathbf{n}}}$ (the component of $\bar{\mathbf{n}}$ in z-direction in body-fixed frame), if m_{66} of $\bar{\mathbf{M}}_a^{-1}$ increases as a result of a change in actuator locations, than the corresponding yaw angular acceleration $\dot{r}(t)$ increases, and so does turning maneuverability. However, if m_{26} and m_{46} increase due to changing actuator locations, than for the same $(n_z)_{\bar{\mathbf{n}}}$, the sway acceleration $\dot{v}(t)$ and the roll angular acceleration $\dot{p}(t)$ increase because of the coupling effect. If the aim of ALTAV is to achieve immediate turning, then the additional maneuvering in sway and roll directions can increase the turning time since more control force and moments need to be used to counter balance maneuvering in these two directions.

In this section, we explore the effects of actuator locations on the entries m_{ij} of the inverse mass matrix $\bar{\mathbf{M}}_a^{-1}$ in Eq. (4.1), and based on these we optimize the inverse mass matrix $\bar{\mathbf{M}}_a^{-1}$ through changing actuator locations to reduce some of the

coupling off diagonal entries of $\bar{\mathbf{M}}_a^{-1}$ to zero. In order to better understand the effect of actuator locations on $\bar{\mathbf{M}}_a^{-1}$, we develop the entries of $\bar{\mathbf{M}}_a^{-1}$ in symbolic form. Since $\bar{\mathbf{M}}_a$ is a symmetric matrix, $\bar{\mathbf{M}}_a^{-1}$ of a finless airship can be expressed as:

$$\begin{bmatrix} \mathbf{M}_a & -m\mathbf{r}_{CG}^{\times} \\ m\mathbf{r}_{CG}^{\times} & \mathbf{J}_a \end{bmatrix}^{-1} = \begin{bmatrix} m_{11} & & m_{13} & & m_{15} & \\ & m_{22} & & m_{24} & & m_{26} \\ m_{13} & & m_{33} & & m_{35} & \\ & m_{24} & & m_{44} & & m_{46} \\ m_{15} & & m_{35} & & m_{55} & \\ & m_{26} & & m_{46} & & m_{66} \end{bmatrix} \tag{4.2}$$

where $\mathbf{M}_a = diag([m_{a11}, m_{a22}, m_{a22}])$, $-m\mathbf{r}_{CG}^{\times} = [-b_{23}, 0, -b_{12}]^{\times}$ and $\mathbf{J}_a = diag([j_{a11}, j_{a22}, j_{a33}])$. In addition, for ALTAV, $m_{a11} = 6.9852$, $m_{a22} = 11.0376$, $b_{12} = mz_{CG} = 0.7393$, $b_{23} = mx_{CG} = 0.1135 + 1.4x_{act1} + 1.4x_{act2}$, and

$$\begin{aligned} j_{a11} &= j_{ap11} + J_y = 0.3265 + 1.4(y_{act1}^2 + y_{act2}^2), \\ j_{a22} &= j_{ap22} + J_x = 7.6293 + 1.4(x_{act1}^2 + x_{act2}^2), \\ j_{a33} &= j_{ap33} + (J_y + J_x) = 5.9558 + 1.4(x_{act1}^2 + x_{act2}^2 + y_{act1}^2 + y_{act2}^2). \end{aligned}$$

j_{apii} is the inertial tensor of the added mass and the physical structure except for actuator parts. Therefore, the entries of $\bar{\mathbf{M}}_a^{-1}$ can be expressed as functions of (m_{aii}, b_{ij}, j_{aii}), which further equals to function of (x_{acti}, y_{acti}). From Fig. 3–9, the (x_{acti}, y_{acti}) is along a strip with a certain distance to the equator of ALTAV, and the corresponding y_{acti} can be derived by the polynomial of the strip once x_{acti} is determined.

4.2.1 $\bar{\mathbf{M}}_a^{-1}$ With Non-Zero x_{CG}

As mentioned before, m_{ii} in $\bar{\mathbf{M}}_a^{-1}$ can be considered to amplify the forces and moments, and $m_{ij,i\neq j}$ is the coupling effect between different acceleration directions on the right hand side of Eq. (4.1). Let us denote the components of $\bar{\mathbf{f}}$ as $(f_x)_{\bar{\mathbf{f}}}$, $(f_y)_{\bar{\mathbf{f}}}$ and $(f_z)_{\bar{\mathbf{f}}}$; and the components of $\bar{\mathbf{n}}$ as $(n_x)_{\bar{\mathbf{f}}}$, $(n_y)_{\bar{\mathbf{f}}}$ and $(n_z)_{\bar{\mathbf{f}}}$. Therefore, in the longitudinal direction, the diagonal entries m_{11}, m_{33} and m_{55} are the amplifiers from $(f_x)_{\bar{\mathbf{f}}}$ to $\dot{u}$, from $(f_z)_{\bar{\mathbf{f}}}$ to $\dot{w}$ and from $(n_y)_{\bar{\mathbf{n}}}$ to $\dot{q}$ respectively, and the off diagonal entries m_{13}, m_{15} and m_{35} are the coupling effects from $(f_z)_{\bar{\mathbf{f}}}||(f_x)_{\bar{\mathbf{f}}}$ to $\dot{u}||\dot{w}$, from $(n_y)_{\bar{\mathbf{f}}}||(f_x)_{\bar{\mathbf{f}}}$ to $\dot{u}||\dot{q}$ and from $(n_y)_{\bar{\mathbf{f}}}||(f_z)_{\bar{\mathbf{f}}}$ to $\dot{w}||\dot{q}$ respectively. The m_{ii} are the principle longitudinal maneuvering entries in $\bar{\mathbf{M}}_a^{-1}$; the m_{13} is the coupling between the surge and the heave; the m_{15} and m_{35} are the couplings between translation and rotation. The longitudinal diagonal entries m_{ii} are expressed in in terms of m_{aii}, b_{ij} and j_{aii} as:

$$(f_x)_{\bar{\mathbf{f}}} \rightarrow \dot{u}: \quad m_{11} = \quad -\frac{-b_{23}^2 + j_{a22}m_{a22}}{m_{a22}b_{12}^2 + m_{a11}b_{23}^2 - j_{a22}m_{a11}m_{a22}} \tag{4.3}$$

$$(f_z)_{\bar{\mathbf{f}}} \rightarrow \dot{w}: \quad m_{33} = \quad -\frac{-b_{12}^2 + j_{a22}m_{a11}}{m_{a22}b_{12}^2 + m_{a11}b_{23}^2 - j_{a22}m_{a11}m_{a22}} \tag{4.4}$$

$$(n_y)_{\bar{\mathbf{n}}} \rightarrow \dot{q}: \quad m_{55} = \quad -\frac{m_{a11}m_{a22}}{m_{a22}b_{12}^2 + m_{a11}b_{23}^2 - j_{a22}m_{a11}m_{a22}} \tag{4.5}$$

and the off diagonal entries $m_{ij,i\neq j}$ are:

$$(f_z)_{\bar{\mathbf{f}}} \rightarrow \dot{u}||(f_x)_{\bar{\mathbf{f}}} \rightarrow \dot{w}: \quad m_{13} = \quad \frac{b_{12}b_{23}}{m_{a22}b_{12}^2 + m_{a11}b_{23}^2 - j_{a22}m_{a11}m_{a22}} \tag{4.6}$$

$$(n_y)_{\bar{\mathbf{n}}} \rightarrow \dot{u}||(f_x)_{\bar{\mathbf{f}}} \rightarrow \dot{q}: \quad m_{15} = \quad \frac{b_{12}m_{a22}}{m_{a22}b_{12}^2 + m_{a11}b_{23}^2 - j_{a22}m_{a11}m_{a22}} \tag{4.7}$$

$$(n_y)_{\bar{\mathbf{n}}} \to \dot{w}||(f_z)_{\bar{\mathbf{f}}} \to \dot{q}: \quad m_{35} = \quad -\frac{b_{23}m_{a11}}{m_{a22}b_{12}^2 + m_{a11}b_{23}^2 - j_{a22}m_{a11}m_{a22}} \tag{4.8}$$

In the lateral direction, the diagonal entries m_{22}, m_{44} and m_{66} are the amplifiers from $(f_y)_{\bar{\mathbf{f}}}$ to $\dot{v}$, from $(n_x)_{\bar{\mathbf{n}}}$ to $\dot{p}$ and from $(n_z)_{\bar{\mathbf{n}}}$ to $\dot{r}$ respectively, and the off diagonal entries m_{24}, m_{26} and m_{46} are the coupling effects from $(n_x)_{\bar{\mathbf{n}}}||(f_y)_{\bar{\mathbf{f}}}$ to $\dot{v}||\dot{p}$, from $(n_z)_{\bar{\mathbf{n}}}||(f_y)_{\bar{\mathbf{f}}}$ to $\dot{v}||\dot{r}$ and from $(n_z)_{\bar{\mathbf{n}}}||(n_x)_{\bar{\mathbf{n}}}$ to $\dot{p}||\dot{r}$ respectively. The m_{ii} are the principle lateral maneuvering entries in $\mathbf{M}_a^{-1}$; the m_{24} and m_{26} are the couplings between translation and rotation; the m_{46} is the coupling between the yaw and the roll. The lateral diagonal entries m_{ii} are expressed in terms of m_{aii}, b_{ij} and j_{aii} as:

$$(f_y)_{\bar{\mathbf{f}}} \to \dot{v}: \quad m_{22} = \quad -\frac{j_{a11}j_{a33}}{j_{a33}b_{12}^2 + j_{a11}b_{23}^2 - j_{a11}j_{a33}m_{a22}} \tag{4.9}$$

$$(n_x)_{\bar{\mathbf{n}}} \to \dot{p}: \quad m_{44} = \quad -\frac{-b_{23}^2 + j_{a33}m_{a22}}{j_{a33}b_{12}^2 + j_{a11}b_{23}^2 - j_{a11}j_{a33}m_{a22}} \tag{4.10}$$

$$(n_z)_{\bar{\mathbf{n}}} \to \dot{r}: \quad m_{66} = \quad -\frac{-b_{12}^2 + j_{a11}m_{a22}}{j_{a33}b_{12}^2 + j_{a11}b_{23}^2 - j_{a11}j_{a33}m_{a22}} \tag{4.11}$$

and the coupling mass entries $m_{ij,i\neq j}$ are:

$$(n_x)_{\bar{\mathbf{n}}} \to \dot{v}||(f_y)_{\bar{\mathbf{f}}} \to \dot{p}: \quad m_{24} = \quad -\frac{b_{12}j_{a33}}{j_{a33}b_{12}^2 + j_{a11}b_{23}^2 - j_{a11}j_{a33}m_{a22}} \tag{4.12}$$

$$(n_z)_{\bar{\mathbf{n}}} \to \dot{v}||(f_y)_{\bar{\mathbf{f}}} \to \dot{r}: \quad m_{26} = \quad \frac{b_{23}j_{a11}}{j_{a33}b_{12}^2 + j_{a11}b_{23}^2 - j_{a11}j_{a33}m_{a22}} \tag{4.13}$$

$$(n_z)_{\bar{\mathbf{n}}} \to \dot{p}||(n_x)_{\bar{\mathbf{n}}} \to \dot{r}: \quad m_{46} = \quad \frac{b_{12}b_{23}}{j_{a33}b_{12}^2 + j_{a11}b_{23}^2 - j_{a11}j_{a33}m_{a22}} \tag{4.14}$$

The numerical values of m_{ij} for the 64 actuator location combinations in Fig. 3–9 are calculate based on Eqs. (4.3-4.14), and the maximum and the minimum values, and the discrepancy between these two for each m_{ij} are listed in Table 4–1[1] .

Table 4–1: Discrepancies Of $\max m_{ij}$ And $\min m_{ij}$ At All Available Actuator Locations

m_{ij}	Multiplied by	$\max(m_{ij}) - \min(m_{ij})$
m_{11}	$F_x \to \dot{u}$	$\max(m_{11})_{4a,5a} - \min(m_{11})_{1,9} = 0.1446 - 0.1437 = 0.0009$
m_{33}	$F_z \to \dot{w}$	$\max(m_{33})_{1,5a} - \min(m_{33})_{*} = 0.0949 - 0.0906 = 0.0043$
m_{55}	$M_y \to \dot{q}$	$\max(m_{55})_{1,9} - \min(m_{55})_{4a,5a} = 0.1291 - 0.0498 = 0.0793$
m_{13}	$F_z \to \dot{u} \vert\vert F_x \to \dot{w}$	$\max(m_{13})_{4a,9} - \min(m_{13})_{1,5a} = 0.0018 - (-0.0019) = 0.0037$
m_{15}	$M_y \to \dot{u} \vert\vert F_x \to \dot{q}$	$\max(m_{15})_{1,9} - \min(m_{15})_{4a,5a} = -0.0053 - (-0.0137) = 0.0084$
m_{35}	$M_y \to \dot{w} \vert\vert F_z \to \dot{q}$	$\max(m_{35})_{1,5a} - \min(m_{35})_{4a,9} = 0.0182 - (-0.0172) = 0.0354$
m_{22}	$F_y \to \dot{v}$	$\max(m_{22})_{1,5a} - \min(m_{22})_{4a,5a} = 0.0967 - 0.0919 = 0.0048$
m_{44}	$M_x \to \dot{p}$	$\max(m_{44})_{1,9} - \min(m_{44})_{4a,5a} = 0.6819 - 0.2847 = 0.3972$
m_{66}	$M_z \to \dot{r}$	$\max(m_{66})_{4a,5a} - \min(m_{66})_{1,9} = 0.1065 - 0.0508 = 0.0553$
m_{24}	$M_x \to \dot{v} \vert\vert F_y \to \dot{p}$	$\max(m_{24})_{1,9} - \min(m_{24})_{4a,5a} = 0.0457 - 0.0191 = 0.0266$
m_{26}	$M_z \to \dot{v} \vert\vert F_y \to \dot{r}$	$\max(m_{26})_{1,5a} - \min(m_{26})_{4a,9} = 0.0167 - (-0.0178) = 0.0345$
m_{46}	$M_z \to \dot{p} \vert\vert M_x \to \dot{r}$	$\max(m_{46})_{4a,9} - \min(m_{46})_{1,5a} = 0.0048 - (-0.0053) = 0.0101$

Three entries in Table 4–1 need to be discussed here. From Table 4–1, we observe that the entry m_{44}, which relates to roll motion, has the largest maximum value, the largest minimum value, and the largest discrepancy value among the 12 entries. This implies that ALTAV is most sensitive in the roll direction maneuvering, and the actuator locations have an obvious effect on m_{44}. Compared to m_{44}, the entry m_{11}, which relates to straight forward maneuver, displays very different

[1] The subscript on $\max(m_{ij})$ and $\min(m_{ij})$ represents the actuator location combinations, and the additional subscript $*$ signifies that there are more than one actuator location combination fit for this situation.

characteristics. m_{11} has the second largest maximum value and the second largest minimum value. However, the discrepancy between the maximum and the minimum is the smallest among the 12 entries. This shows that ALTAV is highly maneuverable in the straight forward direction, and that changing actuator locations has little influence on maneuverability in this direction. Another very important entry is m_{66}, which relates to the turning maneuver. Compared with all the other diagonal entries, the maximum and the minimum value of m_{66} is not so large. However, the discrepancy between the maximum and the minimum ranks in the third position. This means that changing actuator locations can significantly increase or decrease ALTAV's turning maneuverability.

4.2.2 $\bar{\mathbf{M}}_a^{-1}$ With Zero x_{CG}

From Table 4–1, we observe that there are six non zero coupling entries in $\mathbf{M}_a^{-1}$ of ALTAV, m_{13}, m_{15}, m_{35}, m_{24}, m_{26} and m_{46}. In most situations, the coupling between different maneuvering directions can decrease the maneuvering efficiency and make the control of ALTAV more complicated. Therefore, it is desirable to reduce these coupling entries to zero through the available technology in design process. An example of $\mathbf{M}_a^{-1}$ matrix for Skyship-500 is:

$$\mathbf{M}_a^{-1} = \begin{bmatrix} 0.2071 & & & & -0.0075 & \\ & 0.8212 & & 0.1260 & & \\ & & 0.1683 & & & \\ & 0.1260 & & 0.0243 & & \\ -0.0075 & & & & 0.0014 & \\ & & & & & 0.0015 \end{bmatrix} \times 10^{-3} \qquad (4.15)$$

and we observe that the entries m_{13}, m_{35}, m_{26} and m_{46} are equal to zero in this inverse mass matrix. Further looking at Eqs. (4.6, 4.8, 4.13 and 4.14), we find that the numerators of these entries for ALTAV are multiplicative in $b_{23} = mx_{CG} = 0.1135 + 1.4x_{act1} + 1.4x_{act2}$ as mentioned before. This implies that we can make the m_{13}, m_{35}, m_{26} and m_{46} entries for ALTAV equal zero by adjusting actuator locations and making x_{CG} (b_{23}) equal to zero, thus decreasing the coupling between different maneuvering directions. When x_{CG} equals to zero, Eqs. (4.3-4.14) reduce to the following. In the longitudinal direction:

$$\begin{aligned}
(f_x)_{\bar{\mathbf{f}}} \rightarrow \dot{u}: \quad m_{11} &= -\frac{j_{a22}m_{a22}}{m_{a22}b_{12}^2 - j_{a22}m_{a11}m_{a22}} = \frac{j_{a22}}{-b_{12}^2 + j_{a22}m_{a11}} \\
(f_z)_{\bar{\mathbf{f}}} \rightarrow \dot{w}: \quad m_{33} &= \frac{-b_{12}^2 + j_{a22}m_{a11}}{(-b_{12}^2 + j_{a22}m_{a11})m_{a22}} = \frac{1}{m_{a22}} \\
(n_y)_{\bar{\mathbf{n}}} \rightarrow \dot{q}: \quad m_{55} &= -\frac{m_{a11}m_{a22}}{m_{a22}b_{12}^2 - j_{a22}m_{a11}m_{a22}} = \frac{m_{a11}}{-b_{12}^2 + j_{a22}m_{a11}}
\end{aligned} \tag{4.16}$$

and the off diagonal entries are:

$$\begin{aligned}
(f_z)_{\bar{\mathbf{f}}} \rightarrow \dot{u} || F_x \rightarrow \dot{w}: \quad m_{13} &= 0 \\
(n_y)_{\bar{\mathbf{n}}} \rightarrow \dot{u} || F_x \rightarrow \dot{q}: \quad m_{15} &= \frac{b_{12}m_{a22}}{m_{a22}b_{12}^2 - j_{a22}m_{a11}m_{a22}} = \frac{b_{12}}{b_{12}^2 - j_{a22}m_{a11}} \\
(n_y)_{\bar{\mathbf{n}}} \rightarrow \dot{w} || F_z \rightarrow \dot{q}: \quad m_{35} &= 0
\end{aligned} \tag{4.17}$$

In the lateral direction, the diagonal entries of $\bar{\mathbf{M}}_a^{-1}$ become:

$$\begin{aligned}
(f_y)_{\bar{\mathbf{f}}} \rightarrow \dot{v}: \quad m_{22} &= -\frac{j_{a11}j_{a33}}{j_{a33}b_{12}^2 - j_{a11}j_{a33}m_{a22}} = \frac{j_{a11}}{-b_{12}^2 + j_{a11}m_{a22}} \\
(n_x)_{\bar{\mathbf{n}}} \rightarrow \dot{p}: \quad m_{44} &= -\frac{j_{a33}m_{a22}}{j_{a33}b_{12}^2 - j_{a11}j_{a33}m_{a22}} = \frac{m_{a22}}{-b_{12}^2 + j_{a11}m_{a22}} \\
(n_z)_{\bar{\mathbf{n}}} \rightarrow \dot{r}: \quad m_{66} &= \frac{-b_{12}^2 + j_{a11}m_{a22}}{(-b_{12}^2 + j_{a11}m_{a22})j_{a33}} = \frac{1}{j_{a33}}
\end{aligned} \tag{4.18}$$

and the off diagonal entries are:

$$\begin{aligned}
(n_x)_{\bar{\mathbf{n}}} \rightarrow \dot{v}||F_y \rightarrow \dot{p}: \quad m_{24} &= -\frac{b_{12}j_{a33}}{j_{a33}b_{12}^2 - j_{a11}j_{a33}m_{a22}} = \frac{b_{12}}{-b_{12}^2 + j_{a11}m_{a22}} \\
(n_z)_{\bar{\mathbf{n}}} \rightarrow \dot{v}||F_y \rightarrow \dot{r}: \quad m_{26} &= 0 \\
(n_z)_{\bar{\mathbf{n}}} \rightarrow \dot{p}||M_x \rightarrow \dot{r}: \quad m_{46} &= 0
\end{aligned} \tag{4.19}$$

Recalculating m_{ij} of ALTAV when x_{CG} equals to zero, the resulting maximum and minimum values, and the discrepancy between them for each m_{ij} are included in Table 4–2[2] .

From Table 4–2, we observe that the entries m_{13}, m_{35}, m_{26} and m_{46} in $\mathbf{M}_a^{-1}$ of ALTAV have been reduced to zero as expected. On addition, m_{33} also reduces to zero when $x_{CG} = 0$, which means that changing actuator locations has no influence on m_{33} for $x_{CG} = 0$.

[2] The subscript on $\max(m_{ij})$ and $\min(m_{ij})$ represents the value x_{act1} of the x-coordinate of the actuator location combination, and the corresponding x_{act2} is generated according to $x_{CG} = 0$; and the y_{act1} and y_{act2} can be generated by the polynomial of the strip in Fig. 3–9.

Table 4–2: Discrepancies Of $\max m_{ij}$ And $\min m_{ij}$ At Actuator Locations with $x_{CG} = 0$

m_{ij}	Multiplied by	$\max(m_{ij}) - \min(m_{ij})$
m_{11}	$F_x \to \dot{u}$	$\max(m_{11})_{4a} - \min(m_{11})_1 = 0.1446 - 0.1437 = 0.0009$
m_{33}	$F_z \to \dot{w}$	$\max(m_{33})_* - \min(m_{33})_* = 0.0906 - 0.0906 = 0$
m_{55}	$M_y \to \dot{q}$	$\max(m_{55})_{4a} - \min(m_{55})_1 = 0.1282 - 0.0509 = 0.0773$
m_{13}	$F_z \to \dot{u} \| \| F_x \to \dot{w}$	$\max(m_{13}) - \min(m_{13}) = 0$
m_{15}	$M_y \to \dot{u} \| \| F_x \to \dot{q}$	$\max(m_{15})_{4a} - \min(m_{15})_1 = -0.0054 - (-0.0136) = 0.0082$
m_{35}	$M_y \to \dot{w} \| \| F_z \to \dot{q}$	$\max(m_{35}) - \min(m_{35}) = 0$
m_{22}	$F_y \to \dot{v}$	$\max(m_{22})_1 - \min(m_{22})_{4a} = 0.0935 - 0.0919 = 0.0017$
m_{44}	$M_x \to \dot{p}$	$\max(m_{44})_1 - \min(m_{44})_{4a} = 0.6572 - 0.2850 = 0.3722$
m_{66}	$M_z \to \dot{r}$	$\max(m_{66})_{4a} - \min(m_{66})_1 = 0.1060 - 0.0519 = 0.0541$
m_{24}	$M_x \to \dot{v} \| \| F_y \to \dot{p}$	$\max(m_{24})_1 - \min(m_{24})_{4a} = 0.0440 - 0.0191 = 0.0249$
m_{26}	$M_z \to \dot{v} \| \| F_y \to \dot{r}$	$\max(m_{26}) - \min(m_{26}) = 0$
m_{46}	$M_z \to \dot{p} \| \| M_x \to \dot{r}$	$\max(m_{46}) - \min(m_{46}) = 0$

Comparing Table 4–2 with Table 4–1, we observe that the maximum m_{11} (case A4aA5) and minimum m_{11} (case A1A9) and the discrepancy between them do not change, which implies that the highest maneuverability in straight forward maneuvering direction in Table 4–2 is the same as in Table 4–1, and changing actuator locations with $x_{CG} = 0$ does not decrease the possibility for ALTAV to achieve its highest maneuverability in straight forward flight. The discrepancy between the maximum and minimum m_{66} in Table 4–2 decreases slightly compared to that in Table 4–1. However, the influence on $\dot{r}$ is not obvious when x_{CG} turns to zero, unless the $|n_z|_{\bar{\mathbf{n}}}$ is larger than 1000 Nm (0.0553 of $\max(m_{66}) - \min(m_{66})$ in Table 4–1, 0.0541 of $\max(m_{66}) - \min(m_{66})$ in Table 4–2, and 0.0553-0.0541=0.0012), which is hard to be realized by ALTAV actuators. Therefore, x_{CG} does not affect turning maneuverability significantly.

4.3 Effects of ALTAV Actuator Locations on Straight Forward Maneuver and Turning Maneuver

In Section 3.3.3, we observed that both the maximum straight forward velocity $u(t)$ and the roll angular rate $p(t)$ affected the optimal straight forward maneuvering time, and both the maximum yaw angular rate $r(t)$ and the straight forward velocity $u(t)$ affected the optimal turning maneuvering time. In this section, we explain the effect of ALTAV actuator locations on straight forward maneuver through the analysis of the maximum available straight forward control force $\max(|f_x|_{\mathbf{f}_T})$ on the straight forward acceleration $\dot{u}(t)$, and the maximum available roll control moment $\max(|n_x|_{\mathbf{n}_T})$ on the roll angular acceleration $\dot{p}(t)$. We also explain the effect on turning maneuver through the analysis on the maximum available turning control moment $\max(|n_z|_{\mathbf{n}_T})$ on the maximum available turning angular acceleration $\dot{r}(t)$, and the maximum available straight forward control force $\max(|f_x|_{\mathbf{f}_T})$ on straight forward acceleration $\dot{u}(t)$.

Based on the results in Tables 3–3, 3–4, 3–6 and 3–8, different maneuver missions have different optimal actuator locations. Therefore, in order to understand the cause of these differences, the forms of actuator control force $\mathbf{f}_T$ and moment $\mathbf{n}_T$ are expanded in this section. Then, the effect on $(|f_x|_{\mathbf{f}_T}, |f_y|_{\mathbf{f}_T}, |f_z|_{\mathbf{f}_T})$ (the components of $\mathbf{f}_T$ in three directions in body-fixed coordinate) and $(|n_x|_{\mathbf{n}_T}, |n_y|_{\mathbf{n}_T}, |n_z|_{\mathbf{n}_T})$ (the components of $\mathbf{f}_T$ in three directions in body-fixed coordinate) due to changing actuator locations are analyzed. The actuators used for ALTAV are the vectorable thrusters. The control signals of each actuator include the thruster magnitude T_i and orientation θ_i, as illustrated in Fig. 4–1.

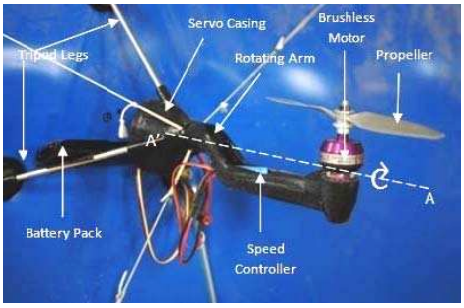

(a) Vectored thruster on ALTAV

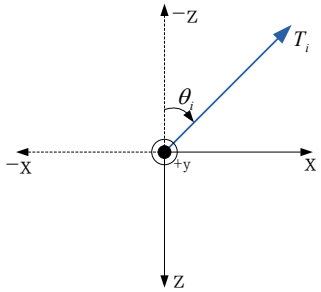

(b) Control signals for each actuator

Figure 4–1: Thruster structure and control signals of each actuator of ALTAV [54]

Based on the actuator location definition in Section 3.3, the control force and moment are derived as:

$$\mathbf{f}_T = \begin{bmatrix} T_1 s_{\theta_1} + T_2 s_{\theta_2} + T_3 s_{\theta_3} + T_4 s_{\theta_4} \\ 0 \\ -T_1 c_{\theta_1} - T_2 c_{\theta_2} - T_3 c_{\theta_3} - T_4 c_{\theta_4} \end{bmatrix} \tag{4.20}$$

$$\mathbf{n}_T = \begin{bmatrix} y_{act_2}(T_3 c_{\theta_3} - T_2 c_{\theta_2}) + y_{act_1}(T_4 c_{\theta_4} - T_1 c_{\theta_1}) \\ x_{act_1}(T_1 c_{\theta_1} + T_4 c_{\theta_4}) - x_{act_2}(T_2 c_{\theta_2} + T_3 c_{\theta_3}) \\ y_{act_2}(T_3 s_{\theta_3} - T_2 s_{\theta_2}) + y_{act_1}(T_4 s_{\theta_4} - T_1 s_{\theta_1}) \end{bmatrix} \tag{4.21}$$

in which $T_i \in [-11, 11]$ N and $\theta_i \in [-90, 90]$ deg.

4.3.1 Available Maximum Straight Forward Acceleration and Effect On Straight Forward Maneuver

In order to perform the straight forward maneuver as quickly as possible, the forward acceleration $\dot{u}$ should be maximum, which requires $T_1 = T_2 = T_3 = T_4 = 11$ N and $\theta_1 = \theta_2 = \theta_3 = \theta_4 = 90$ deg. Then, $s_{\theta_1} = s_{\theta_2} = s_{\theta_3} = s_{\theta_4} = 1$, $c_{\theta_1} = c_{\theta_2} =$

$c_{\theta_3} = c_{\theta_4} = 0$, and:

$$\mathbf{f}_T = \begin{bmatrix} 11 \times 4 \\ 0 \\ 0 \end{bmatrix} \text{ N}, \quad \mathbf{n}_\text{T} = \begin{bmatrix} 0 \\ 0 \\ 0 \end{bmatrix} \text{ Nm} \tag{4.22}$$

which shows that the maximum forward control force $\max(|f_x|_{\mathbf{f}_T})$ is a constant no matter what x_{act_i} and y_{act_i} are. Therefore, changing actuator locations does not affect the feasible maximum forward control force $\max(|f_x|_{\mathbf{f}_T})$. From Fig. 3–19 in Chapter 3, we observe that the maximum magnitude thrust of each actuator is 11 N, and these values are maintained for most of the maneuver. As well, the maximum angle of each actuators is 90°. We consider here, in Fig. 4–2 the actuator thrusters and angles of case A3aA6, the one with the longest optimal straight forward maneuver time.

From Fig. 4–2, we observe that the maximum thrust of 11 N and 90° thruster angles are achieved for this test case as well, which means even case A3aA6, the one with longest maneuver time, can achieve the maximum straight forward control force $\max(|f_x|_{\mathbf{f}_T})$ during the maneuver, which further proves that actuator locations do not affect the feasible maximum forward control force $\max(|f_x|_{\mathbf{f}_T})$. Since the first diagonal entry m_{11} of the inverse mass matrix $\mathbf{M}_a^{-1}$ is different for these 64 actuator location combinations, the maximum available straight forward accelerations $\max(\dot{u}(t))$ due to the available maximum forward control force $\max(|f_x|_{\mathbf{f}_T})$ will be slightly different from one another in these 64 cases. We calculate the available maximum straight forward control force $\max(|f_x|_{\mathbf{f}_T})$, the first diagonal entry m_{11} of the inverse mass matrix $\mathbf{M}_a^{-1}$, the available maximum straight forward acceleration $\dot{u}(t)$,

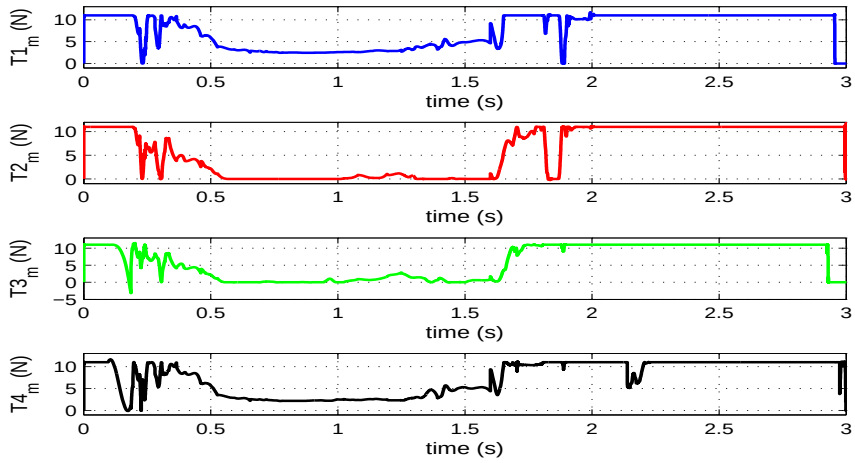

(a) Magnitude of thrust inputs

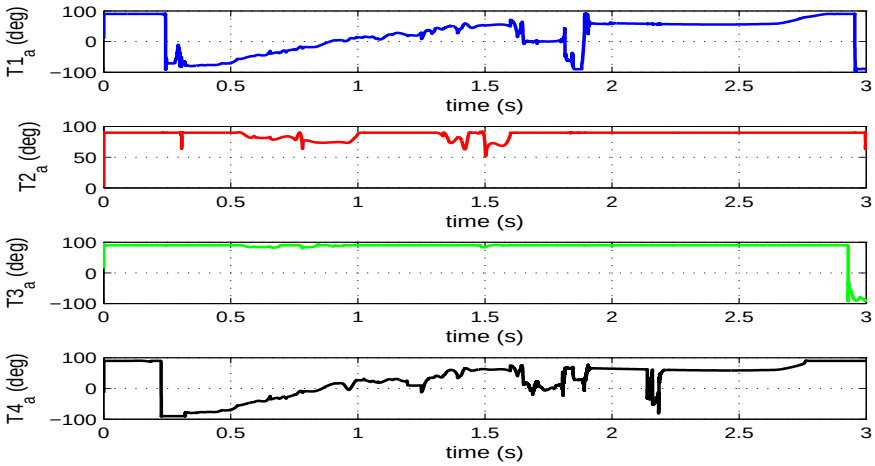

(b) Angles of thrust inputs

Figure 4–2: Time history of control signals of $x_f = 10$ m OSFM, case A3aA6

the straight forward maneuver time $(t_f)_{OSFM}$ for cases A3aA6, A2A7 and A2A8, and list them in Table 4–3. From Table 4–3, we can see that even case A3aA6 has the maximum available straight forward acceleration, it still finishes the OSFM in

the longest maneuver time. This means that there are still other factors existing and affecting the terminal time of the OSFM.

Table 4–3: The Comparison of Maximum Available Straight Forward Acceleration $\max(\dot{u}(t))$ and The Terminal Maneuver Time $(t_f)_{OSFM}$ of Optimal Straight Forward Maneuver, case A3aA6, A2A7 and A2A8

	case A3aA6	case A2A7	case A2A8
$\max(\lvert f_x\rvert_{\mathbf{f}_T})$ (N)	44	44	44
$(m_{11})_{\mathbf{M}_a^{-1}}$	0.1444	0.1441	0.1439
maximum available straight forward acceleration $\max(\dot{u}(t))$ (m/s^2)	6.3536	6.3404	6.3316
$(t_f)_{OSFM}$ (s)	3.03	1.81	1.72

From Fig. 3–21 in Chapter 3, we observed that the roll angular rates are quite different between cases A3aA6 and A2A8. We further calculate and list the maximum available roll control moments $\max(\lvert n_x\rvert_{\mathbf{n}_T})$, the fourth diagonal entry m_{44} of the inverse mass matrix $\mathbf{M}_a^{-1}$, the resulting maximum available roll angular acceleration $\dot{p}(t)$ and the straight forward maneuver time $(t_f)_{OSFM}$ for cases A3aA6, A2A7 and A2A8 in Table 4–4. From Table 4–4, we observe that the maximum available roll angular acceleration $\dot{p}(t)$ has a significant effect on the optimal straight forward terminal maneuver time. Changing actuator locations to obtain high roll controllability, $\max(\lvert n_x\rvert_{\mathbf{n}_T})$ and high roll angular acceleration $\dot{p}(t)$ is correlated with a shorter straight forward maneuver time.

4.3.2 Available Maximum Turning Angular Acceleration and The Effect On Turning Maneuver

On the other hand, in order to perform a clockwise turning maneuver as quickly as possible, the angular acceleration $\dot{r}(t)$ should be maximum, which requires $T_1 = T_2 = T_3 = T_4 = 11$ N, $\theta_1 = \theta_2 = -90$ deg, $\theta_3 = \theta_4 = 90$ deg ($\theta_1 = \theta_2 = 90$ deg,

Table 4–4: The Comparison of Maximum Available Roll Angular Acceleration $\dot{p}(t)$ and The Terminal Maneuver Time $(t_f)_{OSFM}$ of Optimal Straight Forward Maneuver, case A3aA6, A2A7 and A2A8

	case A3aA6	case A2A7	case A2A8
$\max(\lvert n_x\rvert_{\mathbf{n}_T})$ (Nm)	46.3210	40.7418	37.8224
$(m_{44})_{\mathbf{M}_a^{-1}}$	0.2966	0.3738	0.4270
maximum available roll angular acceleration $\dot{p}(t)$ (deg/s^2)	13.7388	15.2293	16.1502
$(t_f)_{OSFM}$ (s)	3.03	1.81	1.72

$\theta_3 = \theta_4 = -90$ deg for counterclockwise turning maneuver). Then, $s_{\theta_1} = s_{\theta_2} = -1$, $s_{\theta_3} = s_{\theta_4} = 1$, $c_{\theta_1} = c_{\theta_2} = c_{\theta_3} = c_{\theta_4} = 0$, and:

$$\mathbf{f}_T = \begin{bmatrix} 0 \\ 0 \\ 0 \end{bmatrix} \text{ N}, \quad \mathbf{n}_\text{T} = \begin{bmatrix} 0 \\ 0 \\ 22(y_{act_1} + y_{act_2}) \end{bmatrix} \text{ Nm} \tag{4.23}$$

which shows that for the clockwise turning maneuver, maximizing the $(y_{act_1} + y_{act_2})$ is important for ALTAV to achieve maximum turning moments $\max(\lvert n_z\rvert_{\mathbf{n}_T})$ and minimum turning time $(t_f)_{OTM}$. As per Fig. 3–9, the case A4aA5a location provides the maximum $(y_{act_1} + y_{act_2})$, and t_f in Table 3–8 supports this claim. In order to further prove that case A4aA5a can achieve the maximum yaw angular acceleration $\max(\dot{r}(t))$, the maximum available turning moment $\max(\lvert n_z\rvert_{\mathbf{n}_T})$, the sixth entry m_{66} of $\mathbf{M}_a^{-1}$, the maximum available yaw angular acceleration $\max(\dot{r}(t))$ and the optimal turning maneuver time $(t_f)_{OTM}$ for cases A1A9, A2aA7a and A4aA5a are calculated and listed in Table. 4–5.

Table 4–5: The Comparison of Maximum Available Yaw Angular Acceleration $\dot{r}(t)$ and The Terminal Maneuver Time $(t_f)_{OTM}$ of Optimal Turning Maneuver, case case A1A9, A2aA7a and A4aA5a

	case A1a9	case A2aA7a	case A4aA5a
$\max(\lvert n_z\rvert_{\mathbf{n}_T})$ (Nm)	28.7210	41.1950	47.3616
$(m_{66})_{\mathbf{M}_a^{-1}}$	0.0508	0.0752	0.1065
maximum available yaw angular acceleration $\dot{r}(t)$ (deg/s^2)	1.459	3.0979	5.0440
$(t_f)_{OSFM}$ (s)	2.14	1.56	1.31

From Table. 4–5, we can see that the actuator location combination case A4aA5a has the maximum available turning moment $\max(\lvert n_z\rvert_{\mathbf{n}_T})$, the maximum sixth entry m_{66} of $\mathbf{M}_a^{-1}$, the maximum available yaw angular acceleration $\max(\dot{r}(t))$ and the shortest optimal turning maneuver time $(t_f)_{OTM}$. In Section 3.3.4, we observe that the straight forward acceleration $\dot{u}(t)$ directly affects the turning maneuverability. In order to further analyze the effect of maximum available straight forward force $\max(\lvert f_x\rvert_{\mathbf{f}_T})$ on the terminal turning time, we calculate the available maximum straight forward control force $\max(\lvert f_x\rvert_{\mathbf{f}_T})$, the first diagonal entry m_{11} of the inverse mass matrix $\mathbf{M}_a^{-1}$, the available maximum straight forward acceleration $\dot{u}(t)$, the straight forward maneuver time $(t_f)_{OSFM}$ case A1A9, A2aA7a and A4aA5a, and list them in Table 4–6. The case A4aA5a has the highest straight forward maneuverability, and the higher straight forward acceleration that can help with shortening the optimal turning maneuver time.

4.4 Optimal Actuator Placement Cost Function

In Section 4.2, we analyzed the effect of actuator location on entries m_{ij} of the inverse mass matrix $\bar{\mathbf{M}}_a^{-1}$, and found out that by changing actuator locations to satisfy $x_{CG} = 0$, we can nullify eight, four off diagonal entries of $\bar{\mathbf{M}}_a^{-1}$. Therefore, the

Table 4–6: The Comparison of Maximum Available Straight Forward Acceleration $\max(\dot{u}(t))$ and The Terminal Maneuver Time $(t_f)_{OTM}$ of Optimal Turning Maneuver, case case A1A9, A2aA7a and A4aA5a

	case A1a9	case A2aA7a	case A4aA5a
$\max(\lvert f_x \rvert_{\mathbf{f}_T})$ (N)	44	44	44
$(m_{11})_{\mathbf{M}_a^{-1}}$	0.1437	0.1441	0.1446
maximum available straight forward acceleration $\max(\dot{u}(t))$ (m/s^2)	6.3228	6.3404	6.3624
$(t_f)_{OSFM}$ (s)	2.14	1.56	1.31

coupling effect between the different maneuver directions can be greatly decreased. In Section 4.3, we demonstrated how by changing actuator locations and choosing the proper m_{ij} of $\bar{\mathbf{M}}_a^{-1}$ can help ALTAV improve straight forward maneuverability and turning maneuverability. In this section, we focus on finding the optimal actuator locations through systematically adjusting the effects of actuator locations on m_{ij} of $\bar{\mathbf{M}}_a^{-1}$ under the condition $x_{CG} = 0$.

In order to achieve best maneuverability in both the straight forward and turning maneuvers, we need to maximize some of the entries m_{ij}, and minimize others. First, to achieve highest controllability in roll direction and shorten airship straight forward maneuver time, one can minimize m_{44} according to Table 4–4. Second, it is better to maximize m_{11} and m_{66} so as to maximize the turning maneuverability in yaw direction. On addition, the pitching maneuverability is also important for an airship, and therefore maximizing m_{55} is also required. Second, the absolute values of the coupling terms $|m_{15}|$ and $|m_{24}|$ should be minimized. In addition, in order to decrease the sensitivity in the sway direction, in which no control forces can be generated by ALTAV actuators,the m_{22} entry needs to be minimized. Therefore, all m_{ij} terms can be cataloged into three groups:

- m_{ij} to be maximized: m_{11}, m_{55}, and m_{66}.
- m_{ij} to be minimized: m_{15}, m_{22}, m_{44}, and m_{24}.
- m_{ij} to be set to zero: m_{33}, m_{13}, m_{35}, m_{26}, and m_{46}.

Based on above analysis, the cost function for optimal actuator locations can be formulated as:

$$J_{act} = \min_{\hat{x}_{CG}=0} F_{act}(x_{act1}, x_{act2}, y_{act1}, y_{act2}) \tag{4.24}$$

in which

$$F_{act} = \underbrace{k_1\frac{1}{m_{11}} + k_2\frac{1}{m_{55}} + k_3|m_{15}|}_{longitudinal} + \underbrace{k_4\frac{1}{m_{66}} + k_5 m_{22} + k_6 m_{44} + k_7|m_{24}|}_{lateral} \tag{4.25}$$

where k_i are the optimal coefficients in the required direction and $\sum_{i=1}^{7} k_i = 1$. Since y_{acti} depends on x_{acti} and the sum of x_{act1} and x_{act2} is a constant ($\hat{x}_{CG} = 0.113472 + 1.4(x_{act1} + x_{act2}) = b_{23} = 0$), x_{act2} and y_{acti} are functions of x_{act1}, and furthermore, $1/m_{ii}$ and m_{ij} can be considered as functions of x_{act1}. Technically speaking, the weights k_i are determined by the requirements of the mission. For instance,if the maneuver mission emphasizes turning maneuverability, k_4 should be set to a relatively large value. When actuator locations $(x_{act1}, y_{act1}, x_{act2}, y_{act2})$ change, the terms $1/m_{ii}$ and m_{ij} change in different scales and speeds. Although k_i are determined by the mission requirements, the changing scales and speeds of $1/m_{ii}$ and m_{ij} should be considered also. Therefore, the changes of $1/m_{ii}$ and m_{ij} with increase of x_{act1} are plotted in Fig. 4–3.

From Fig. 4–3, except for $|m_{15}|$, the terms $1/m_{ii}$ and m_{ij} obey a positive relationship with the increase of x_{act1}. Large $|m_{15}|$ value can increase the coupling

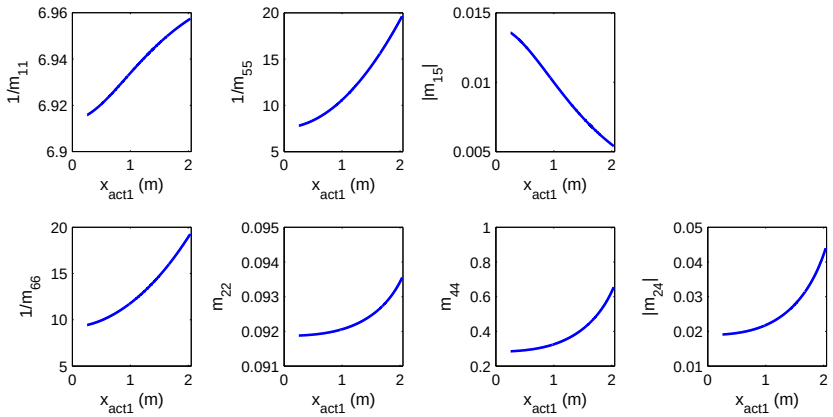

Figure 4–3: The changes of individual items in F_{act} with increase of x_{act1}

effect between straight forward direction and pitch direction, and decrease ALTAV straight maneuver and turning maneuver times. Therefore, the coefficient k_3 of $|m_{15}|$ should be carefully chosen. Because the scales of $1/m_{ii}$ and m_{ij} in Fig. 4–3 are very different. We rescale the terms in the function between one and two in Fig. 4–4 and Eq. (4.25) is reformulated to Eq. (4.26).

$$\begin{aligned}\tilde{F}_{act} =& k_1\left[\frac{1/m_{11}-\min(1/m_{11})}{\max(1/m_{11})-\min(1/m_{11})}+1\right]+k_2\left[\frac{1/m_{55}-\min(1/m_{55})}{\max(1/m_{55})-\min(1/m_{55})}+1\right]+\\ & k_3\left[\frac{|m_{15}|-\min(|m_{15}|)}{\max(|m_{15}|)-\min(|m_{15}|)}+1\right]+k_4\left[\frac{1/m_{66}-\min(1/m_{66})}{\max(1/m_{66})-\min(1/m_{66})}+1\right]+\\ & k_5\left[\frac{m_{22}-\min(m_{22})}{\max(m_{22})-\min(m_{22})}+1\right]+k_6\left[\frac{m_{44}-\min(m_{44})}{\max(m_{44})-\min(m_{44})}+1\right]+\\ & k_7\left[\frac{|m_{24}|-\min(|m_{24}|)}{\max(|m_{24}|)-\min(|m_{24}|)}+1\right]\end{aligned} \tag{4.26}$$

Considering an equal weighting for all terms in Eq. (4.26), i.e., $k_1 = k_2 = k_3 = k_4 = k_5 = k_6 = k_7 = 1/7$, the resulting value of $\tilde{F}_{act}$ is plotted in Fig. 4–5 and

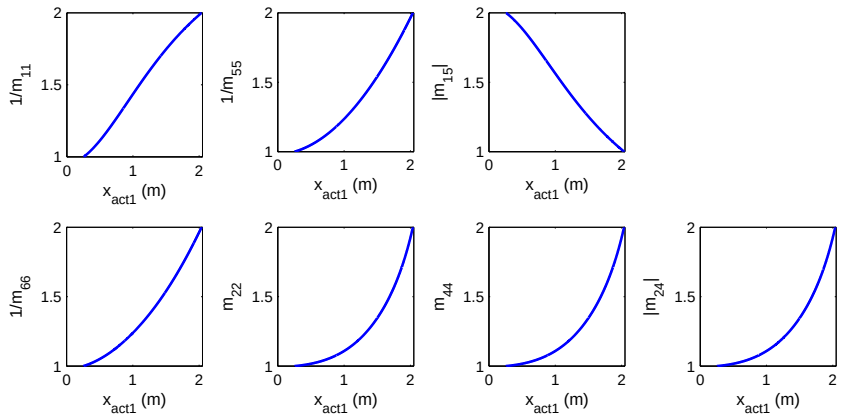

Figure 4–4: The changes of individual items in $\tilde{F}_{act}$ with increase of x_{act1}

the corresponding optimal actuator locations are shown in Fig. 4–6. This actuator placement is fit for the OTM but not for the OSFM.

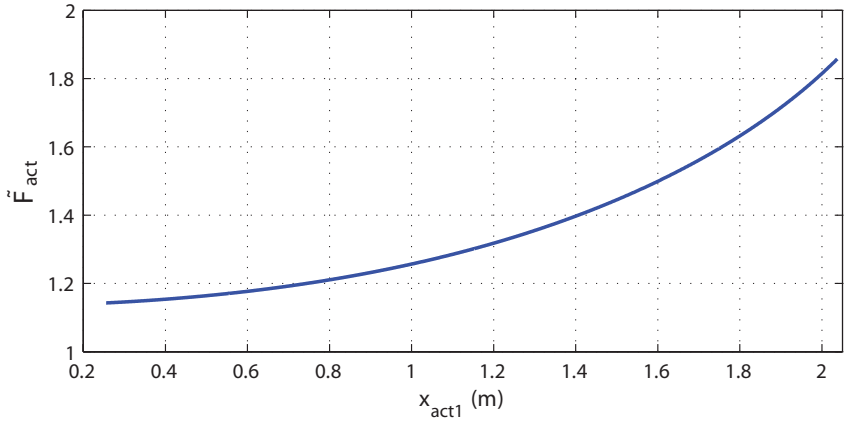

Figure 4–5: $\tilde{F}_{act}$ with $k_1 = k_2 = k_3 = k_4 = k_5 = k_6 = k_7 = 1/7$

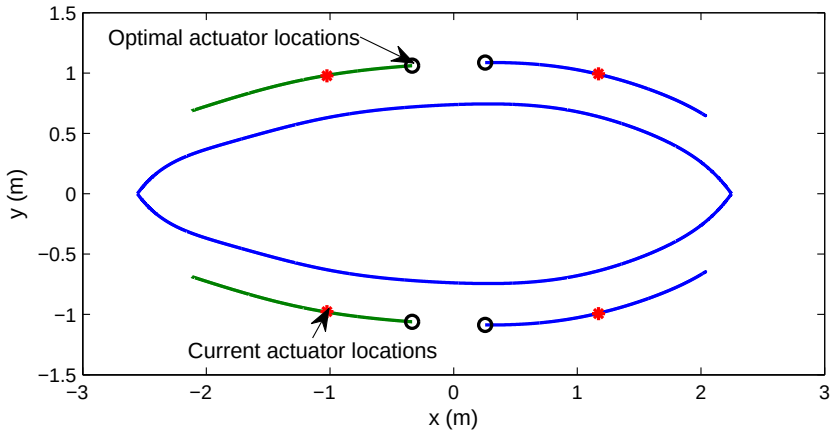

Figure 4–6: Optimal actuator locations of $\tilde{F}_{act}$ with $k_1 = k_2 = k_3 = k_4 = k_5 = k_6 = k_7 = 1/7$

In order to further analyze the roles of the terms in Eq. (4.26), they are grouped into those related to the longitudinal direction and those related to the lateral direction as in Eq. (4.27) and Eq. (4.28) respectively:

$$F_{Lon} = k_1 \left[\frac{1/m_{11} - \min(1/m_{11})}{\max(1/m_{11}) - \min(1/m_{11})} + 1 \right] + k_2 \left[\frac{1/m_{55} - \min(1/m_{55})}{\max(1/m_{55}) - \min(1/m_{55})} + 1 \right] + k_3 \left[\frac{|m_{15}| - \min(|m_{15}|)}{\max(|m_{15}|) - \min(|m_{15}|)} + 1 \right] \tag{4.27}$$

$$F_{Lat} = k_4 \left[\frac{1/m_{66} - \min(1/m_{66})}{\max(1/m_{66}) - \min(1/m_{66})} + 1 \right] + k_5 \left[\frac{m_{22} - \min(m_{22})}{\max(m_{22}) - \min(m_{22})} + 1 \right] + k_6 \left[\frac{m_{44} - \min(m_{44})}{\max(m_{44}) - \min(m_{44})} + 1 \right] + k_7 \left[\frac{|m_{24}| - \min(|m_{24}|)}{\max(|m_{24}|) - \min(|m_{24}|)} + 1 \right] \tag{4.28}$$

in which $\sum_{i=1}^{3} k_i = 1$ and $\sum_{i=4}^{7} k_i = 1$. Then, $\tilde{F}_{act}$ for optimizing actuator locations is reformulated as:

$$\bar{F}_{act} = K_1 \left[\frac{F_{OSFM} - \min(F_{OSFM})}{\max(F_{OSFM}) - \min(F_{OSFM})} + 1 \right] + K_2 \left[\frac{F_{OTM} - \min(F_{OTM})}{\max(F_{OTM}) - \min(F_{OTM})} + 1 \right] \tag{4.29}$$

and Eq. (4.24) becomes:

$$J_{act} = \min_{\hat{x}_{CG}=0} \bar{F}_{act}(x_{act1}, x_{act2}, y_{act1}, y_{act2}) \tag{4.30}$$

in which $\sum_{i=1}^{2} K_i = 1$. First, we study the influence of k_1 to k_3 on the optimal actuator cost function, and assume that the longitudinal maneuver is as important as the lateral maneuver for ALTAV, which yields $K_1 = K_2 = 0.5$. Figure. 4–7 shows the change in $\bar{F}_{act}$ as we vary k_1 to k_3, with k_2 equal to k_3, and k_1 changing from 1/3 to 0.0.

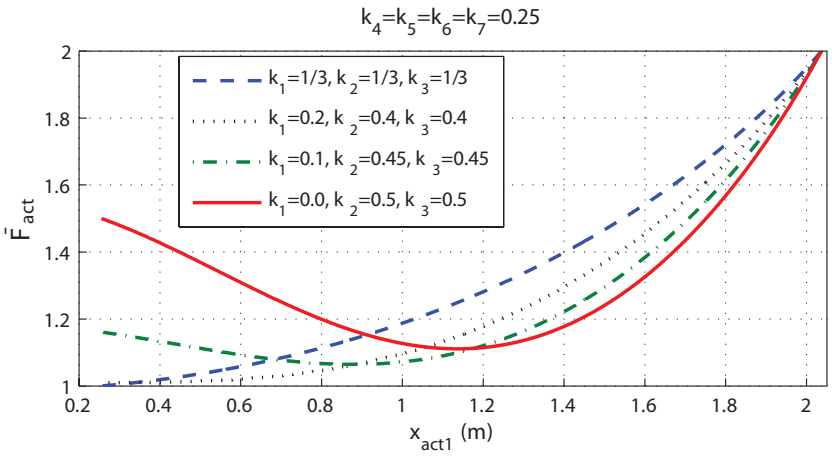

Figure 4–7: $\bar{F}_{act}$ ($k_4 = k_5 = k_6 = k_7 = 0.25$, $K_1 = K_2 = 0.5$)

From Fig. 4–7, we observe that the location x_{act1} in Eq. (4.30) increases with the decrease of k_1. Referring to Table 3–6, $k_1 = 0$ can better reflect the longitudinal characteristics, and the x_{act1} of J_{act} in Fig. 4–7 with $k_1 = 0$ is quite close to caseA2A8 in Table 3–6. Furthermore, for different actuator locations, the differences in the straight forward maneuverability due to the ability to resist motions in other directions, and the available maximum straight forward acceleration does not affect the straight forward maneuvering time.

The influence of k_4 to k_7 on the lateral direction is studied in Fig. 4–8, where k_1 to k_3 are set to 0.0, 0.5 and 0.5 based on the previous analysis. In the lateral direction, the term $1/m_{66}$ is considered to be the most important one. Therefore, the corresponding k_4 value is increased at here, and all the other three coefficients are set to the same values. From Fig. 4–8, the x_{act1} of J_{act} due to different k_4 to k_7 are almost the same. This variation is in agreement with the positive relationship of $1/m_{66}$, m_{22}, m_{44} and $|m_{24}|$ with increase of x_{act1} in Fig. 4–4.

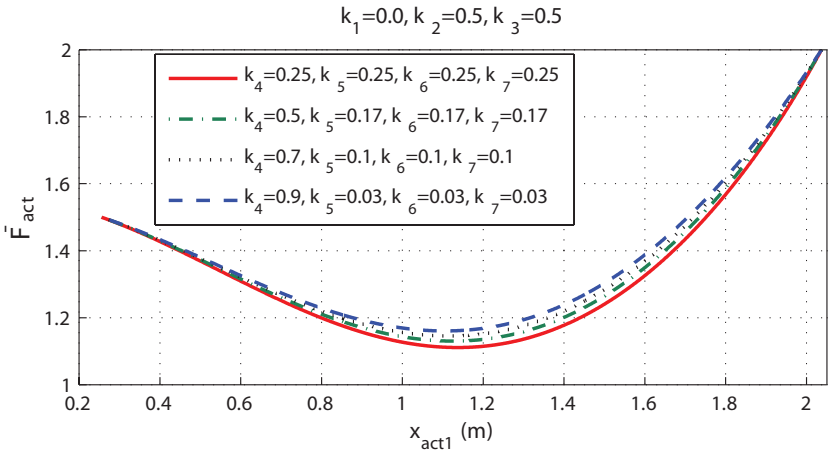

Figure 4–8: $\bar{F}_{act}$ ($k_1 = 0.0$, $k_2 = k_3 = 0.5$, $K_1 = K_2 = 0.5$)

In most real maneuver tasks, however, the percentages of the longitudinal maneuver and the lateral maneuvering are not the same. Additionally, as we observed from Tables 3–6 and 3–8, the optimal actuator locations for the longitudinal maneuvering are different from those for the lateral maneuvering. In order to achieve the highest maneuverability in the whole maneuver task, the optimal actuator locations should be selected between those for the longitudinal maneuver and those for the lateral maneuver. In this thesis, this issue is solved by adjusting K_1 and K_2 in Eq. (4.30). K_1 and K_2 are used to represent the percentages of the longitudinal maneuver and the lateral maneuver in the required maneuver task. In Fig. 4–9, we show the effect on the objective function as K_1 increases from 0% to 100%, and K_2 decreases from 100% to 0% with $k_1 = 0.0$, $k_2 = k_3 = 0.5$, and $k_4 = k_5 = k_6 = k_7 = 0.25$.

The optimal actuator locations due to different K_1 and K_2 in Fig. 4–9 are in good agreement with the simulation results in Table 3–6 and Table 3–8. From Fig. 4–9, we can see that with the increase of the percentage of longitudinal maneuver, the x_{act1} increases from 0.2553 m to 1.2723 m. The optimal actuator locations with equal K_1 and K_2 are plotted in Fig. 4–10, which are quite close to the current actuator locations used for ALTAV.

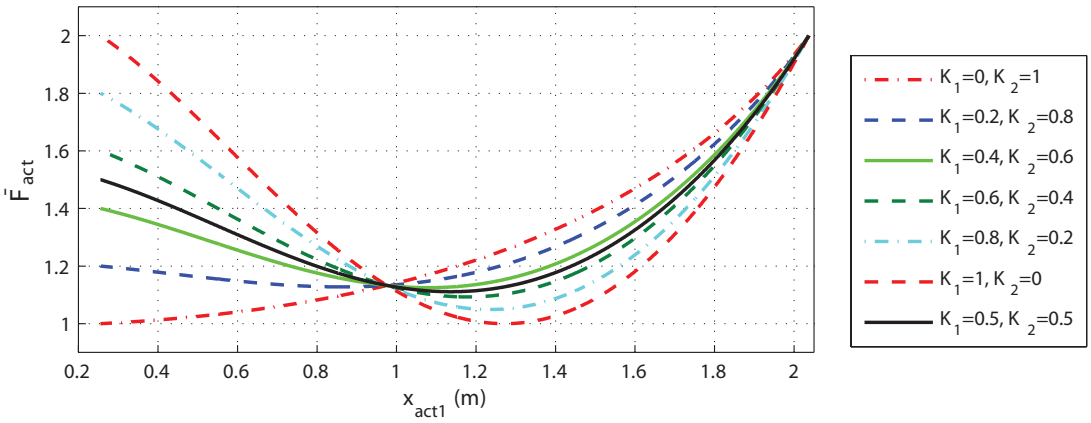

Figure 4–9: $\bar{F}_{act}$ ($k_1 = 0.0$, $k_2 = k_3 = 0.5$, $k_4 = k_5 = k_6 = k_7 = 0.25$)

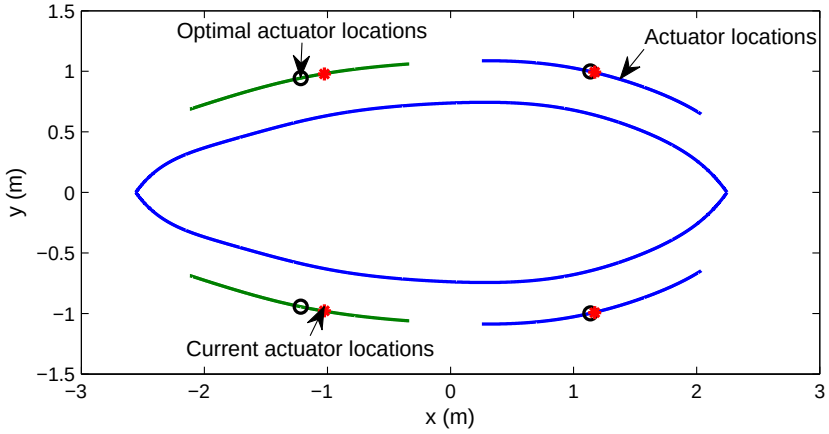

Figure 4–10: Optimal actuator locations of $\bar{F}_{act}$ with $k_1 = 0.0$, $k_2 = k_3 = 0.5$, $k_4 = k_5 = k_6 = k_7 = 0.25$, $K_1 = K_2 = 0.5$

CHAPTER 5
Conclusion

This thesis has focused on the design of highly maneuverable airships. Three areas were studied in this work, with emphasis on airship size minimization method, airship maneuverability quantification method that can be applied to ALTAV airship, and optimal actuator locations for ALTAV that can help ALTAV achieve highest maneuverability. In the following sections, a summary and concluding remarks are provided for each of the areas.

5.1 Airship Size Minimization

In chapter 2, a size minimization method for non-rigid airships was proposed. The size minimization flow chart was provided at the beginning of that chapter, which could be used for small airship design in the conceptual design phase. Based on this flow chart, four modules directly relating to airship design were illustrated. In the Pressure and Fabric Module, the envelope pressure, the required strength of the envelope and ballonets were obtained according to airship mission profile requirements. If the available material is not strong enough, new materials are required or the mission profile must be changed. The second module was the Geometric Module, in which the airship envelope size and surface area were calculated. The mass of the envelope could be estimated by using the material tested by the Pressure and Fabric Module. In the third module, the Aerostatic Module, the required ballonets volume was calculated from the relationship between the atmospheric condition and

flight mission requirements. After obtaining the ballonets volume, the mass of the ballonets and the available net lift during flight can be computed. In the fourth module, the Power and Propulsion Module, the required engine power is coupled based on the aerodynamic drag. Then, the number of engines and the mass of the required fuel are computed, as well as the mass of the propulsion system. After that, the mass of other subsystems can be estimated. The masses of all subsystems are added together and compared with the available net lift. The sizing program is iterated in this manner until the minimum size of the airship that could provide enough lift is found.

In addition to the size minimization method, new materials and novel propulsion systems were presented in chapter 2 and adopted in the sizing procedure. The algorithm validation was given at the end of the chapter, through application to non-rigid airships sizing with and without fins.

5.2 ALTAV Maneuverability Quantification and Maneuver Tests

In order to improve airship maneuverability and design a small highly maneuverable airship, Chapter 3 offered the airship maneuverability quantification method according to the proposed to date maneuver tests and simulations conducted for ships, aircraft and airships. The heading angle was defined as the primary variable for describing airship maneuvering capability. Three maneuver tests were adopted to explore airship maneuverability: the straight forward maneuver, the zig-zag maneuver and the turning maneuver. The maneuverability quantifications were offered based on each maneuver test.

This maneuverability quantification method was applied to ALTAV in Chapter 3. Besides, since improving small airship maneuverability was one of the goals of this work, a set of 8×8 actuator locations was employed in evaluating each maneuver test. Considering the influence of control method on ALTAV maneuverability, two control methods were adopted in ALTAV maneuver tasks: the PID control method and the open-loop optimal control method. Four maneuvering tasks were designed for ALTAV, including the $\psi_f = 360°$ turning maneuver under PID control, the zig-zag maneuver under PID control, the straight forward maneuver with optimal control, and the $\psi_f = 180°$ turning maneuver with optimal control.

Comparing the simulated responses obtained with PID control and optimal control, optimal control produced better maneuverability. The simulation results with optimal control were taken as reference for further analysis on the influence of actuator locations on ALTAV maneuverability.

5.3 ALTAV Optimal Actuator Locations

The aim of Chapter 4 was to find the optimal actuator locations for ALTAV. The terms in ALTAV dynamics model were analyzed in order to disclose the influence of actuator locations on ALTAV maneuverability. Then, the symbolic equations for entries in the inverse mass matrix of ALTAV were developed, and the effect of actuator location on these entries was analyzed. Based on a comparison with the inverse mass matrix of a famous airship Skyship-500, the method used to nullify some of the off diagonal entries was provided. In the simulations which ALTAV can finish the required maneuvers with certain actuator location combinations, the control forces and moments play a very important role. In order to explain the effect

of actuator locations on a straight forward and turning maneuvers, the control forces and moments were evaluated symbolically and the corresponding maximum available accelerations and angular accelerations were computed.

Based on the results of the above analysis, the cost function for optimizing actuator locations was proposed. The coefficients used to weight the maneuverability in different directions were studied, and the optimal actuator locations to achieve equal weighting for longitudinal and lateral maneuvering were selected at the end of that chapter.

5.4 Future Work

Several directions are suggested for further research based on study presented in this thesis:

- Although the new technologies for the Power and Propulsion Module were adopted in this thesis, the method used to calculate the available thrust and corresponding power depends on the specific experimental results of that certain type of of power and propulsion system. The theoretical method used to calculate the available thrust and the corresponding power for general novel power and propulsion system is undeveloped. New theoretical methods that could be applied to mass estimation of these novel technologies are required.
- The maneuverability quantification method proposed in this thesis is based on research on ships, aircraft and airships, and may have some limitations when applied to certain scenarios that are specific to airships, for instance, for evaluating the ability to resist kiting motion. Therefore, developing methods that are particular to quantifying special airship maneuvers could be useful.

- In [17], there are sixteen design maneuver conditions employed for airship design. In this thesis, only the most important maneuvers, the straight forward maneuver, the turning maneuver and the zig-zag maneuver are studied. Additional maneuver conditions can be taken into account to cover the full range of mission requirements.
- The values of the coefficients in the cost function for optimizing actuator locations were decided based on the assumed proportions of the straight forward maneuver and the turning maneuver in the whole maneuver mission. In addition, the GPOPS is not very efficient when it is used to solve a multi-phase maneuvering mission of ALTAV, which includes a series of straight forward and turning maneuvers. Therefore, a more efficient optimization algorithm should be adopted to validate the selected optimal actuator locations based on the proposed method in Chapter 4.

References

[1] D.M. Acosta and S.S. Joshi. Adaptive nonlinear dynamic inversion control of an autonomous airship for the exploration of titan. In *AIAA Guidance, Navigation, and Control Conference 2007;Hilton Head, SC7*, volume 2, pages 1690–1702, 20 August-23 August 2007.

[2] R.E. Adams. Parametric sizing of modern naval airships. In *AIAA 8th Lighter-than-air Systems Technology Conference, Jacksonville, FL*, 1989.

[3] H. Allen. *The story of the airship*. Akron, Ohio : Goodyear Tire and Rubbery, 1932.

[4] H.J. Allen and E.W. Perkins. *A study of effects of viscosity on flow over slender inclined bodies of revolution*. National Aeronautics and Space Administration Moffett Field CA Ames Research Center, 1951.

[5] A. Arbel. Controllability measures and actuator placement in oscillatory systems. *International Journal of Control*, 33(3):565–574, 1981.

[6] R.A. Barr, E.R. Miller, V. Ankudinov, and F.C. Lee. Technical Basis for Maneuvering Performance Standards. *US Coast Guard Report CG-8-81, NTIS ADA*, 11474, 1981.

[7] D.A. Benson, G.T. Huntington, T.P. Thorvaldsen, and A.V. Rao. Direct trajectory optimization and costate estimation via an orthogonal collocation method. *Journal of Guidance, Control and Dynamics*, 29(6), 2006.

[8] S. Bocvarov, F. LUTZE, and E. CLIFF. Time-optimal reorientation maneuvers for a combat aircraft. *Journal of Guidance, Control, and Dynamics*, 16(2):232–240, 1993.

[9] N. BOON. Mini airship patrol craft. Bachelor Thesis, National University of Singapore, 2003.

[10] C.P. Burgess. *Airship design*. The Ronald Press Company, 1927.

[11] S.A. Cambone and Office of The Secretary of Defense Washington DC. *Unmanned aircraft systems roadmap 2005-2030*. Defense Technical Information Center, 2005.

[12] W.J. Chen and W.W. Xiao. Structural performance evaluation procedure for large flexible airship of HALE stratospheric platform conception. *Journal of Shanghai Jiaotong University (Science)*, 12(2):293–300, 2007.

[13] C.L. Darby, W.W. Hager, and A.V. Rao. An hp-adaptive pseudospectral method for solving optimal control problems. *Optimal Control Applications and Methods*, 32(4):476–502, 2011.

[14] B. Dorminey and The Daily Climate. Is there a future for airships. `http://www.scientificamerican.com/article.cfm?id=is-there-a-future-for-airships`. May 3, 2011.

[15] GE Dorrington. Concept options for the aerial survey of titan. *Advances in Space Research*, 47(1):1–19, 2011.

[16] Y. Fan and Lutze. Time-optimal lateral maneuvers of an aircraft. *Journal of Guidance, Control, and Dynamics*, 18(5):1106–1112, 1995.

[17] Federal Aviation Administration. *Airship Design Criteria*, rept. p-8110-2 chg 2 edition, 1995.

[18] R.D. Finck, D.E. Hoak, Douglas Aircraft Company, and Air Force Flight Dynamics Laboratory (US). *USAF stability and control DATCOM*. Flight Control Division, Air Force Dynamics Laboratory, Wright-Patterson Air Force Base, 1978.

[19] D. Garg, W.W. Hager, and A.V. Rao. Pseudospectral methods for solving infinite-horizon optimal control problems. *Automatica*, 2011.

[20] D. Garg, M. Patterson, W.W. Hager, A.V. Rao, D.A. Benson, and G.T. Huntington. A unified framework for the numerical solution of optimal control problems using pseudospectral methods. *Automatica*, 46(11):1843–1851, 2010.

[21] D. Garg, M.A. Patterson, C. Francolin, C.L. Darby, G.T. Huntington, W.W. Hager, and A.V. Rao. Direct trajectory optimization and costate estimation of finite-horizon and infinite-horizon optimal control problems using a radau pseudospectral method. *Computational Optimization and Applications*, 49(2):335–358, 2011.

[22] Manuever Air Support Working Group. Airships for civil and military uses. http://www.angelfire.com/art/enchanter/airship.html.

[23] D. Halim and SO Reza Moheimani. An optimization approach to optimal placement of collocated piezoelectric actuators and sensors on a thin plate. *Mechatronics*, 13(1):27–47, 2003.

[24] H. Harper. *The evolution of the flying machine: balloon, airship, aeroplane*. Philadelphia : D. McKay, 1930.

[25] R.C. Hibbeler. *Mechanics of Materials*. Prentice Hall, Upper Saddle River, 2011.

[26] E.J. Hopkins and United States National Advisory Committee for Aeronautics. *A semi-empirical method for calculating the pitching moment of bodies of revolution at low Mach numbers*. National Advisory Committee for Aeronautics, 1951.

[27] J.E. Houmard. Maximum size of a non-rigid airship. In *AIAA/AHS/ASEE Aircraft Systems, Design and Technology Meeting, Dayton, OH, USA.*, 1986.

[28] L.H. Jorgensen. *Prediction of static aerodynamic characteristics for space-shuttle-like and other bodies at angles of attack from* 0° *to* 180°. National Aeronautics and Space Administration, 1973.

[29] G. A. Khoury and I. D. Gillett. *Airship technology*. Cambridge University Press, 1999.

[30] U.S. Naval Research Lab. Welcome the arrival of the airship mz3a. http://www.nrl.navy.mil/media/videos/welcome-the-airship-mz-3a-to-scientific-development-squadron-one-vxs-1.

[31] J. W. Lancaster. Feasibility study of modern airships. Technical report, NASA, 1975.

[32] J.W. Lancaster and D.B. Bailey. Naval airship program for sizing and performance (napsap). *Journal of Aircraft*, 18(8):677–682, 1981.

[33] A. Landsburg, J. Card, H. Eda, H. von Breitenfeld, and T. Knerim. Proposed Shipboard Maneuvering Data. In *1980 SNAME Spring Meeting and STAR Symposium, Coronado, California*, pages 241–262, 1980.

[34] A.C. Landsburg, J.C. Card, C.L. Crane Jr, P.R. Alman, W.R. Bertsche, J.W. Boylston, H. Eda, V.F. Keith, and I.R. McCallum. Design and verification for adequate ship maneuverability. *SNAME TRANS.*, 91:351–401, 1983.

[35] Y. Li. *Dynamics Modeling and Simulation of Flexible Airships*. PhD thesis, McGill University, 2008.

[36] Y. Li, A.C. Landsburg, R.A. Barr, and SM Calisal. Improving ship maneuverability standards as a means for increasing ship controllability and safety. In *OCEANS, 2005. Proceedings of MTS/IEEE*, pages 1972–1981. IEEE, 2005.

[37] C. Liang, FP Sun, and CA Rogers. Determination of design of optimal actuator location and configuration based on actuator power factor. *Journal of intelligent material systems and structures*, 6(4):456–464, 1995.

[38] T. Liu, W.W. Liou, and M. Schulte. Aeroship: A hybrid flight platform. *Journal of aircraft*, 46(2):667–674, 2009.

[39] X. Liu, D.W. Begg, and D.R. Matravers. Optimal topology/ actuator placement design of structures using sa. *Journal of Aerospace Engineering*, 10:119, 1997.

[40] S. Maekawa, M. Nakadate, and A. Takegaki. Structures of the Low-Altitude Stationary Flight Test Vehicle. *Journal of aircraft*, 44(2):662, 2007.

[41] S. Maekawa and T. Yoshino. Tear propagation of a high-performance airship envelope material. *Journal of Aircraft*, 45(5):1546–53, 2008.

[42] P.G. Maghami and S.M. Joshi. Sensor/actuator placement for flexible space structures. *IEEE Transactions on Aerospace and Electronic Systems*, 29(2):345–351, 1993.

[43] M. Mattingly, R.B. Roemer, and S. Devasia. Optimal actuator placement for large scale systems: a reduced-order modelling approach. *International journal of hyperthermia*, 14(4):331–345, 1998.

[44] B. McCormick. *Aerodynamics, aeronautics, and flight mechanics*. Wiley, 1995.

[45] E. Miller, V. Ankudinov, and T. Ternes. Evaluation of concepts for improved controllability of tank vessels. *Marine Technology*, 18(4):365–381, 1981.

[46] T. Miller and M. Mandel. Airship envelopes: Requirements, materials and test methods. In *3rd International Airship Convention and Exhibition*, pages 1–5, 2000.

[47] B.L. Nagabhushan and G.D. Faiss. Thrust vector control of a V/STOL airship. *Journal of Aircraft*, 21(6), 1984.

[48] B.L. Nagabhushan and N.P. Tomlinson. Thrust-vectored takeoff, landing, and ground handling of an airship. *Journal of Aircraft*, 23:250–256, 1986.

[49] N. NOAA and U.S.A. Force. US Standard Atmosphere, 1976. *US Government Printing Office, Washington, DC*, 1976.

[50] K. Nomoto. Response Analysis of Maneuverability and its Application to Ship Design. *60th Anniversary Series, The Society of Naval Architects of Japan*, 11, 1966.

[51] J. Olson and M. Scott. Helicopter design optimization for maneuverability and agility. In *AHS, Annual Forum, 45 th, Boston, MA*, 1989.

[52] R.S. Pant. Methodology for determination of baseline specifications of a nonrigid airship. *Journal of Aircraft*, 45(6), 2008.

[53] V. H. Pavlecka. Thruster control for airships. *AIAA Lighter-Than-Air Systems Technology Conference, Palo Alto, Calif., UNITED STATES*, pages 82–87, July 11-13, 1979.

[54] P. Peddiraju. Development and validation of a dynamics model for an unmanned finless airship. Master's thesis, McGill University, 2010.

[55] A.V. Rao, D. Benson, C.L. Darby, B. Mahon, C. Francolin, M. Patterson, I. Sanders, and G.T. Huntington. User's manual for gpops version 4. x: A matlab r o software for solving multiple-phase optimal control problems using hp–adaptive pseudospectral methods. 2011.

[56] A.V. Rao, D.A. Benson, C. Darby, M.A. Patterson, C. Francolin, I. Sanders, and G.T. Huntington. Algorithm 902: Gpops, a matlab software for solving multiple-phase optimal control problems using the gauss pseudospectral method. *ACM Transactions on Mathematical Software (TOMS)*, 37(2):22, 2010.

[57] M.R. Robinson and W.B. Herbst. The X-31 A and advanced highly maneuverable aircraft. In *ICAS, Congress, 17 th, Stockholm, Sweden*, 1990.

[58] J.B. Russell. *Performance and stability of aircraft*. Butterworth-Heinemann, 1996.

[59] M. Sato. Flight test of flight controller for arbitrary maneuverability and wind gust rejection. In *2006 IEEE Computer Aided Control System Design, 2006 IEEE International Conference on Control Applications, 2006 IEEE International Symposium on Intelligent Control*, pages 2534–2540, 2006.

[60] R. Skjetne, T.I. Fossen, and P.V. Kokotović. Adaptive maneuvering, with experiments, for a model ship in a marine control laboratory. *Automatica*, 41(2):289–298, 2005.

[61] C. Sprigg. *The airship: its design, history, operation and future*. London : S. Low, Marston, 1931.

[62] D. Stinton. *The design of the aeroplane*. Blackwell Science, 1995.

[63] W. Tennakoon and S.R. Munasinghe. Design and simulation of a UAV controller system with high maneuverability. In *4th International Conference on Information and Automation for Sustainability, 2008. ICIAFS 2008*, pages 431–436, 2008.

[64] A.D. Topping. The critical slit length of pressurized coated fabric cylinders. *Journal of Industrial Textiles*, 3(2):96–110, 1973.

[65] Q. Wang, J. Chen, G. Fu, D. Duan, and H. Zhao. A methodology for optimisation design and analysis of stratosphere airship. *Aeronautical Journal.*, 113(1146):533–540, 2009.

[66] Y.W. Wu, R.B. Rice, and J.N. Juang. Sensor and actuator placement for large flexible space structures. In *Proceedings of the Joint Automatic Control Conference*, pages 230–238. American Institute of Chemical Engineers, 1979.